MECHANISTIC STUDY OF SELF-ASSEMBLED TUNGSTEN NANOGRATINGS ON SOLIDS INDUCED BY FEMTOSECOND LASER BEAM

by

Mingzhen Tang

A dissertation submitted to the faculty of
The University of North Carolina at Charlotte
in partial fulfillment of the requirements
for the degree of Doctor of Philosophy in
Optical Science and Engineering

Charlotte

2010

Approved by:

_____
Dr. Tsing-Hua Her

_____
Dr. James Amburgey

_____
Dr. Wei Cai

_____
Dr. Steve Bobbio

_____
Dr. Greg Gbur

_____
Dr. Raphel Tsu

ABSTRACT

MINGZHEN TANG. Mechanistic study of self-assembled tungsten nanogratings on solids induced by femtosecond laser beam. (Under direction of DR. TSING-HUA HER)

This dissertation describes a mechanistic study on the spontaneous formation of tungsten nanograting induced by a 400 nm femtosecond laser beam on solids observed in laser induced chemical vapor deposition configuration. The formed tungsten nanograting has a periodicity less than half the laser wavelength, and the orientation of the nanograting is parallel to the laser polarization direction, given that the laser is linearly polarized. By translating the substrate with respecting to the fixed laser beam, long-range ordered transverse or longitudinal nanograting is produced depending on the angle between the translating and laser polarization directions. Systematic experimental studies on the effect of laser power, scanning speed of substrate, laser polarization, wavelength and substrate were carried out in detail. The formation of tungsten nanograting is nearly a universal phenomenon observed on a wide range of substrates. Appearance of tungsten nanograting requires a threshold laser power which varies for different substrates. The grating period can be tuned simply by managing writing parameters. Scaling to large area grating pattern and feasibility of growing nanograting on curved surfaces were also demonstrated. Evidence shows that laser heating and local field enhancement are involved in the formation of tungsten nanograting. A crude conjectured theoretical model was proposed to explain the mechanism of tungsten nanograting formation. Due to the novel nature of self-assembled tungsten nanograting, this study is expected to advance the knowledge on laser-material interaction field.

ACKNOWLEDGMENTS

The past six years of graduate school study has been enjoyable and fulfilling. My deep thanks go to many people who have made this long journey so pleasant.

First and foremost, I would like to express my deepest gratitude to my advisor, Dr. Tsing-Hua Her. I joined Dr. Her's group with zero experience on optics and research laboratory works. Dr. Her spent lot of time teaching me hand by hand on experiments, starting from cleaning a mirror and tying down a screw properly. His continuing support and guidance helped me through these years when we encountered difficulties in experiments and interpretation of experimental results. I appreciated many chances to be involved in all aspects of research Dr. Her gave me, in addition to the core elements of carrying out and analyzing experiments: I have gained experience in coming up with ideas for experiments, writing articles, and presenting results on international conferences. Finally, I would like to thank Dr. Her for treat us like friends and always been supportive and helpful on personal life.

This project would not have been possible without some very bright co-workers. I had the chance to work with Dr. Haitao Zhang. Who took lead and spent lots of time building the vacuum system of the experiments, preparing substrates, acquiring high quality SEM and AFM images. I benefited enormously from Haitao and learned a lot from him on material science. It was also appreciated to have Jerry McCoy taking some time to help on this project, who took big effort to work on the motion control system. I sincerely thank Dr. Xianyu Ao and Yue Zhou for their input on the temperature calculation presented in Appendix B.

I would like to thank the other members of my dissertation committee, Dr. James Amburgey, Dr. Stephen Bobbio, Dr. Wei Cai, Dr. Greg Gbur, and Dr. Raphel Tsu for their interest in my work and valuable inputs.

My great thanks also go to many people outside the lab. I have made so many friends with other graduate students, staff of physics department and optoelectronics center, who have shared my happiness, embraced my complaints, and made me feel part of a close family.

Finally, I want to thank all of my family members, for their unconditional generosity, love and encouragement.

I gratefully acknowledge the financial support from the department of physics and optical science, and DARPA grant # W911NF-05-2-0053.

TABLE OF CONTENTS

LIST OF FIGURES ix

LIST OF TABLES xiii

LIST OF ABBREVIATIONS xiv

CHAPTER 1 : INTRODUCTION 1

CHAPTER 2 : BACKGROUND 6

2.1 Laser induced Chemical Vapor Deposition (LCVD) 6

2.2 Deposition of tungsten out of tungsten hexacarbonyl 8

CHAPTER 3 : EXPERIMENTS 10

3.1 Experimental setup 10

3.1.1 Optical system 11

3.1.2 Vacuum system 15

3.1.3 Motion Control 16

3.2 Substrates preparation and experiment procedure 17

3.3 Characterization methods and preliminary results 19

3.3.1 Characterization techniques 19

3.3.2 Physical attributes of tungsten nanograting 19

3.3.2.1 Tungsten nanograting grown in stationary mode 19

3.3.2.2 Tungsten nanograting grown in scanning mode 21

3.3.3 Verification of tungsten growth 22

CHAPTER 4 : CHARACTERISTICS OF TUNGSTEN NANO-GRATINGS 24

4.1 Laser power and exposure effects 24

4.1.1 Evolution of TNG in stationary mode 24

4.1.2 Evolution of TNG in scanning mode 26
4.2 Effect of laser polarization on tungsten nanograting growth 33
4.2.1 Growth morphology with linear polarization 33
4.2.2 Polarization state evolution of TNG 36
4.2.3 Cross polarization study 41
4.3 Dependence on laser wavelength 43
CHAPTER 5 : SUBSTRATE EFFECT ON NANOGRATINGS 47
5.1 Substrates and their material properties 47
5.2 Universality of tungsten nanograting 49
5.3 The dependence of TNG period on substrate 51
5.4 Effect of substrate on threshold laser power for TNG growth 56
CHAPTER 6 : MECHANISM DISCUSSION 59
6.1 Periodic structure induced by a single laser beam 59
6.1.1 Laser induced periodic surface structure 59
6.1.2 Femtosecond laser induced periodic surface structure 60
6.1.3 Self organization from instability induced by single beam 62
6.1.4 Femtosecond laser induced periodic nano-cracks inside substrate 63
6.1.5 Periodic structure in deposited metal film 64
6.2 Mechanistic study on the formation of tungsten nanograting 65
6.2.1 Formation of periodic surface structures in ablation case 65
6.2.2 Growth of tungsten thin film and discussion on laser power threshold 66
6.2.3. The role of laser heating in the formation of tungsten nanogratings 67
6.2.4 Local field enhancement and asymmetric growth of tungsten nano-particle 70
6.2.5. Conjectured mechanism on self-assembly of tungsten nanogratings 72

CHAPTER 7 : FEASIBILITY AND POTENTIAL APPLICATIONS OF TNG 77

7.1 Feasibility and scalability of tungsten nanogratings 77

7.2 Comparison with other nano-patterning methods 81

7.3 Potential applications of TNG 82

REFERENCES 84

APPENDIX A: DETAILED RESULTS ON SUBSTRATE STUDY 89

APPENDIX B: DERIVATION ON THE ABSORPTANCE OF TUNGSTEN FILM 102

LIST OF FIGURES

Figure 2.1: Schematic of photolytic LCVD process 7

Figure 2.2: Schematic of the reaction process of LCVD 9

Figure 3.1: Schematic of femtosecond LCVD experiments. 10

Figure 3.2: Picture of the fs LCVD experimental setup. 11

Figure 3.3: FROG traces 12

Figure 3.4: Schematic of a telescope used to expanding the beam size 13

Figure 3.5: Cross section of the expanded and collimated laser beam. 13

Figure 3.6: Power correction for laser beams 15

Figure 3.7: Schematic of the vacuum system. 16

Figure 3.8: SEM image and AFM images of a TNG deposited on sapphire 20

Figure 3.9: SEM images of transverse and longitudinal TNGs on sapphire 22

Figure 3.10: EDX spectra 23

Figure 4.1: SEM image of a dot array grown on sapphire 25

Figure 4.2: SEM images of time evolution of grating formation 26

Figure 4.3: SEM images of power effect on grating formation 26

Figure 4.4: SEM images of longitudinal TNGs on sapphire 27

Figure 4.5: SEM images of transverse TNGs 28

Figure 4.6: SEM images of TNGs on sapphire 29

Figure 4.7: Schematic of grating period determination procedure 30

Figure 4.8: Dependence of L and Λ of transverse TNGs on V 32

Figure 4.9: The relationship between Λ of longitudinal TNG and laser power 33

Figure 4.10: Schematic of rotating linear polarization direction. 34

Figure 4.11: SEM image of a TNG array 35

Figure 4.12: SEM images of tungsten gratings with different orientation 36

Figure 4.13: SEM images of polarization dependence study 37

Figure 4.14: Schematic of changing polarization state. 38

Figure 4.15: Evolution of TNG growth as polarization state changes 39

Figure 4.16: SEM images of TNG written with elliptically polarized laser beam 40

Figure 4.17: Relation between Λ in normal direction and the rotating angle 41

Figure 4.18: SEM images of TNG written with cross-polarization 42

Figure 4.19: SEM images of tungsten deposition with 800-nm laser beam 44

Figure 4.20: Grating period versus scanning speed for different laser wavelengths 45

Figure 5.1: EDX spectra of the soda-lime glass substrate. 48

Figure 5.2: SEM images of transverse tungsten nanograting on insulators 49

Figure 5.3: SEM images of transverse tungsten nanogratings on semiconductors 50

Figure 5.4: SEM images of surface roughness and TNG grown on metals 51

Figure 5.5: Plot of grating period versus scanning speed for insulators 52

Figure 5.6: Plot of grating period versus scanning speed for semiconductors 52

Figure 5.7: Plot of P_1 as a function of refractive index of substrate 56

Figure 5.8: AFM images of TNG and tungsten stripe 57

Figure 6.1: Ripples in fused silica 60

Figure 6.2: SEM images of self-organized periodic nanoplanes 64

Figure 6.3: SEM images of ablated surface morphologies 66

Figure 6.4: Threshold power of TNG as a function of S 69

Figure 6.5: FDTD simulation results 71

Figure 6.6: SEM images show tungsten nanostructure evolution 72

Figure 6.7: Conjectured model of TNG formation 73

Figure 6.8: Conjectured model on grating period prediction. 74

Figure 7.1: SEM images of circular and “UNCC” grating pattern 78

Figure 7.2: SEM image of multiple scanned TNGs 79

Figure 7.3: SEM images of Tungsten nanostructure on surface of ZnO Micro-wire. 80

Figure 7.4: SEM image of TNG grown on the surface of glass optical fiber. 81

Figure Appx. 1: SEM images of transverse TNGs on sapphire 89

Figure Appx. 2: Plot of TNG period as a function of V on sapphire 90

Figure Appx. 3: SEM images of transverse TNGs on soda-lime glass 90

Figure Appx. 4: Plot of TNG period as a function of V on glass 91

Figure Appx. 5: SEM images of transverse TNGs on fused silica 91

Figure Appx. 6: Plot of TNG period as a function of V on fused silica 92

Figure Appx. 7: SEM images of transverse TNGs on quartz 92

Figure Appx. 8: Plot of TNG period as a function of V on quartz 93

Figure Appx. 9: SEM images of transverse TNGs on calcium fluoride 93

Figure Appx. 10: Plot of TNG period as a function of V on calcium fluoride 94

Figure Appx. 11: SEM images of transverse TNGs on Magnesium fluoride 94

Figure Appx. 12: Plot of TNG period as a function of V on magnesium fluoride 95

Figure Appx. 13: SEM images of transverse TNGs on Magnesium oxide <100> 95

Figure Appx. 14: Plot of TNG period as a function of V on magnesium oxide <100> 96

Figure Appx. 15: SEM images of transverse TNGs on Magnesium oxide <110> 96

Figure Appx. 16: Plot of TNG period as a function of V on magnesium oxide <110> 97

Figure Appx. 17: SEM images of transverse TNGs on aluminum nitride 97

Figure Appx. 18: Plot of TNG period as a function of V on aluminum nitride 98

Figure Appx. 19: SEM images of transverse TNGs on Zinc Oxide 98

Figure Appx. 20: Plot of TNG period as a function of V on zinc oxide 99

Figure Appx. 21: SEM images of transverse TNGs on Gallium nitride 99

Figure Appx. 22: Plot of TNG period as a function of V on gallium nitride 100

Figure Appx. 23: SEM images of transverse TNGs on Silicon nitride 100

Figure Appx. 24: Plot of TNG period as a function of V on silicon nitride 101

Figure Appx. 25: Schematic of two layer system 105

Figure Appx. 26: Absorptance in tungsten film as a function of refractive index 106

LIST OF TABLES

Table 1: Material properties of selected substrates involved in the substrate study 48

Table 2: Theoretical fitting parameters for the period-speed data 54

LIST OF ABBREVIATIONS

fs	femtosecond
LCVD	laser-induced chemical vapor deposition
SCCM	standard cubic centimeter per minute
SEM	scanning electron microscopy
AFM	atomic force microscopy
EDX	energy-dispersive X-ray spectroscopy
FWHM	full wave at half maximum
LIPSS	laser induced periodic surface structure
FLIPSS	femtosecond laser induced periodic surface structure
SEW	surface electromagnetic wave
SPW	surface plasma wave

CHAPTER 1：INTRODUCTION

The first high-power source of pulses with 10-100nanoscond (10^{-9}sec) duration was demonstrated in 1964[1]. In the early eighties, several groups passed the 100 femtoseconds (10^{-15}sec) mark and the development of fs technology started quickly. By 1987, pulses as short as 6 fs have been achieved[2]. Today, commercial laser systems routinely produce sub-100 fs pulses, and these pulses are finding application in a variety of fields.

The transition to fs pulses is accompanied with a huge gain to higher intensities. Fs pulse propagation is a field rich in nonlinear phenomena because of the extremely high intensity. The short duration of femtosecond pulses has many light-matter interactions observable which were not accessible before the invention of short pulse lasers.

Fs technology opens up new possibilities in interacting with matters based on some unique properties of fs pulses:

- The energy is concentrated in a temporal interval as short as several 10^{-15}s which corresponds to only a few optical cycles in the visible range.
- The peak power and intensity can be extremely high even at moderate average pulse energies. For instance a 50-fs pulse with energy of 1-mJ exhibits a peak power of 200-igawatt (10^{9}W). Focusing this pulse to a 100-μm^2 spot yields a peak intensity of 20-Petawatt/cm^2 (10^{15}W/cm^2!), which means an electric field of about 3 GV/cm.

- The energy transfer is very fast. Photons of fs pulses interact with electrons strongly while remaining transparent to phonons, providing a non-thermal excitation process. This reduces the requirement of the energy input and minimizes the heat diffusion.
- Capability of initiating multi-photon process. Photon density is very high with ultra-high peak intensity even at low average power, make it possible for an atom or molecule to absorb two or more low energy photons simultaneously which otherwise are transparent to them in single photon absorption process.
- Strong localized 3D excitation. The excitation initiated by fs laser can be strongly localized in the focus volume where intensity is very high and reduce the infection to the surrounding area. By using a wavelength which is transparent to the bulk material, 3D structure can be directly fabricated inside bulk material.

All these unique properties enable fs laser to be widely used in various areas such as: material characterization, material processing, information processing, biomedical, metrology, and quantum control, etc. The application of fs in material processing has been mainly focused on two big categories, one is material removal: cutting and drilling[3], mask repair[4], laser surgery[5], etc. And the other one is material modification, including: embedded 3-D optical waveguide[6], two-photon polymerization[7], volume holography[8], etc. The above applications of femtosecond laser are all non-additive. Material deposition induced by fs laser, on the other hand, has not progressed until recently[9]. In which the authors reported that by focusing 400nm fs laser into a laser-induced chemical vapor deposition system, Metallic structures with

feature size of 100nm were written on transparent substrate. This high resolution resulted from multi-photon process and very tight focus (N.A=0.9). And there is no much room for further improvement. This technique is a serial writing process, which means it only produce one line at a time, to generate a large area of parallel lines, it requires repeating writing processes. Thus makes this technique time-consuming.

Recently, we reported a novel phenomenon on the self-assembly of tungsten nanostructures during the experiment similar to reference [9], in which a single 400-nm femtosecond Ti:Sapphire laser beam was gently focused onto the substrates to photo-dissociate tungsten carbonyl and induced the self-assembly of tungsten nanograting at room temperature without any masks or beam shaping [10-11]. The light can control the morphology of tungsten nanostructures, including its orientation, orderliness, aspect ratio, and periodicity. Compare to other laser chemical vapor deposition processes, this newly reported technique turns the nominal serial writing process into a parallel approach without adding any complex setup.

This dissertation presents in detail the mechanistic study of the self-assembled tungsten nanostructures. Systematical experiment studies, including on the effects of laser parameters, substrate motion, and substrate on the formation and properties of tungsten nanograting were conducted to reveal the physical mechanism of this phenomenon. The key significances expected from this work are: 1) this study discovers a novel phenomenon in laser-material interaction and the understanding of this process will advance our knowledge on this research area; 2) Detailed investigation on factors that correlated to tungsten nanograting allows us to produce tungsten nanograting that fulfill the designated requirements, thus make this discovery applicable in nanofabrication.

Organization of dissertation

Basic background information relevant to laser chemical vapor deposition (LCVD) is introduced briefly in Chapter 2. It includes the principle of LCVD, its advantage and applications. Two types of LCVD, photolytic and pyrolytic LCVD are discussed. Schematic introduction on femtosecond laser initiating the deposition of tungsten from precursor gas tungsten hexacarbonyl will also be covered in this chapter.

Chapter 3 presents the experiments. It covers the experimental setup, composed by optical system and vacuum system; the detailed experiment procedure; the investigation and analysis method of experiment data; and preliminary results.

Chapter 4 presents detailed results on the characteristic study of the deposited tungsten nanogratings. The study includes the evolution of tungsten nanogratings on laser power and exposure time, detailed experiments are designed to study the physical attributes and grating period change corresponding to laser power and exposure time/ scanning speed; the effect of the laser polarization effect on tungsten nanograting formation is discussed in section 4.2; and the relationship between grating period and writing laser wavelength is studied in section 4.3.

The results on substrate study are presented in Chapter 5 separately due to the large volume of information. Two main properties of tungsten nanograting dependence to substrate are studied in detail in this chapter: one is the grating period; another is the threshold laser power at which tungsten nanograting starts to grow. For each substrate, line array with different laser power and scanning speed are written to study the evolution of grating period, and then the mean grating period is obtained mathematically from the experiment data to study the substrate effect on tungsten nanograting period. The

threshold power is carefully obtained from the experiments to compare the requirement of tungsten grows on different substrate.

Chapter 6 discusses the mechanism behind the formation of tungsten nanogratings. In which Laser induced periodic surface structures and nanocracks inside bulk material are reviewed first. The corresponding theoretical explanations are also introduced. By studying the commons and differences between these laser induced periodic structures and self-assembled tungsten nanogratings, an alternative and preliminary theoretical model is proposed to explain the formation of tungsten nanogratings and their properties.

After presenting the feasibility and scalability of self-assembled tungsten nanogratings, the advantages and potential applications of this technique are summarized in Chapter 7.

Detailed substrate study results and derivation process on threshold temperature for tungsten nanograting were presented in Appendix A and B, respectively.

CHAPTER 2 : BACKGROUND

This chapter attempts to provide the reader with the information necessary to understand later chapters. The first section introduces general backgrounds on laser induced chemical vapor deposition. The second part presents some basics on femtosecond laser material processing. A brief description of the reaction process involved in deposition of tungsten induced by laser will be given at the end.

2.1 Laser induced Chemical Vapor Deposition (LCVD)

Laser-induced chemical vapor deposition (LCVD) is a process that utilizing laser to initiate the deposition of a solid material from a precursor material that contains the atom of target material. It allows single-step growth or direct writing of structures with small feature size confined in the focus of laser beam and has large selection on target materials.

The decomposition of precursor molecules in laser-induced chemical vapor deposition (LCVD) can be activated thermally (pyrolytic LCVD) or non-thermally (photolytic LCVD) or by a combination of both[12]. The process can be identified from the morphology of the deposit and/or from measurements of the deposition rate as a function of laser power, wavelength, and substrate material.

Pyrolytic LCVD is a thermally driven process in which the laser light heats up the substrate locally by focusing to a temperature required for decomposing the precursor molecule and not absorbed by the precursor molecule directly. The reactant gases fall into the heated region absorb the heat and get dissociated, and the target species condense

onto the substrate surface and form thin film. The benefits of pyrolytic LCVD include high processing speed and low impurity.

Photolytic LCVD, in which laser light is absorbed by the reactant gases, and breaks the chemical bonds of the molecule directly, i.e., non-thermally. The decomposition of precursor molecules takes place in the gas phase within the volume of the laser beam. The decomposed atoms diffuse and condense, in part, on the substrate surface. Figure 2.1 schematically shows the reaction of photolytic LCVD process. Structures grown in photolytic LCVD can achieve diffraction-limited feature size, but the writing speed is much slower than in pyrolytic LCVD.

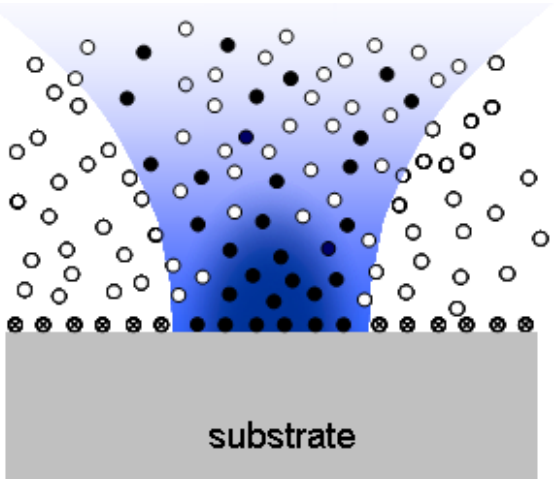

Figure 2.1 Schematic of photolytic LCVD process. Empty, solid, and cross circles represent precursors that are unexcited, excited, and adsorbed on surface, respectively.

In conventional Chemical vapor deposition process, the furnace heats the entire surface of the substrate uniformly to the temperature required for the reactions to proceed, the deposition is extended uniformly to the whole substrate. LCVD can be performed at considerably lower temperatures. In pyrolytic LCVD process, the heating zone is confined by the laser focus spot and leaving the substrate otherwise unaffected. In

photolytic LCVD, there is no or negligible surface heating take place. Thus, LCVD allows deposition of temperature-sensitive materials which would melt or decompose at the temperatures required for conventional CVD systems. The main applications of LCVD are: contacts, circuit repair, interconnect, mask repair and most attractive one, 3D objects.

2.2 Deposition of tungsten out of tungsten hexacarbonyl

Metal carbonyls and alkyls are always used for metal deposition in the form of microstructures and thin films. In the experiments involved in this dissertation, tungsten is deposited out of its gas phase precursor, tungsten hexacarbonyl. For cw- and pulsed-laser irradiation at low power densities, decomposition seems to be based on sequential elimination of CO ligands by single-photon processes [13]:

$$\begin{aligned}
&W(CO)_m + h\upsilon \rightarrow W(CO)^*_{m-1} + CO,\\
&W(CO)^*_{m-1} + h\upsilon \rightarrow W(CO)^*_{m-2} + CO,\\
&W(CO)^*_{m-2} + h\upsilon \rightarrow W(CO)^*_{m-3} + CO,\\
&\vdots \qquad\qquad \vdots \qquad\quad \vdots \qquad\quad \vdots\\
&W(CO)^* + h\upsilon \rightarrow W^* \qquad\quad + CO,
\end{aligned}$$

Focused high-power pulsed-laser excitation may facilitate multi-photon photochemistry rather than sequential single-photon process, i.e. the molecule may absorb multi-photon simultaneously and several bonds break at the same time.

Figure 2.2 shows the simplified schematic of the reaction process of tungsten deposition from the reactant tungsten hexacarbonyl gases. It involves three main steps: first, the reactant molecule absorb photons in a sequential or multi-photon simultaneously; secondly, the reactant molecule dissociate into tungsten atom and six CO ligands; and finally, the tungsten atoms diffuse and condense on the substrate and form thin film.

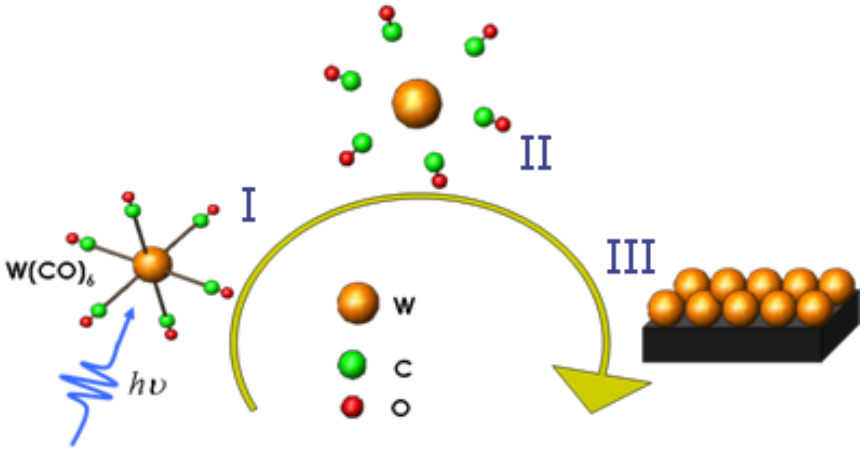

Figure 2.2 Schematic of the reaction process of Laser induced Chemical Vapor Deposition of tungsten: I) Energy absorption. II) Molecule dissociation. III) Tungsten deposition.

Tungsten hexacarbonyl has absorption peak at wavelength of 193nm, and a very weak absorption peak at 308nm[14]. The absorption cross section of $W(CO)_6$ at 400nm is orders of magnitude smaller than that at 308nm. Also with a total dissociation energy of $W(CO)_6$ to ground state W to be 11eV[15], a multi-photon absorption is expected to be involved in the photo-dissociation of $W(CO)_6$ with 400 nm (3.1 eV) light, which is the working wavelength involved in this dissertation study.

CHAPTER 3 : EXPERIMENTS

This chapter presents in detail the experimental setup of femtosecond laser induced chemical vapor deposition, including the optical system, vacuum system, and motion control system; detailed daily experiment process; the investigation and characterization methods and the preliminary results.

3.1 Experimental setup

The experimental setup includes three major systems: optical system, vacuum system, and motion control system. As shown schematically in Figure 3.1. Figure 3.2 is the picture of the LCVD experimental setup.

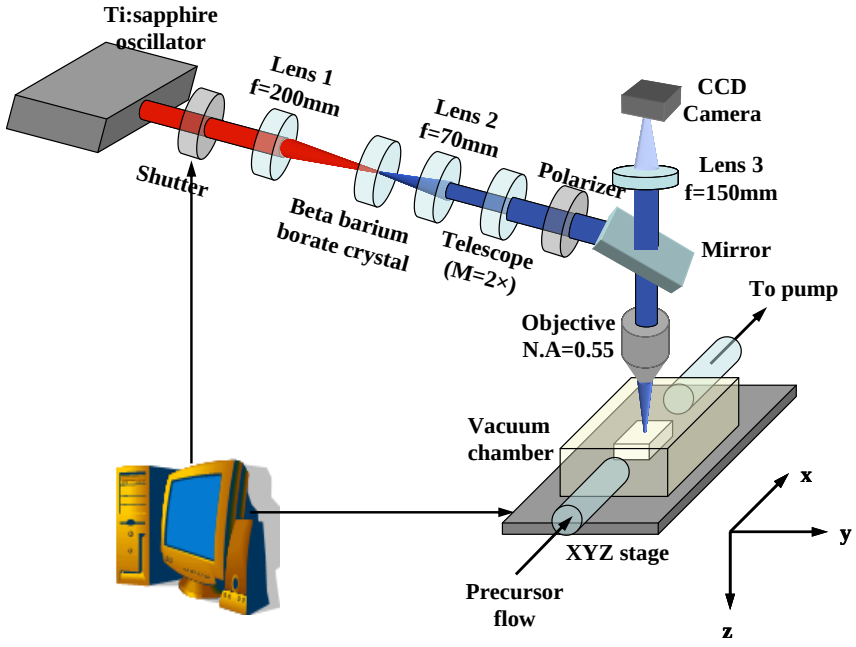

Figure 3.1 Schematic of femtosecond LCVD experiments.

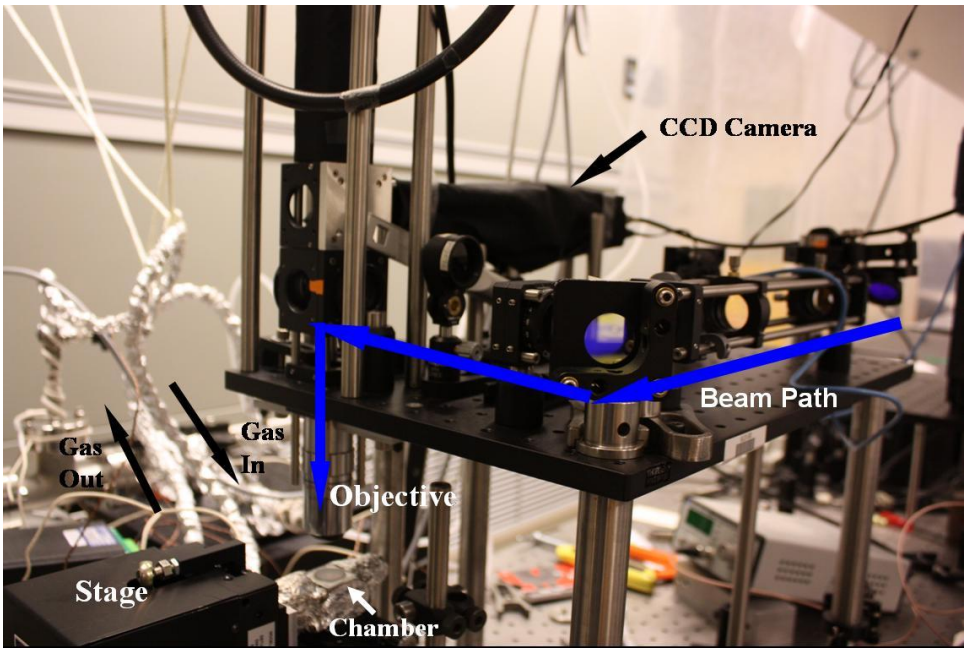

Figure 3.2 Picture of the fs LCVD experimental setup.

3.1.1 Optical system

The output of a mode-locked 80-MHz Ti:sapphire oscillator (Kapteyn-Murnane Labs and Tsunami from Newport) with 800-nm center wavelength and 1W average power was the fundamental laser source. The laser is monitored with spectrometer, oscilloscope during experiments. The output pulse is measured by a Frequency-resolved optical gating (FROG). Figure 3.3 shows the spatial (a) and temporal (b) profile of the outputting pulses. The full wave half maximum (FWHM) spectrum width measured in wavelength is 11-nm ($\Delta\upsilon = \frac{c}{\lambda^2}\Delta\lambda$), corresponding to 5.1×10^{12} Hz in frequency spectrum width.

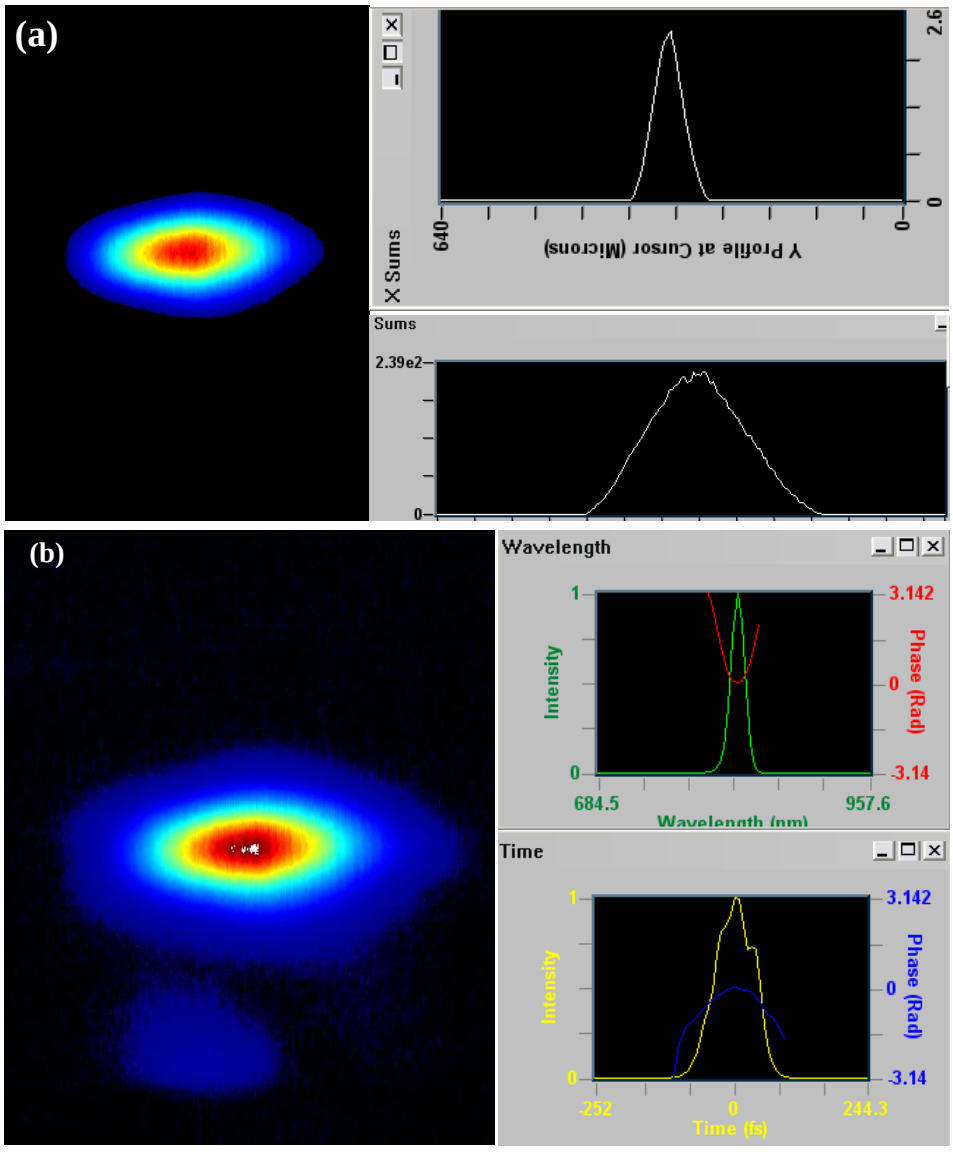

Figure 3.3 FROG trace of (a) spatial and (b) temporal of the 800-nm femtosecond pulses.

To generate the 400-nm laser pulses, the fundamental laser beam was focused through a beta-BaB_2O_4 (BBO) crystal by a lens with focus length of 200-mm. The 400-nm laser pulses were produced through the procedure called second harmonic generation (SHG) or frequency doubling. The 800-nm component in the output beam was filtered by the following highly selective reflecting mirrors designated for 400-nm in the

downstream after the SHG process in the beam path. A home-build telescope shown schematically in Figure 3.3 with magnification of 2X is applied to expand and collimate the beam. Negative lens was chosen here to take advantage of limited space. The cross-section of the collimated beam is measured and the result is shown in Figure 3.4. The beam size is determined to be 2.8-mm.

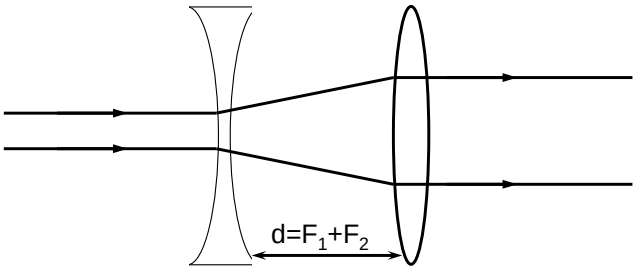

Figure 3.4 Schematic of a telescope used to expanding the beam size. In the real experiment, F1=-50mm, F2=100mm. The magnification M=F2/F1=-2.

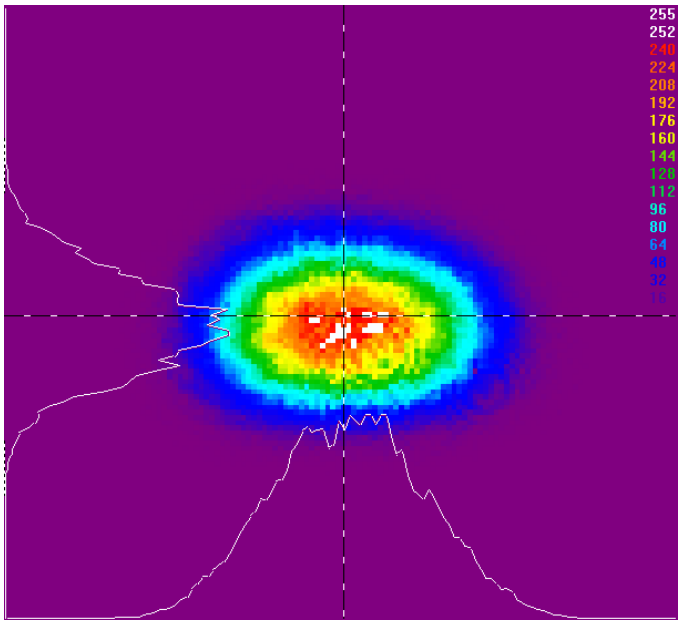

Figure 3.5 Cross section of the expanded and collimated laser beam.

The collimated and expanded beam is then focused onto the substrates normally using a long-working-distance (13-mm) microscope objective (Mitutoyo) with 0.55 Numerical Aperture. However, given the beam diameter of 2.8-mm and while the diameter of the objective aperture was 5-mm, which indicated the effective N.A is about 0.3. The focal spot size rendered by the objective is then calculated by the following formula and the value is about 0.8-μm in diameter:

$$2w_0 = (\frac{2\lambda}{\pi})(\frac{1}{2N.A}). \tag{3.1}$$

Considering the aberration caused by the 1mm thick glass (BK7) window of the vacuum chamber, the real focus spot size should be larger than the above calculated value.

Laser power was adjusted using a neutral-density filter and measured before the microscope objective. To determine the final power delivered onto the substrate. The actual power after the microscope objective and the glass chamber window was measured and compared to the measuring value before the objective to calculate the power loss ratio. The results of different writing lasers are shown in Figure. 3.5. The power values quoted in this dissertation are corrected values at the substrate.

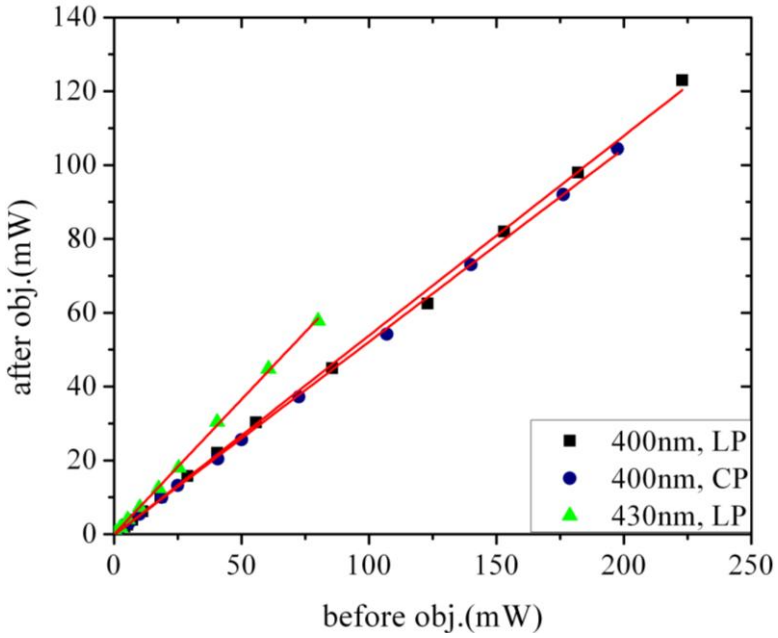

Figure 3.6 Power correction for laser beam of 400-nm linearly polarized, 400-nm circularly polarized, and 430nm linearly polarized.

3.1.2 Vacuum system

All the chemical reactions are carried out inside a home-built vacuum system. The reaction chamber is an aluminum cubic chamber equipped with a 1-mm thick glass window (BK7) through which the laser beam is introduced onto the substrate. An aluminum cylinder is sitting inside the chamber acting as a sample holder. The upstream end of the chamber is connected to the source reservoir where the precursor is stored, with its downstream end pumped by vacuum pump system including a rough and a turbo pump. The upstream end of the source cell is connected to a high purity nitrogen gas tank. During the experiments, nitrogen gas passes through the reservoir and carries the precursor gas to the reaction chamber. The flow of nitrogen gas is regulated by an un-calibrated flow meter with reading about 20-SCCM (standard cubic centimeter per minute). Both the valves that connect the chamber to source reservoir and vacuum pump

were fully opened during the experiments. The schematic of the vacuum system is shown in Figure 3.6.

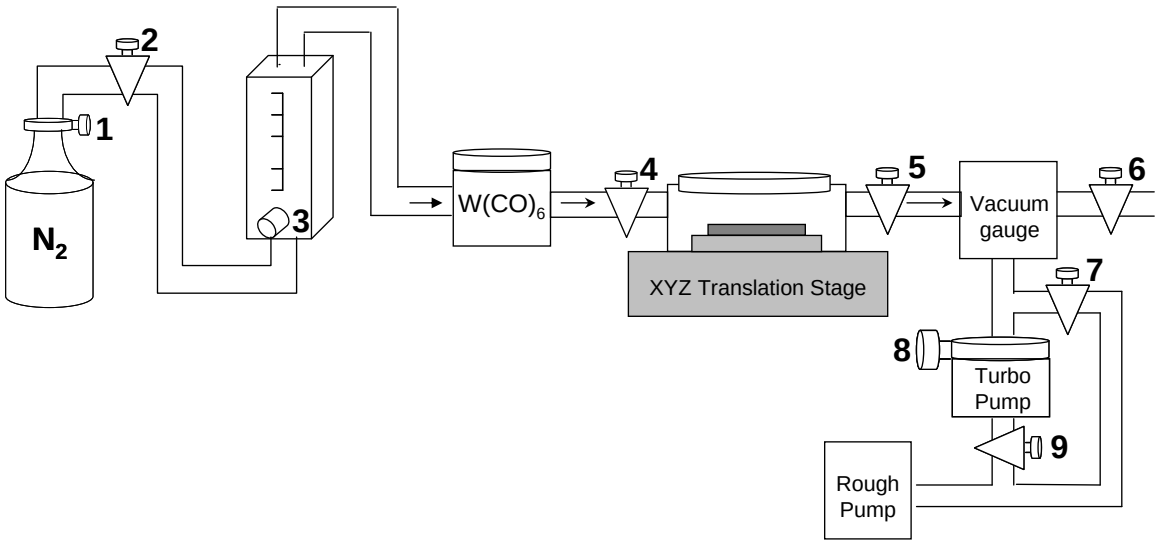

Figure 3.7 Schematic of the vacuum system. 1. Nitrogen gas tank regulator. 2. Nitrogen gas flow control valve. 3. Flow meter regulator knob. 4. Precursor control valve. 5. Reaction gas exhaust valve. 6. Vent valve. 7. Rough pump valve. 8. Turbo pump gas gate. 9. Connector between rough and turbo pump.

3.1.3 Motion Control

The vacuum chamber is attached to a two axis mirror mount which enables the adjustment of the substrate flatness. This method guarantees the consistency of the substrate staying in focus during movement. Before starting the experiment, the two axes of the mirror mount are carefully adjusted to make sure that all the four apex of a 1×1-mm square stays in the same focal plane when the substrate translates. After this adjustment, it was assumed that the substrate stays in the same focus condition during substrate scanning. The whole set was then mounted onto a three axis translating stage which can be controlled electronically (Aerotech). Two growth modes are involved during experiments: in the stationary mode, the substrate is exposed to the laser beam

under certain laser power level for a time interval administrated by the mechanical shutter installed in the beam path; while in the scanning mode, the substrate is translated with respect to the laser focus at a designated scanning speed and direction programmed by the built-in control software of the translation stage. Both the stage movement and shutter status are controlled and synchronized by computer.

3.2 Substrates preparation and experiment procedure

In this dissertation, the study is carried out mainly on c-plane sapphire substrate [Al_2O_3(0001)], while other substrates were also involved, including insulators, semiconductors, and metals. Detailed information on substrates will be introduced in later chapter. Substrates are cleaned right before the experiment by the following procedure before introduced into the vacuum chamber: ultrasonically cleaned with acetone for 20 minutes, followed by submersion in isoproponal bath for 20 minutes, then blow dry with high purity nitrogen gas.

The daily experiment procedures are as following:

1. Warm up laser by turning on the chiller, turning the laser control knob to “on” position; and open the shutter;
2. Clean substrate as described in substrate preparation section;
3. After laser warms up, mode-lock the laser and optimize the output;
4. Adjust the optics to make sure the laser beam goes through the center of the two irises installed on the SHG rail-rack;
5. Insert the BBO crystal into the SHG station, adjust its position and angle to optimize the output (400 nm) power;
6. Adjust the mirrors after BBO to make sure the beam is centered at the

entrance of the microscope objective;

7. Close valves 7 and 8; Open valve 6, after the vacuum gauge read reaches the air pressure, close valve 6. Slide the glass window out and clean it with acetone; load the substrate in; replace the glass window;
8. Fully close valve 9, and open valve 7, let the rough pump pumping the system to a relatively low pressure;
9. Bring the substrate to the focus plane of laser beam, check the flatness of the substrate, using the two knobs of the mirror mount to adjust the flatness;
10. Open valves 1-5 in descending order;
11. Check the flow meter; readjust the regulator to make the gas flow stays at 20 SCCM, it might take several minutes;
12. When the gas flow is stabilized, and the vacuum reading reaches to 10^-2 Torr, close valve 7; Fully open valve 9, and gas gate 8;
13. Start the experiment. During which the spectrum of fundamental laser, flow of nitrogen gas need to be monitored carefully.

To finish the experiment, the procedures are:

1. Turn off the laser by closing the shutter, and turning the control knob to standby position; shut down the chiller;
2. Close valves1-4 in ascending order; leave valve 5 open to let the reaction residue gas pumped away for certain time;
3. Turn off all monitoring devices;
4. Close valve 5;
5. Adjust the stage to bring the reaction chamber far from the objective;

6. Close the valves 7 and 8; Open valve 6, after the vacuum gauge read reaches the pressure, close valve 6. Slide the glass window out; take out the sample carefully; replace the glass window;
7. Fully close valve 9, and open valve 7, let the rough pump pump the system to a relatively low pressure;
8. Close valve 7, fully open valve 9 and gas gate 8.

3.3 Characterization methods and preliminary results

3.3.1 Characterization techniques

Samples are investigated using several examination tools. A CCD camera was mounted on the top of microscopy objective to monitoring the reaction on situ during experiments. Optical microscope was adapted to look at the finishing samples right after the experiments. Deposited areas are carefully marked providing convenience to later investigation equipments. The detailed morphology and physical attributes of the deposited nanograting were investigated using scanning electron microscope (SEM). The 3D profile of TNG was determined by atomic force microscope (AFM). Its material composition was analyzed using energy dispersive x-ray spectroscopy (EDX). These analyses are expected to provide insight into the physical and chemical attributes of deposited nanogratings.

3.3.2 Physical attributes of tungsten nanograting

3.3.2.1 Tungsten nanograting grown in stationary mode

Figure 3.7(a) shows a SEM image of a typical TNG under the stationary growth mode with a laser power of 19-mW and an exposure time of 4-sec, and Figure 3.7(b) shows an AFM image of a typical TNG grown under similar conditions along with its cross section

profile. Each tooth in the grating resembles willow leaf shape with long strips and pointing ends [Figure 3.7(a)]. The orientation of the grating teeth was found always parallel to the laser polarization; when the input linear polarization was rotated, the orientation of nanogratings rotated accordingly. The AFM profile [Figure 3.7(b)] indicates the thickness of the grating teeth, maximally around 20-30-nm, decreases monotonically from the center to the edge, consistent with the Gaussian intensity profile of the focused laser beam. The grating teeth have maximum line-width about 80-nm (λ/5) and average periodicity about 160 (λ/2.5) -180 (λ/2.2) nm. The dimension of the pointing ends is less than 50-nm. What noticeable in the AFM image is a shallow ring (< 5-nm) encompassing the TNG which could be tungsten deposition due to the first diffraction maximum of the focused laser beam[16].

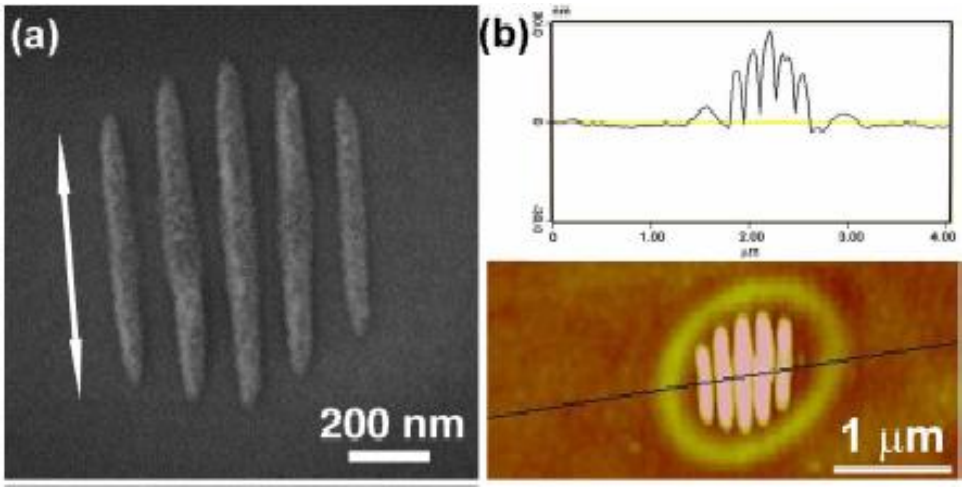

Figure 3.8 (a) SEM image and (b) AFM image and cross-section profile of a TNG deposited on sapphire substrate with a laser power of 19 mW and an exposure time of 4 sec.

3.3.2.2 Tungsten nanograting grown in scanning mode

In scanning growth mode, the substrates are translated with respect to the laser beam and this resulted in TNGs with excellent long-range spatial order. By controlling the laser polarization with respect to substrate translation direction, transverse or longitudinal TNGs can be obtained. Figures 3.8(a) and (d) show, respectively, the SEM images of typical transverse and longitudinal TNGs deposited on sapphire with a laser power *(P)* of 22-mW and scanning speed *(V)* of 0.8-μm/s. The insets indicate the relative orientations among laser incidence *(k)*, substrate scanning *(S)* and laser polarization *(E)*. As shown, the individual grating tooth for the transverse TNGs is short and resembles willow leaves, whereas that for the longitudinal TNG is long and extends along the scanning direction. The grating periods are around 165-nm in both cases. The corresponding AFM images and cross-sectional profiles are shown in Figures 3.8(b), (c) and (e), (f), respectively. Figure 3.8(c) reveals an almost constant tooth height of 16 $\pm$ 2-nm for transverse TNG, whereas the height of a longitudinal TNG tooth decreases from the center one to the edge (Figure 3.8(f)), same as the profile of the TNG grown in stationary mode.

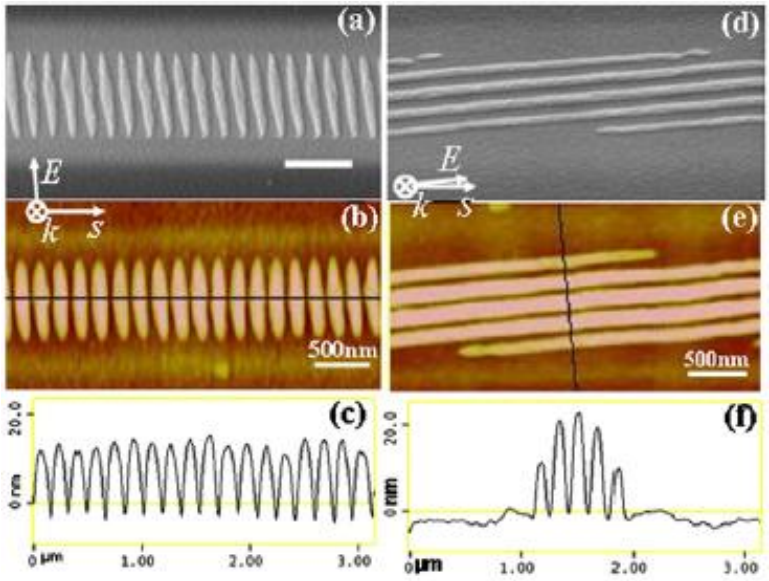

Figure 3.9 SEM images of (a) transverse and (d) longitudinal TNGs on sapphire at P = 22-mW and V = 0.8-µm/s. The scale bar represents 500-nm and applies to both SEM images. (b-c) and (e-f) are the corresponding AFM images and cross-sectional profiles for (a) and (d), respectively. In the insets, *k*, *E*, and *S* indicate the relative orientation of laser propagation, electric field of the laser, and substrate scanning, respectively.

3.3.3 Verification of tungsten growth

To verify the material composition of deposited pattern, energy-dispersive X-ray spectroscopy (EDX) study was carried out on bare sapphire, TNGs on sapphire, and tungsten microdot on sapphire (obtained by exposing the substrate to the laser beam for 2 minutes). All spectra were taken with electron beam energy of 20-Kev and a working distance of 10-mm. Figure 3.9 shows the EDX spectra along with insets of corresponding SEM images. The black line which corresponds to the bare sapphire substrate clearly indicates background peaks of O, Mg and Al from the substrate and Au from the coating. In addition to those above-mentioned peaks, the red line which corresponds to the TNG shows a small yet clear signal of W. To further verify this additional peak is due to W, EDX was also carried out on a micron size dot with a deposition time of 2-minutes where substrate stayed stationary. Much strong W peaks are observed at the same position as

indicated by the blue line, which confirms the extra peak in the blue line is indeed tungsten. A small carbon peak was also found in this case and is due to the formation of unsaturated metal carbonyls and the dissociation of CO, which is commonly seen in photolytic LCVD of metal carbonyls[16]. The weak W peak detected with TNG is mainly due to the fact that the thickness of TNG are only about 20-nm as determined by the AFM study, and that TNG only covers partial portion of the detection area. The above EDX study confirms the deposition of tungsten.

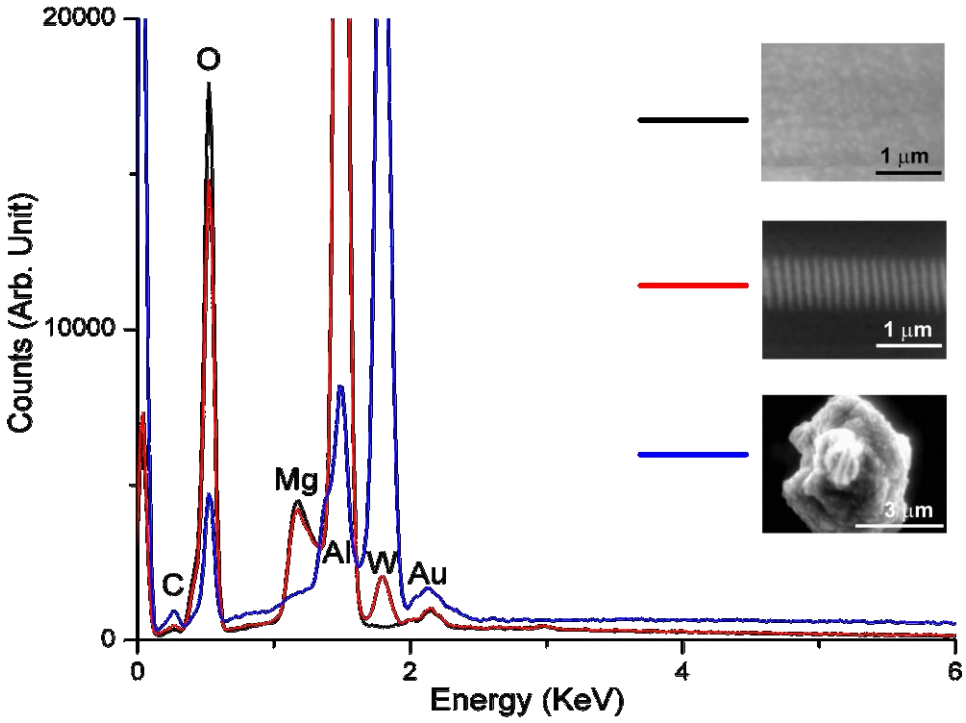

Figure 3.10 EDX spectra on bare sapphire substrate (black line), tungsten nanogratings (red line), and tungsten micron-sized dot (Blue line). Insets are corresponding SEM images.

CHAPTER 4 : CHARACTERISTICS OF TUNGSTEN NANO-GRATINGS

This chapter presents the detailed characteristics of self-assembled tungsten nanograting. Systematic experiments on parameters that could affect the formation and properties of TNG were conducted and the results were presented in this chapter. The studied parameters included laser power, exposure time/scanning speed, laser polarization, and laser wavelength. These factors control the morphology of individual grating teeth and the periodicity of the grating. This study provides mechanism on controlling the TNG.

4.1 Laser power and exposure effects

4.1.1 Evolution of TNG in stationary mode

Dot array written with varied laser powers and exposure times shown in Figure 4.1 was produced to study the effects of these two factors on the TNG formation in stationary mode. It was found that a laser power threshold around 17mW was required for the nanograting to grow on sapphire substrate, below which no grating was found for an exposure time over 10 sec, except for a thin tungsten film inside the exposure area. For laser powers equal to or greater than 17mW, on the other hand, nanogratings were well established in less than 2 sec (not shown in the picture).

The grating teeth grew larger and higher with increasing exposure time at a constant laser power, and eventually a flake-like structure appeared on top of the gratings. The

flake structures were always distorted and less dense than the underlying gratings and could be easily scratched away by AFM tips (contact mode).

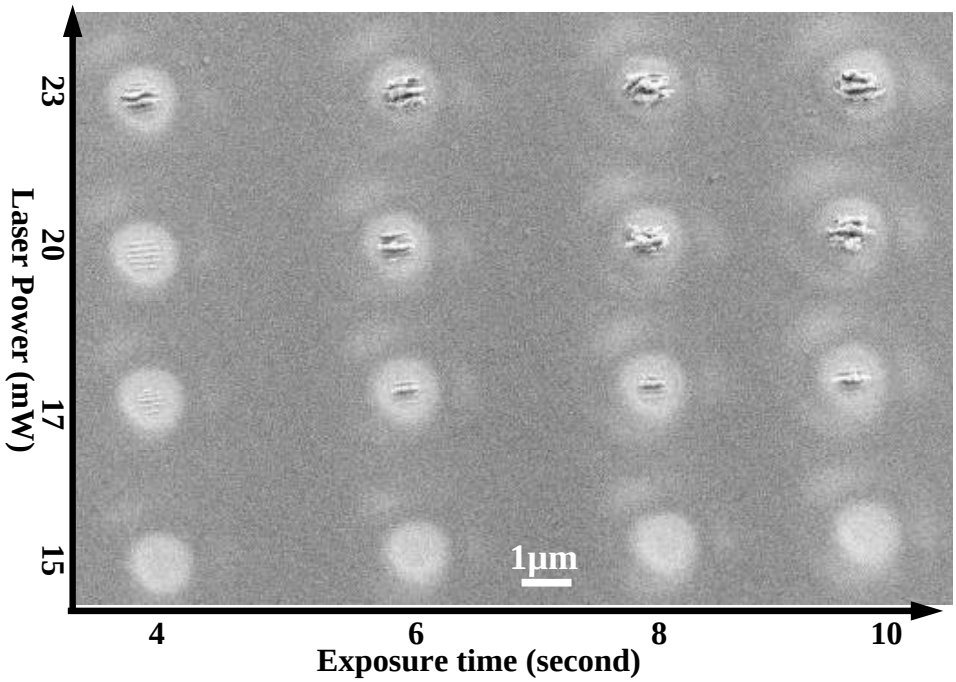

Figure 4.1 SEM image of a dot array grown on sapphire with different laser power and exposure time.

The higher the laser power, the faster the transition from neat grating to flake structure. Figure 4.2 shows the time evolution trend, and Figure 4.3 shows the laser power effects on TNG growth at constant exposure time. For example, at laser power equal to 20-mW, 2-sec exposure time produces clear and neat grating structure (Figure 4.2A), with 4-sec exposure, the center tooth grows much taller and forms flake structure (Figure 4.2B), with two more seconds, flakes almost cover the entire structure as shown in Figure 4.2C. With laser power of 25-mW, the flake structures start to occur at exposure time of 2-sec as shown in Figure 4.3C. In addition to the growth of flake structures, the number of grating teeth increases steadily as the increasing of laser power: there are 4

teeth in Figure 4.3A, 5 in Figure 4.3B, and 7 in Figure 4.3C, as the power changed from 17-mW to 23-mW and to 25-mW with the same exposure time. This observation is consistent with the threshold phenomena described earlier. With a fixed laser focus spot size and threshold required for grating growth, higher laser power covers a larger area within which the laser power is above the threshold and hence more grating tooth develop. This provides a possibility to make large area grating structure with a single exposure.

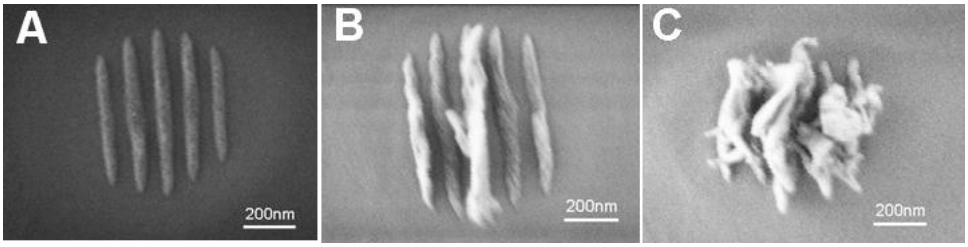

Figure 4.2 SEM images of time evolution of grating formation: (A) 2 sec, (B) 4 sec, and (C) 6 sec.

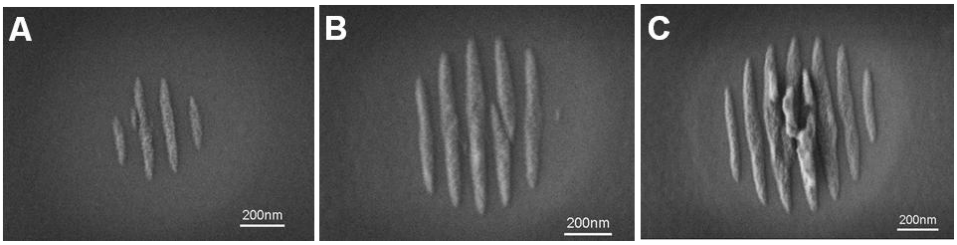

Figure 4.3 SEM images of power effect on grating formation: (A) 17mW, (B) 23mW, and (C) 25mW.

4.1.2 Evolution of TNG in scanning mode

Similar to TNG in stationary mode, the morphology of nanogratings also strongly depends on laser power and scanning speed in scanning growth mode. There is an operating window of laser power and scanning speed in which long range ordered grating structure can be produced. For conditions outside this window, the grating structure

exhibits discontinuity or overgrows into flake-like structure and loses the periodicity. The laser power threshold also applies to TNG formed in scanning mode. Figure 4.4 shows the longitudinal grating array on sapphire substrate written with different laser powers and scanning speeds. Under the five different laser power levels showed below, the nanogratings become discontinuous at the scanning speed of 0.8-μm/sec (Figure 4.4A-J). While with slower scanning speed, the nanogratings are covered with flake structure (Figure 4.4S-T, V-Y).

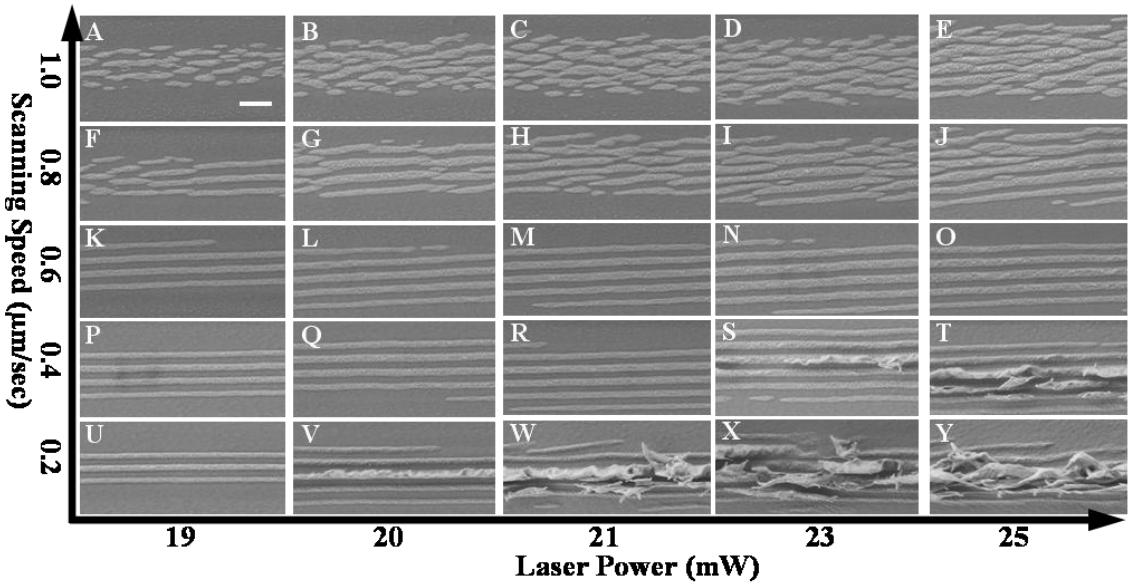

Figure 4.4 SEM images of longitudinal tungsten nanogratings on sapphire substrates grown at various laser power and scanning speeds. The scale bar is 500nm and applies to all images.

Figure 4.5 shows the transverse grating array under the same laser powers and scanning speeds as the longitudinal one. The data with 19-mW and 0.2-μm/sec was missing with this experiment run. Similar to longitudinal gratings, with slower scanning speeds, the nanogratings are covered with flake structure. Difference exists, however, with scanning speed at or higher than 0.8-μm/sec, at which the longitudinal gratings

become broken and disconnected, the teeth in transverse gratings stay ordered (Figure 4.5A-J). This implies that transverse grating is more robust against scanning speed than longitudinal one. This is most likely due to the nature of longitudinal grating require the teeth of TNGs connected along there longer axis as the substrate scanned cross the laser beam. If the displacement is larger than the grating teeth, then the teeth developed over adjacent exposure area won't be connected and thus appear broken.

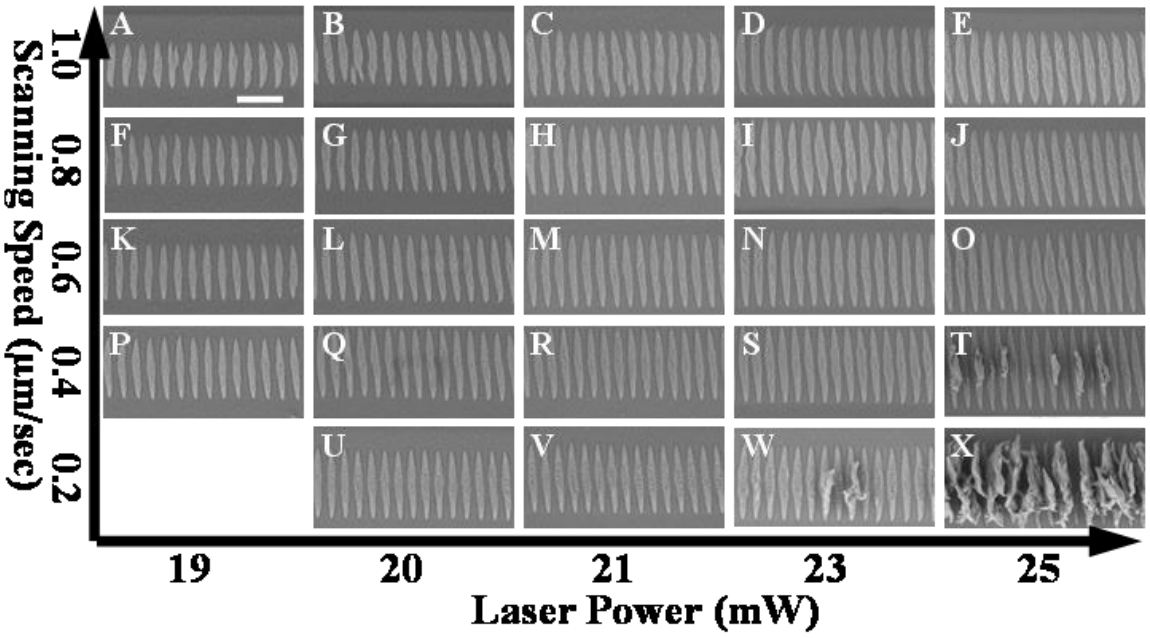

Figure 4.5 SEM images of transverse tungsten nanogratings on sapphire substrate at various laser power and scanning speed. The scale bar represents 500-nm and applies to all images.

To study the effect of laser power and scanning speed on TNG physical attributes and other properties, three typical transverse TNGs are taken out to compare side by side, as illustrated in figure 4.6. Figures 5.6(a)–(c) show SEM images of three transverse TNGs grown on sapphire under the conditions of P = 18-mW and V = 1.0-μm/s, P = 20-mW and V = 0.6-μm/s, and P = 24-mW and V = 0.4-μm/s, respectively. Comparing these

images reveals strong contrast: at low power and fast scanning speed, the teeth are short and sparse, whereas at high power and slow scanning speed the teeth are long and more closely packed.

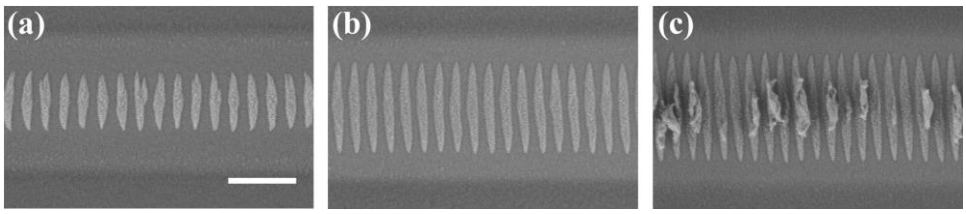

Figure 4.6 SEM images of TNGs on sapphire with (a) P = 18-mW and V = 1.0-μm/s, (b) P = 20-mW and V = 0.6-μm/s, (c) P = 24-mW and V = 0.4-μm/s. The scale bar represents 500 nm and applies to all images.

To study in detail the effects of laser power and scanning speed on the tooth length and period of transverse TNG, the critical step is measure the values correctly and more accurately. For tooth length, the mean value and standard deviation are calculated statistically from the numbers of more than 20 measurements of different individual grating teeth for each writing condition. The mean grating period values and the standard deviations are determined by the following procedure: (1) Based on the SEM images, the cross section profile is plotted (ImageJ). (2) The data of cross section profile is exported into data analysis software (Origin7.5). (3) Fourier transform of the data is performed. (4) From the Fourier transform result, the mean grating period and standard deviation are determined from the peak frequency and bandwidth of the FFT curve. Above description of the procedure determining the grating period and deviation is illustrated in Figure 4.7.

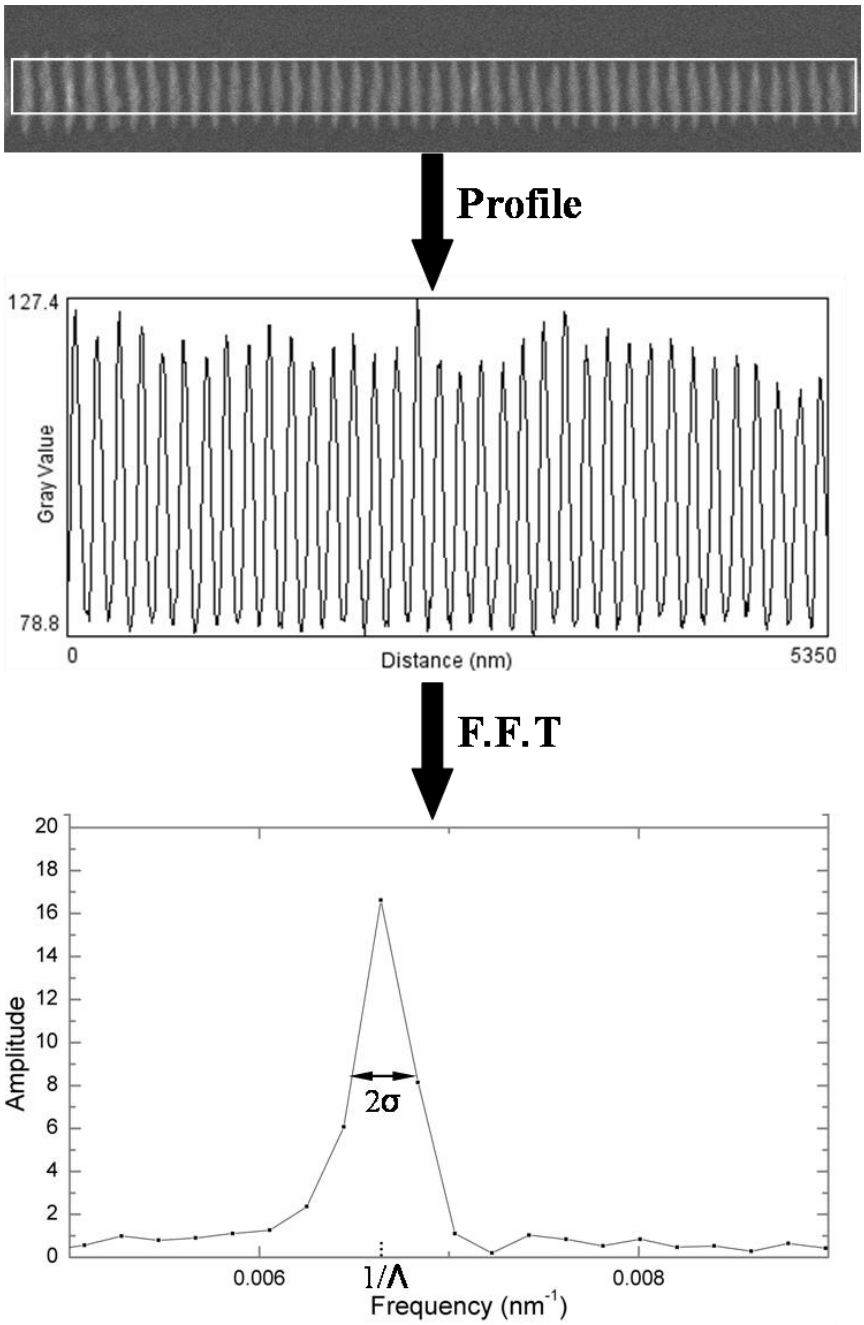

Figure 4.7 Schematic of grating period determination procedure.

Figure 4.8(a) shows the dependence of the tooth length of transverse TNGs on scanning speed for laser powers between 17-mW (threshold for TNGs growth on sapphire substrate) and 24-mW (maximum available power at the substrate). As shown,

the tooth length exhibits a monotonic dependence on laser power and scanning speed: at P = 20-mW, it decreases from 752±18-nm with V = 0.2-μm/s to 640 ± 15-nm with V = 1.0-μm/s; whereas at V = 0.8-μm/s, it increases from 540 ± 11-nm with P = 18-mW to 773±14-nm with P = 24-mW. On average, the tooth length increases more than 40% when power increases from 18-mW to 24-mW.

The grating period also exhibits a clear monotonic dependence on laser power and scanning speed, as shown in Figure 4.8(b). In contrast to the tooth length, the period increases with scanning speed and decreases with laser power: at P = 20-mW, it increases from 158 ± 2.5-nm with V = 0.2 μm/s to 172 ± 1.5-nm with V = 1.0-μm/s; whereas at V = 1.0-μm/s, it decreases from 185 ± 2-nm with P = 18-mW to 167 ± 1.5-nm with P = 24-mW. Figure 4.7 also reveals very good uniformity of tooth length and grating period: the standard deviation (one sigma) is between 1.5% and 4% for the former and between 0.75% and 1.5% for the latter. The variation in standard deviations does not depend on the laser power and/or scanning speed, and is likely caused by random fluctuations in local growth conditions such as substrate surface defects, laser power instability, laser focus drift, irregularity in stage motion, etc. Further improvement in uniformity may require substrates with better quality, as well as feedback control to stabilize laser power, scanning motion and laser focusing.

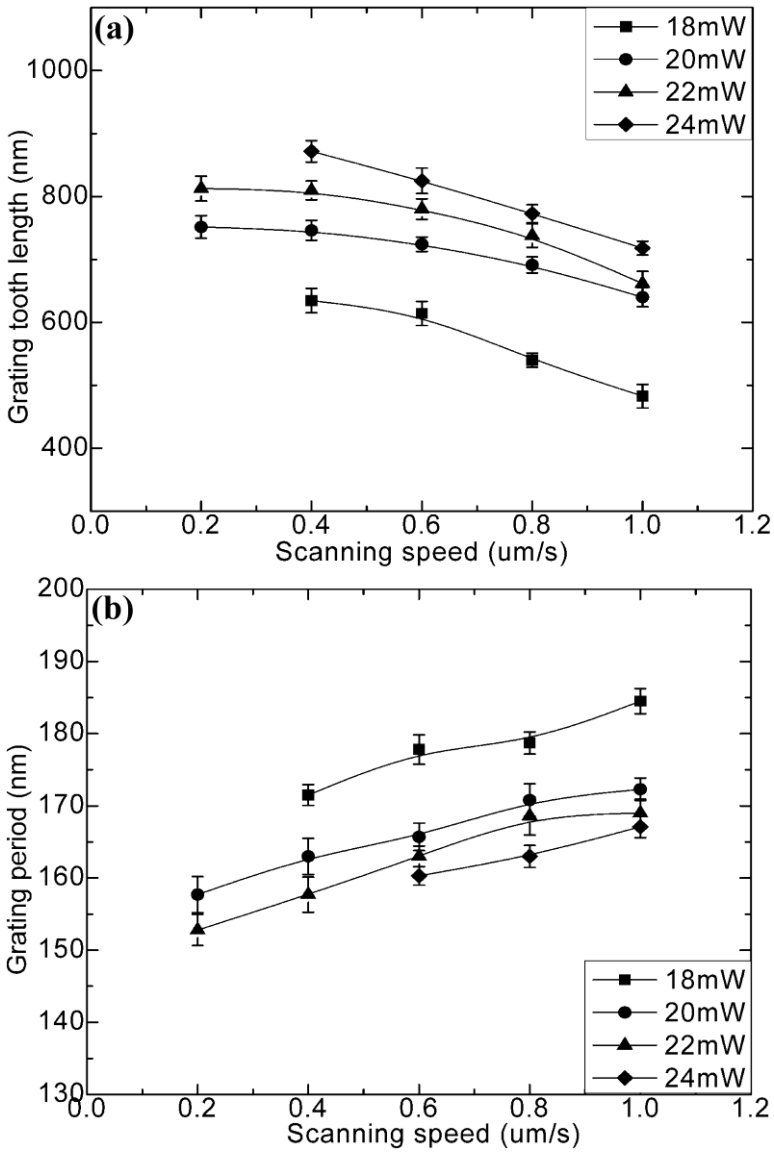

Figure 4.8 Dependence of (a) tooth length and (b) grating period of transverse TNGs on substrate scanning speed for different laser powers. The lines across data points are for eye guiding.

Unlike the transverse TNGs, the periodicity of longitudinal nanogratings varies from 150-nm to 165-nm on sapphire and is not dependent on laser power monotonically, as illustrated in Figure 4.9. However, scanning speed still affects the period slightly, slower scanning speed results in smaller period, similar to transverse gratings. But the effect is not as obvious as transverse one. The fact that transverse gratings are correlated to and more robust against scanning speed suggests there might be some coupling between the

growth of TNG and the relative motion between photons and substrate, when the motion direction is perpendicular to the TNG orientation which is determined by the laser polarization.

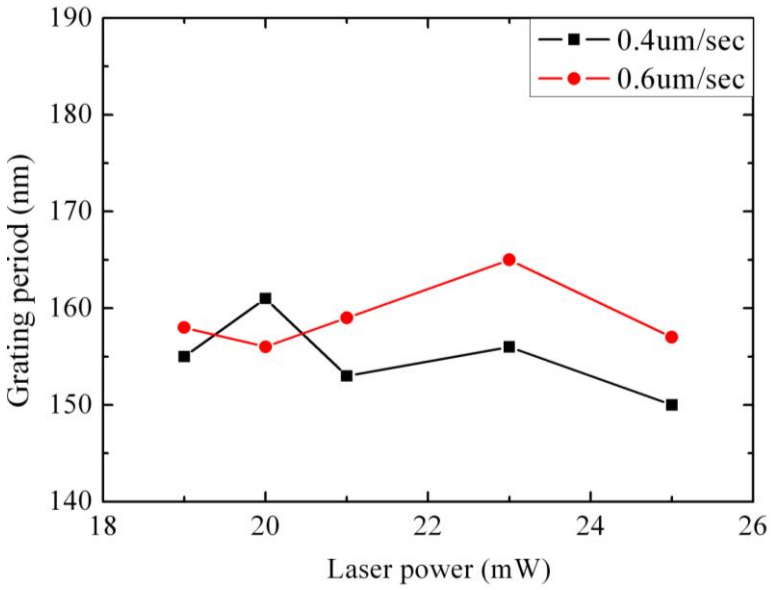

Figure 4.9 The relationship between period of longitudinal nanogratings and laser power for different scanning speeds.

4.2 Effect of laser polarization on tungsten nanograting growth

In this section, the effect of laser polarization state on the growth of TNG is studied. The first section discusses the growth morphology with rotating linear polarization. The second section discusses in detail the evolution of tungsten nanogratings when the polarization state changes from pure linear to elliptical and to circular polarization. These studies shed light to the mechanism of the formation of TNG.

4.2.1 Growth morphology with linear polarization

It was mentioned previously that the orientation of TNG teeth was parallel to laser polarization direction when the laser light is linearly polarized. This section studies the growth morphology of TNGs when the linear polarization direction rotates. The

polarization state of the fundamental laser output is fixed. In order to rotate the polarization direction, a combination of a half-wavelength wave-plate following a polarizer is used, as shown in Figure 4.10. When a linearly-polarized light purified by the polarizer is incident onto the half wave plate normally, and the optical axis of the wave plate is at an angle θ with respect to the polarization direction, as shown, the polarization state of the light emerging out the wave-plate remains linear polarization and gets rotated to an angle of 2θ respecting to the original polarization direction.

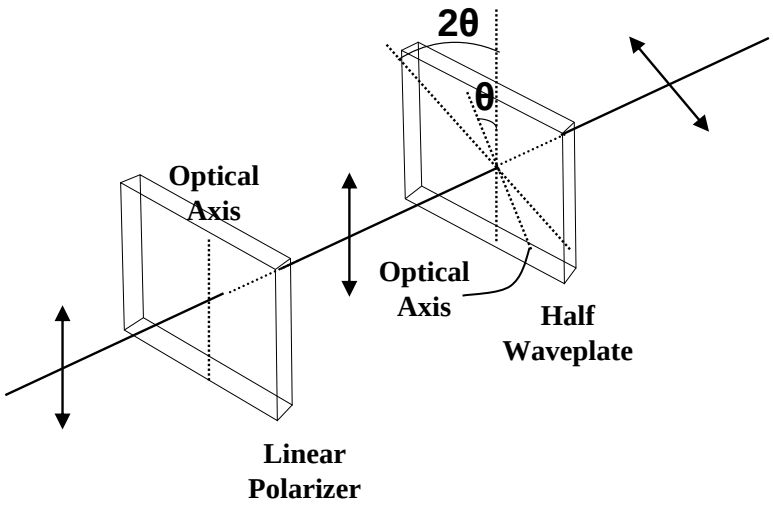

Figure 4.10 Schematic of rotating linear polarization direction.

Figure 4.11 shows an array of TNGs in stationary mode written with the same laser power of 17-mW and exposure time of 1-sec, but with rotating linear laser polarization directions as indicated by the white arrows. The result reveals that TNG is always growing along the polarization direction. Thus by managing the polarization direction, the orientation of formed TNG can be controlled precisely.

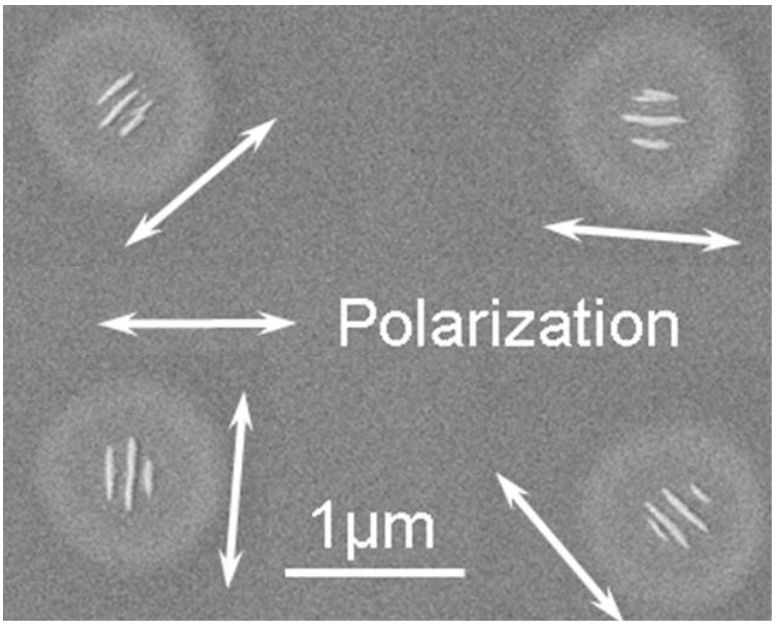

Figure 4.11 SEM image of a TNG array written with same laser power and exposure time but with rotating polarization direction. The white arrows indicate the laser polarization directions for each exposure.

This property of TNG can be used to generate arbitrary orientated long range ordered nanograting in scanning mode. By simply managing the angle between the polarization and scanning direction, tungsten nanogratings with each tooth orients along the polarization direction yet extend along the scanning direction can be produced. Figure 4.12 shows a set of grating structures orienting at different directions. The angles between the laser polarization (indicated by the white arrow) and scanning direction (indicated by the black arrow) are 0º, 30º, 60º, and 90º respectively in Figure 4.12A-D. This observation confirms that complicated 2D grating structure can be produced with this technique by simply arranging the angle between laser polarization and substrate scanning direction at designated position.

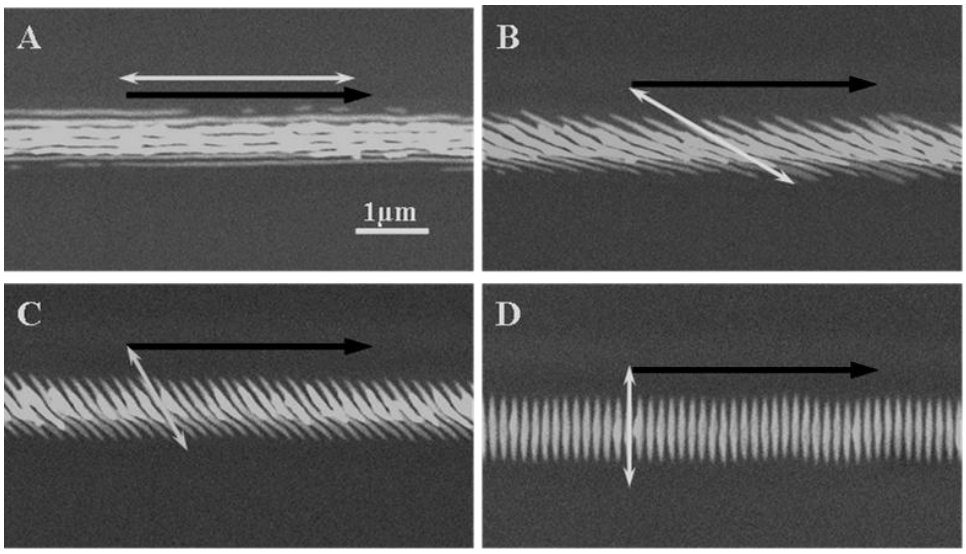

Figure 4.12 SEM images of tungsten gratings with different orientation. The angle between laser polarization and scanning direction are A) 0º, B) 30º, C) 60º, and D) 90º. The scale bar applies to all the images. White and black arrows indicate the direction of laser polarization and substrate scanning directions, respectively.

4.2.2 Polarization state evolution of TNG

The preliminary data shows that the formation of TNG is only observed with linearly polarized laser beam; with circular polarization, on the other hand, there is no evidence of TNG growth. Figure 4.13 shows two SEM images of tungsten deposited on sapphire substrate with laser power of 18-mW and 5-sec exposure time in stationary mode. With linear polarization, we observe TNG grating with flake structures as seen previously (shown in Figure 4.13B). Figure 4.13A shows a cluster of 2D dot array inside the exposure center grown with circularly polarized laser beam and exhibits no periodicity. The thickness of deposited pattern is very small with circular polarization comparing to linear polarized light with the same exposure conditions, indicates that the growth rate of tungsten under circular polarization laser is much lower.

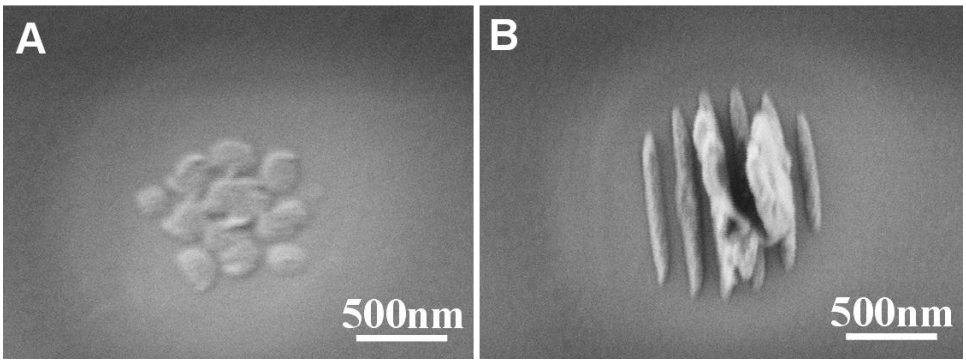

Figure 4.13 SEM images of polarization dependence study. A) Circularly, and B) linearly polarized light.

To further study the effect of laser polarization state on the formation of TNG. Experiments were extended to study in detail the growth change when the laser polarization is changing from pure linear to elliptical and to circular polarization. A quarter wave-plate following a polarizer can change the polarization state, as illustrated in Figure 4.14. The linearly-polarized light (after the polarizer) is incident onto the quarter wave plate normally, and the optical axis of the wave plate is at an angle θ with respect to the polarization direction, as shown. After passing through the wave plate, the original polarization is changed depending on the angle θ. For instance, when the angle is 0-degree or 90-degree, the polarization state passing through the quarter wave-plate remains linear; if the angle is 45-degree, the output polarization state changes to circular; and for angles in between, the output polarization state is elliptical, with the electric field component along the fast and slow axes of the polarization ellipse can be calculated for a given angle.

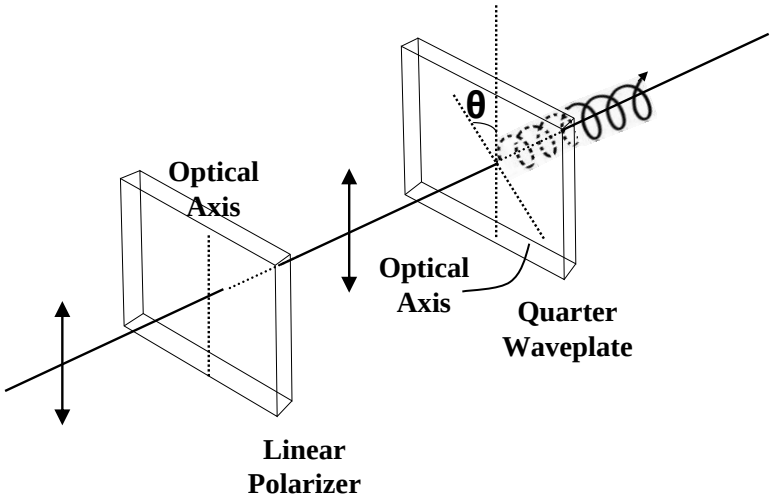

Figure 4.14 Schematic of changing polarization state.

The typical experimental results in stationary mode are shown in Figure 4.15. Initially, the quarter wave plate is aligned in the way that the optical axis is along the direction of the linear polarization, so the output polarization remains unchanged. The result is identical with the one that produced without the existence of quarter wave plate (the top image). Then the quarter wave plate was rotated such that the optical axis has a certain angle to the original linear polarization direction clockwise and counter-clockwise. It is interesting to find that the formation of TNG is not only occurring under pure linear polarized light. With elliptical polarization, the formation of TNG is also observed, and it orients parallel to the long axis of the polarization ellipse. The TNGs produced by left and right hand elliptical polarization are mirror images of each other. Comparing to the grating produced with linear polarization, the individual grating teeth become wider and blunter as the angle increases. When the angle approaches 45-degree, i.e., elliptical polarization becomes circular polarization, it is confirmed that the grown nanostructures are cluster of many dots and exhibit no periodicity.

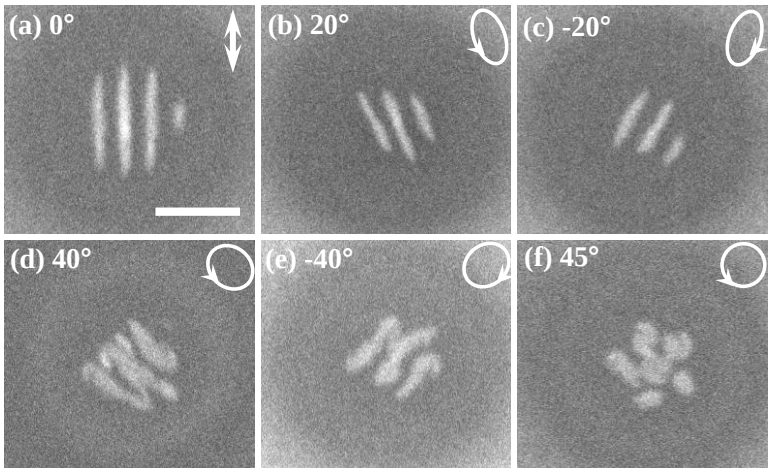

Figure 4.15 Evolution of TNG growth as polarization state changes. The rotating angles of quarter wave-plate and the corresponding polarization states are denoted in the figure.

By scanning the substrate cross the fixed laser beam, long-range ordered TNG can be produced, and the results are shown in Figure 4.16. Similar to the results in rotating linear polarization in scanning mode, the formed TNG orients parallel to the long axis of the polarization ellipse, and as the angle increases, the neatness and orderliness of the grating reduces. With circularly polarized light, i.e. when the angle approaches 45-degree, the formed structure doesn't possess any periodicity.

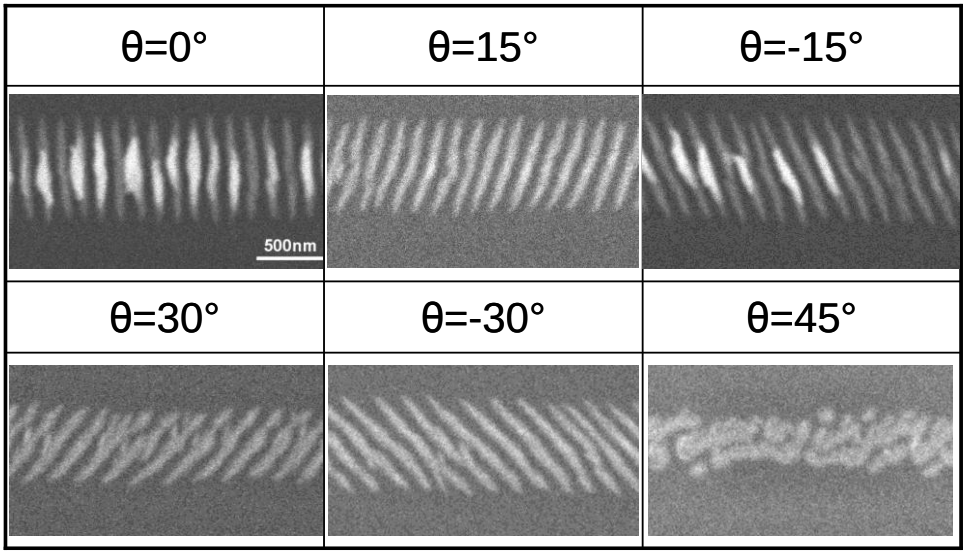

Figure 4.16 SEM images of TNG written on sapphire with elliptically polarized laser beam, θ is the angle between the optical axes of quarter wave-plate and the polarizer. Scale bar applies to all images.

It would be informative to verify if polarization affects the grating period or not. To do this, a set of TNGs written with the same laser power of 27-mW and scanning speed of 1-μm/s are taken out for comparison. Grating period here is defined as the normal distance between two adjacent grating teeth. The mean grating period value and standard deviation is determined from the Fourier transform of the profile data acquired from SEM images. For TNG with arbitrary orientation angle, distance between the teeth along the scanning direction is determined first, then multiply the cosine of the rotating angle of the quarter wave-plate to get the grating period in normal direction.

It is found that the grating period Λ increases with the angle of the quarter wave-plate to the original polarization for given laser power and scanning speed, as shown in Figure 4.17. It has been reported previously that the period of TNG increased with scanning speed and decreased with laser power.

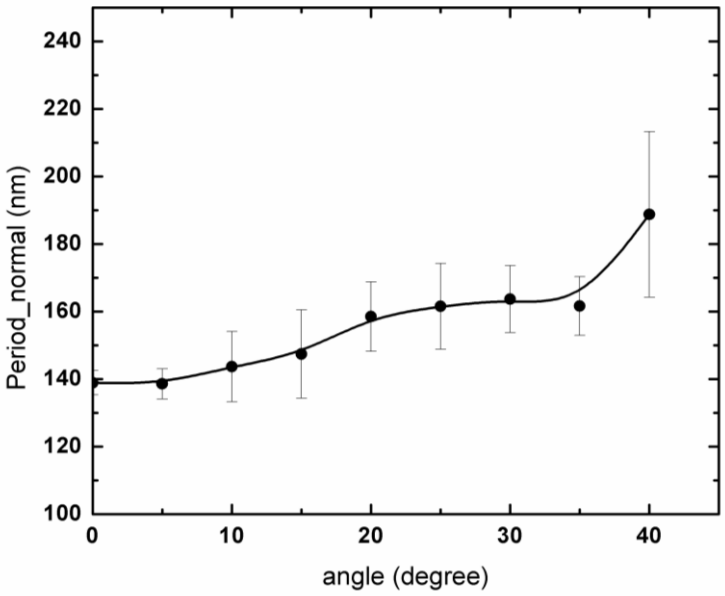

Figure 4.17 Relation between grating period in normal direction and the rotating angle of the quarter wave-plate. The line is for eye guidance only.

4.2.3 Cross polarization study

In this study, transverse or longitudinal grating was written at first, then the direction of laser polarization and/or scanning direction were rotated by 90-degree for the second scan. By studying the growth morphology at the overlapping area, the effect of existing grating structure on those grown in later stage could be revealed. Figure 4.18 illustrated four different cases of cross polarization scanning. In Figure 4.18 (a) and (b), the substrate was scanned left to right first, and then the laser polarization was rotated to the orthogonal direction then scanned the substrate back to the starting point with the same speed. The grating in Figure 4.18(c) was written with transverse grating produced first and then wrote another transverse cross the existing one, i.e., both the polarization and scanning direction were rotated 90-degree. Figure 4.18(d) was produced by a transverse grating written first, then wrote a longitudinal grating perpendicular to and cross the existing transverse grating, i.e., the scanning direction was rotated by 90-degree while the

polarization kept the same. It was found that at the interception area of two orthogonal gratings, quasi-periodic beads were filled in the gap between the grating teeth grown previously. And the existing grating teeth acted as a boundary that preventing the beads getting connected to each other. The orderliness of the filled beads was not well defined. As illustrated in Figure 4.18(d), when the second scan was along the extension of the grating teeth, the existing grating teeth provided seed and guided the growth of the longitudinal grating. The written condition for the longitudinal grating was chosen that no ordered grating could form. When it scanned close to the transverse grating, the new deposition lined up with the existing grating teeth and extended them for certain distance, and then the guidance was lost, and the longitudinal grating became disconnected again. This indicates that the exiting grating teeth enhance the deposition of tungsten at their tip when the polarization direction is parallel to laser polarization.

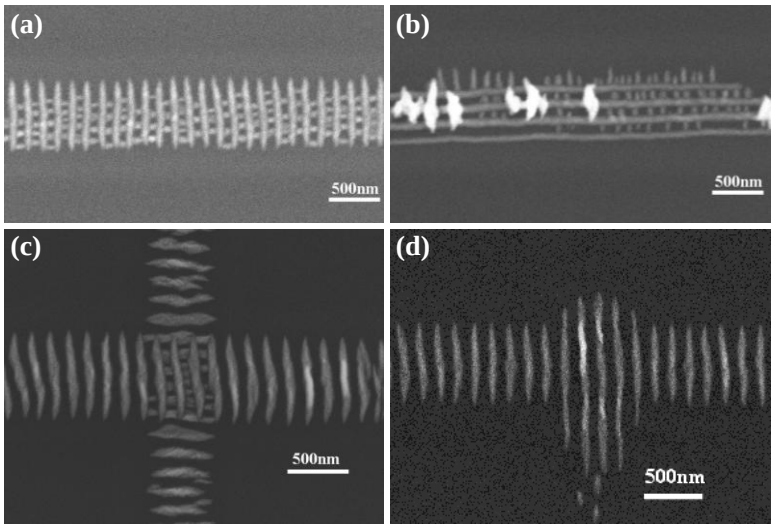

Figure 4.18 SEM images of tungsten nanograting written on sapphire with cross-polarization.

4.3 Dependence on laser wavelength

For periodic structure initiated by the interference between two waves, the periodicity usually correlates to the written wavelengths. To investigate if tungsten nanograting is originated from the interference between the incoming laser and another surface wave, it is critical to execute the wavelength study.

The first attempt was using the 800-nm fundamental laser beam directly. The results show that tungsten deposition can be induced by 800-nm light but at much higher powers than at 400-nm (about 3-4 times higher). Some of the results in scanning mode are shown in Figure 4.19. The deposited structures don't exhibit well-defined periodicity, neither as continuously grown film. When the laser power gets higher, similar flake structure grows on the top of underlying nanostructures. And when the laser power gets even higher as the growth rate becomes very large, the formed patterns are thick walls distributed periodically with periodicity about the laser wavelength, as shown in Figure 4.19(c).

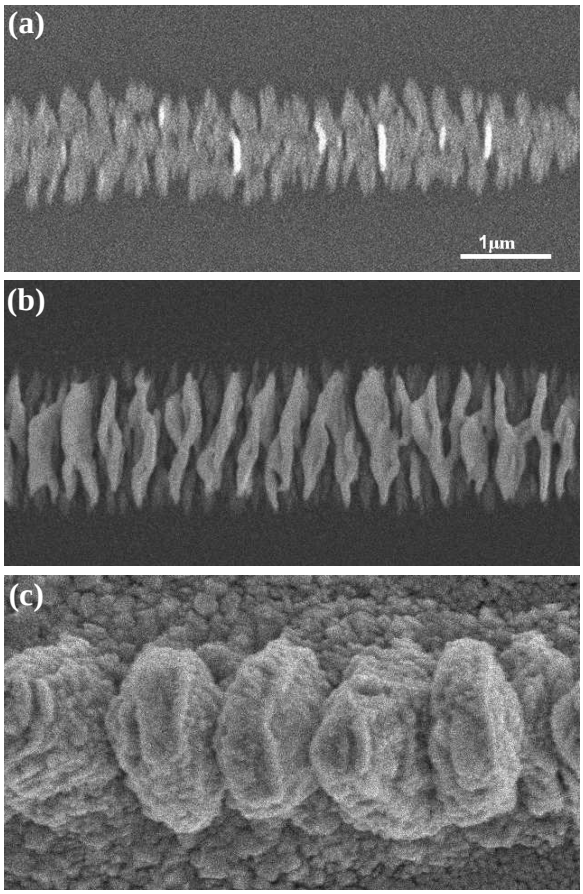

Figure 4.19 SEM images of tungsten deposition on sapphire substrate with 800-nm linearly polarized laser beam.

It is ideal to systematically study the wavelength over a large range. However, all the optics in current machining system are designated specifically for wavelength range at 375-425-nm; the microscope objective has very low transmittance for wavelengths below 400 nm, on the other hand. This made the wavelength tuning range very limited. To study the wavelength effect in a large range, optics for other wavelengths are needed. Two different wavelengths were involved in this study, 400-nm and 425-nm. For each wavelength, transverse nanogratings arrays were written with different laser powers and scanning speeds. The working window on written parameters varies for these two wavelengths. Figure 4.20 shows the preliminary results on the grating period versus

different scanning speed for wavelength at 425-nm and 400-nm. It was known that laser power had effects on grating period, to exclude the power effect in the wavelength study, for each scanning speed, the mean grating period and the standard deviation were obtained statistically from gratings written at that speed and all the powers that could produce ordered nanograting. It was then assumed the period of grating wouldn't exceed that range for each wavelength for a given scanning speed, independent on the wavelength. Thus the power factor was isolated in this study. It is easy to see that longer wavelength produce bigger grating period. Simple calculations reveal that the grating period actually scales to grating period linearly. Wavelength thus is an important control parameter of tungsten nanograting growth. Studies on larger wavelength range are critical to further confirm this observation.

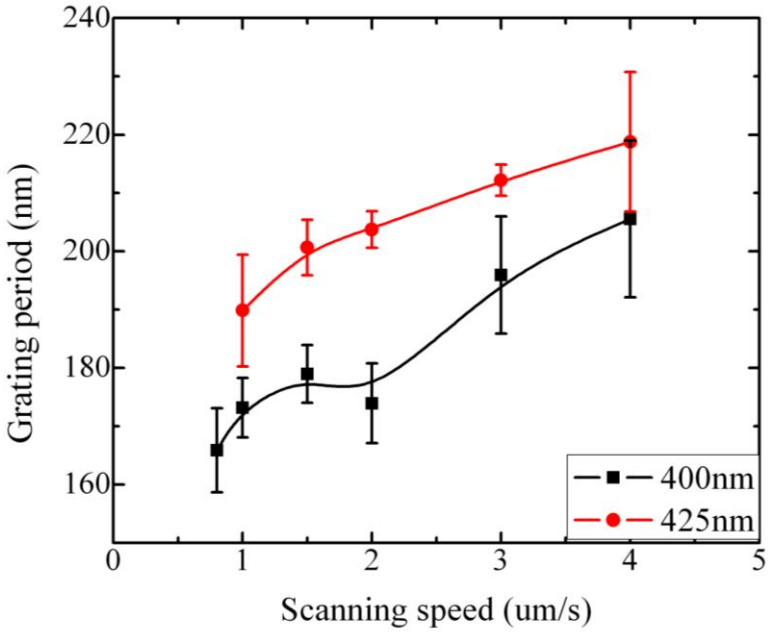

Figure 4.20 Grating period versus scanning speed for laser wavelength at 400-nm and 425-nm.

In summary, written parameters that affect the morphology and properties of tungsten

nanograting were studied experimentally in stationary and scanning modes. Laser power, scanning speed/exposure time, laser polarization, and laser wavelength are controlling factors on both the morphology of the individual grating teeth and the grating period. Complete knowledge on these parameters provides information on the mechanism of TNG formation and control method for practical application of TNG.

CHAPTER 5 : SUBSTRATE EFFECT ON NANOGRATINGS

In this chapter, detailed studies on the effect of substrate on TNG growth condition and physical attributes were presented. TNG growth was conducted on a wide range of substrates, including insulator, semiconductors, and metals. Line arrays were written on these substrates to characterize the impact of substrate on the formation of TNG.

5.1 Substrates and their material properties

Substrates involved in this study include insulators, semiconductors, and metals. Among the insulators, there are c-plane sapphire (Al_2O_3 <0001>, 2 sides polished, MTI corporation), z-cut quartz (SiO2 <111>, 2 sides polished, MTI corporation), fused silica (SiO_2, 2 sides polished, MTI corporation), calcium fluoride (CaF_2, <111>, 2 sides polished, MTI corporation), magnesium oxide (MgO, <100>, <110>, 2 sides polished, MTI corporation), and magnesium fluoride (MgF_2, <001>, 2 sides polished, MTI corporation), glass slide (SiO_2, Fisher Scientific). To determine the composition of the unknown glass slide, EDX analysis was performed on the substrate. It was found that the glass was mainly doped with sodium atom, as shown in Figure 5.1. The detected Au signal is coming from the coated Au film to eliminate the charging effect during SEM.Semiconductors include zinc oxide (ZnO, <0001>, 1 side polished, MTI corporation), gallium nitride (GaN, undoped, 5.7μm on sapphire, TDI), and aluminum nitride (AlN, 2 sides polished, Valley design Corp.). The metals, include gold (Au, 99.95%, Alfa Aesar), silver (Ag, 99.95%, Alfa Aesar), tungsten (W, 99.95%, Alfa Aesar),

and nickel (Ni, 99.95%, Alfa Aesar). Physical and optical properties of these substrates that might affect the growth of TNGs are summarized in Table 1.

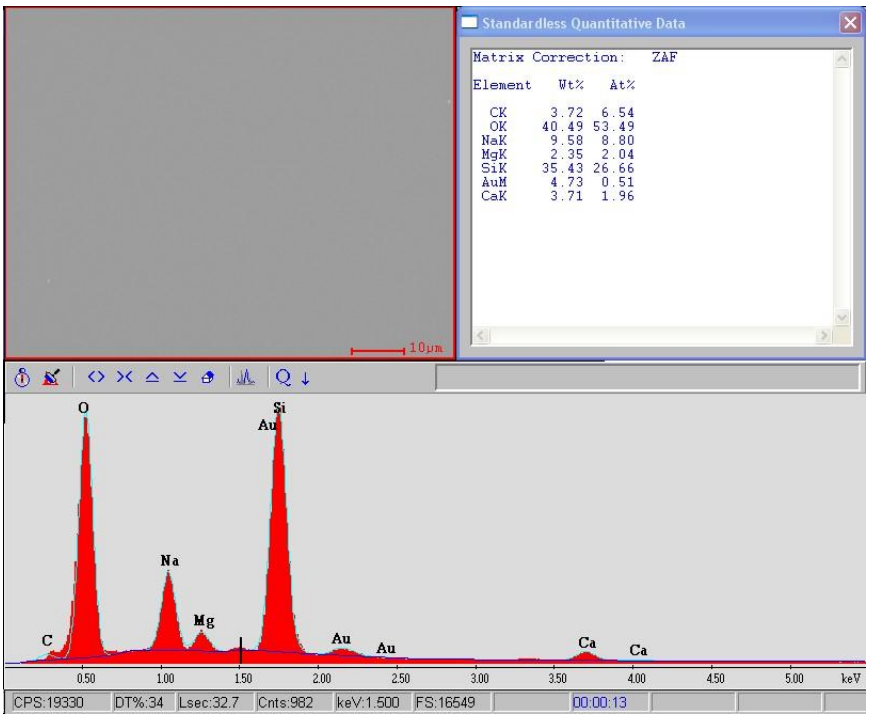

Figure 5.1 EDX spectra of the soda-lime glass substrate.

Table 1 Material properties of selected substrates involved in the substrate study.

Substrate	Refractive index	Band gap (eV)	Thermal Conductivity (W/m•K)	Heat Capacity (J/Kg•K)	density (Kg/m^3)
MgF2	1.38	10.8	14	1005	3180
CaF_2	1.44	10.96	10	854	3180
Fused SiO_2	1.47	8.5	1.38	703	2203
Soda-lime	1.53	9	1.11	858	2510
Quartz	1.56	10.1	9.5	733	2650
MgO	1.74		59	877	3580
Sapphire	1.78	9.1	42	750	3970
AlN	2.1	6.2	170	740	3260

5.2 Universality of tungsten nanograting

TNGs were observed on all the substrates listed above, to give some examples, Figure 5.2 shows SEM images of transverse TNG on four different insulator substrates and Figure 5.3 on four different semiconductor substrates with written condition denoted in the figures. This observation indicates that femtosecond laser induced self-assembly of tungsten nanogratings is a universal phenomenon. This universality is very important for practical application purpose. There was a Threshold laser power for each substrate. Flake structures were observed on all the substrates when laser power was too high or too slow scanning speed.

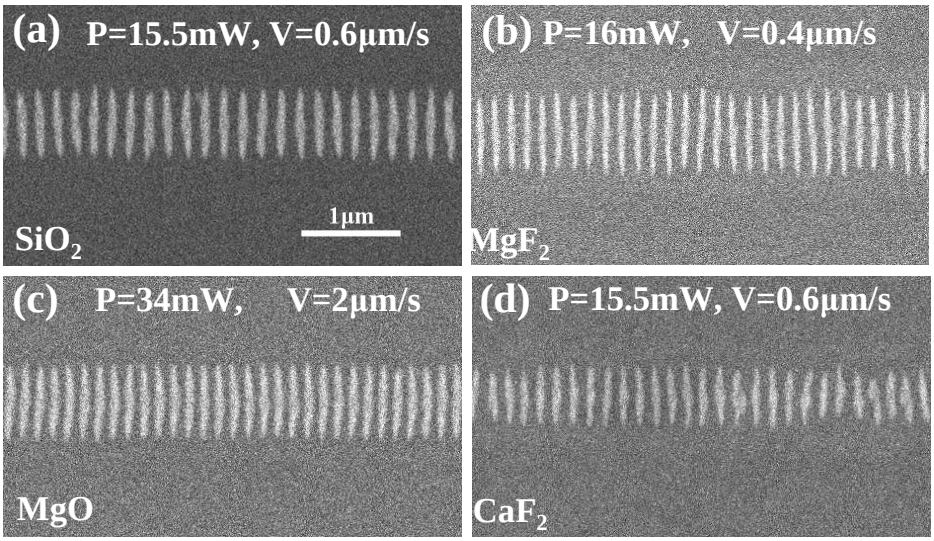

Figure 5.2 SEM images of transverse tungsten nanograting on (a) Fused SiO2, (b) MgF2, (c) AlN, and (d) CaF2 substrate. The scale bar applies to all images.

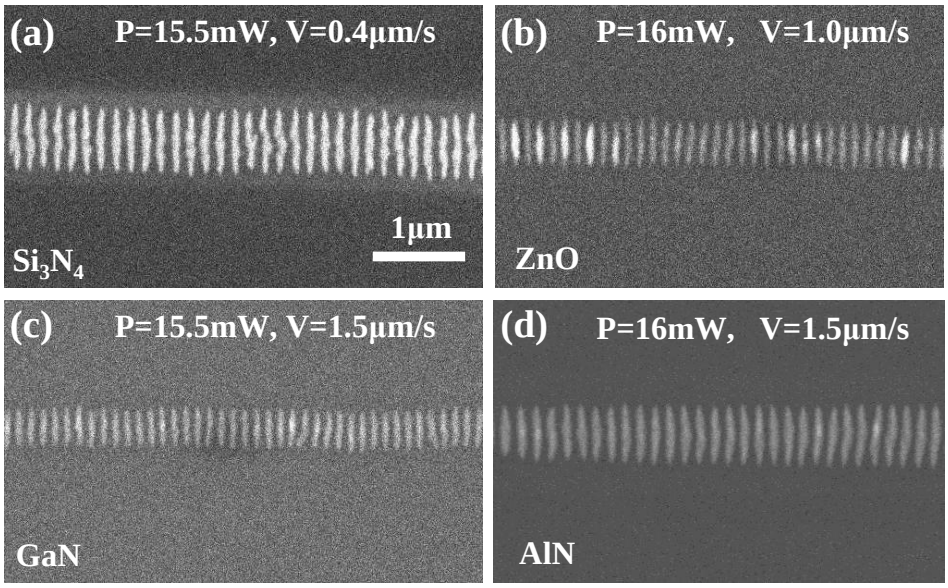

Figure 5.3 SEM images of transverse tungsten nanogratings on (a) Si3N4, (b) ZnO, (c) GaN, and (d) AlN substrate. The scale bar applies to all images.

Unlike the insulator and semiconductor substrate that has very flat surface, the metal substrates involved in this study have very rough surface with lot of defects and voids even after polishing, as shown in the top row of Figure 5.4. These defects on the substrate affected the growth of TNG a lot, as can be seen in the bottom row of Figure 5.4. The deposited patterns on these non-smooth surfaces were not well defined and the periodicity was hard to be determined. Nevertheless, the grown pattern intend to show periodicity and it was confident to expect ordered grating could grow on these substrates if much smoother surface condition can be provided.

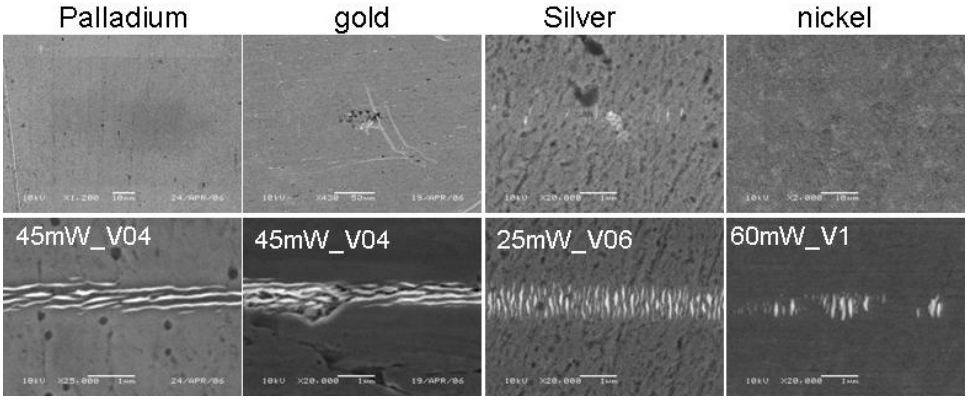

Figure 5.4 SEM images of surface roughness (upper row) of and TNG grown on (bottom row) palladium, gold, silver, and nickel substrate.

5.3 The dependence of TNG period on substrate

For each substrate, transverse TNG array with different laser power and scanning speed were written to study in detail the effects of laser power and scanning speed on the periodicity of TNG. The scanning speeds rang was extended from 0.2-μm/s to 5-μm/s. Detailed plots on grating period versus scanning speed for different laser power on each substrate can be find in appendix A. Figure 5.5-5.6 plot one typical data set for each substrate in group insulator and semiconductors, respectively. In general, insulators have larger working window for ordered TNG growth, and the period of gratings on semiconductors is smaller than that on insulators**.** Similar trend is observed on all the substrates that the grating period increases monotonically with scanning speed and decreases with increasing laser power. The details vary significantly from one substrate to another, however. For example, the grating period increases sharply at the scanning speed range of 0.2 – 1.0-μm/s on glass and fused silica, and after which the period value starts to saturate. While it rise slowly but consistently for magnesium fluoride and magnesium oxide till speed of 5-μm/s. The period tuning range is about 60-nm on glass, and is only about 15-nm on gallium nitride. Comparison of the data on MgO<100> and

MgO<110> confirms that the orientation of crystalline substrate doesn't affect the formation of tungsten nanograting and its properties.

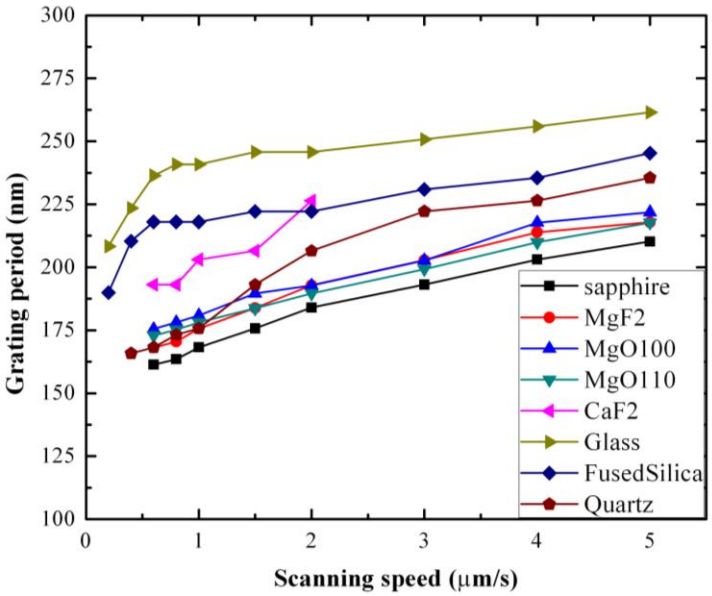

Figure 5.5 Plot of grating period versus scanning speed for different insulator substrates.

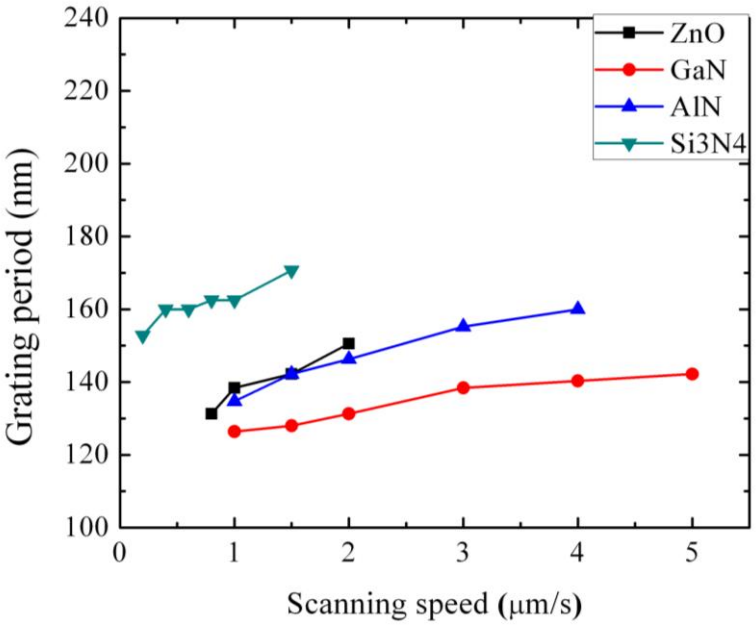

Figure 5.6 Plot of grating period versus scanning speed for different semiconductor substrates.

The effect of substrate on the grating period is studied on insulator substrate only due to the reality that the data points on semiconductor results are limited. One exception is aluminum nitride. It is included in this study since its 6.2-eV band-gap energy is twice the photon energy of 3.1-eV, thus it can be treated as a transparent substrate at wavelength of 400-nm. When study the effect of substrate on TNG period, since the scanning speed and laser power affect the grating period, and the growth condition varies for different substrates, it is necessary to define a parameter that can represent each substrate grating period while excludes the effects of scanning speed and laser power. Here we choose the period value when the scanning speed is equal to zero. This value can be determined experimentally, by emitting the laser beam onto the stationary substrate for certain amount of time. This method has some drawbacks, however. First, TNG intends to possess high orderliness when the substrate is scanning, and the grating teeth produced in stationary mode is not always well registered, they are usually misaligned or intertwined. Secondly, the number of grating teeth in a single exposure is very limit due to the small laser focus spot, and the value obtained in this way might have large error if only a few teeth are measured.

This value is determined mathematically in this discussion. It is extrapolated from the period-speed curve of each power on a substrate by fitting the curve mathematically. From the fitting parameters, the extrapolated period values at zero speed and the errors are determined. Most of the period-speed curves are fitted with exponential function defined as

$$\Lambda = P_1 + P_2(1 - \exp(-PV)) \tag{1}$$

where P_1 represented the extrapolated period at zero speed, P_2 is the saturate value that

the curve can reach, and P is the rising rate of the exponential curve. For some curves, linear function as following fit the data with smaller error than does the exponential function

$$\Lambda = P_1 + P_3 V \tag{2}$$

where P_1 again represented the extrapolated period at zero speed, and P_3 is the slope of the period-speed curve.

For all the curves on each substrate, the fitting parameters are summarized in Table 2.

Table 2 Theoretical fitting parameters for the period-speed data for different powers on wide-band dielectrics.

substrate	laser power	P1	error	P2	error	P3
MgF2	18.5	175.3	1.17	--	--	11.7
	24.7	152.6	1.9	81.9	3.4	--
CaF2	14.8	183.1	1.9	--	--	20
	15.4	176.9	4.9	--	--	23.1
Fused SiO2	15.4	193.3	7.8	45.6	7.5	--
	18.5	186.1	2.4	53.3	2.3	--
	21.6	174.9	2.6	69.2	2.4	--
Soda-lime glass	15.4	184.6	8.8	58.6	8.4	--
	18.5	181.6	4.1	65.4	3.8	--
	21.6	180.2	5.9	73.5	5.5	--
quartz	17	145.3	4.6	101.9	6.3	--
	18.5	145.2	4.7	101.5	7.8	--
MgO <100>	18.9	166.5	2.8	113.2	42.1	--
	21.6	162.9	2.1	78.2	24.2	--
	24.3	160.8	1.7	99.9	35.2	--
MgO <110>	18.9	165.1	0.6	134.5	17.5	--
	21.6	155.3	1	70	3.5	--
	24.3	150.5	2.8	55.8	2.3	--
Sapphire	21.6	148.7	1.4	84.8	5	--
	23.1	139.7	4.7	75.5	5.9	--
	27.4	140.5	2.4	62.2	2	--
AlN	30.9	141.9	2.3	--	--	15.6
	37	142.7	2.5	--	--	9.2

For each substrate, the values of P_1 are collected and averaged for all laser powers that can produce ordered TNGs. And the range of possible P_1 values for each substrate is represented by the error bar centered at the average P_1 value. For instance, there are three P_1 of 148.7±1.4-nm, 139.7±4.7-nm, and 140.5±2.4-nm on sapphire substrate for the power equals to 21.6-mW, 23.1-mW, and 27.4-mW, respectively, the average P_1 value is calculated to be 142.6-nm with a 15-nm error bar. This value then represents the grating period on sapphire substrate at zero scanning speed for all possible laser powers that can produce ordered TNG. By this method, the effects of scanning speed and laser power are excluded when studying the grating period as function of substrate material parameters.

One hypothesis is that the grating period depends on the refractive index of substrate inversely, as in the reports by some researchers on the formation of single laser beam induced periodic surface structures, which will be reviewed in next chapter. The plot of P_1 versus the refractive index of substrate as illustrated in Figure 5.7 says that it is not the case for TNG. In general, the grating period is larger for lower refractive indices and smaller for higher refractive indices. But there is not a monotonic trend found for all the materials. Among all the substrates, the grating period is the largest on fused silica substrate. From quartz to aluminum nitride, the refractive index increases about 30%, but the grating period almost stays the same. This study indicates that other material properties such as thermal conductivity, heat diffusion, etc. beside refractive index might play important roles in define the grating period during the self-assembly process.

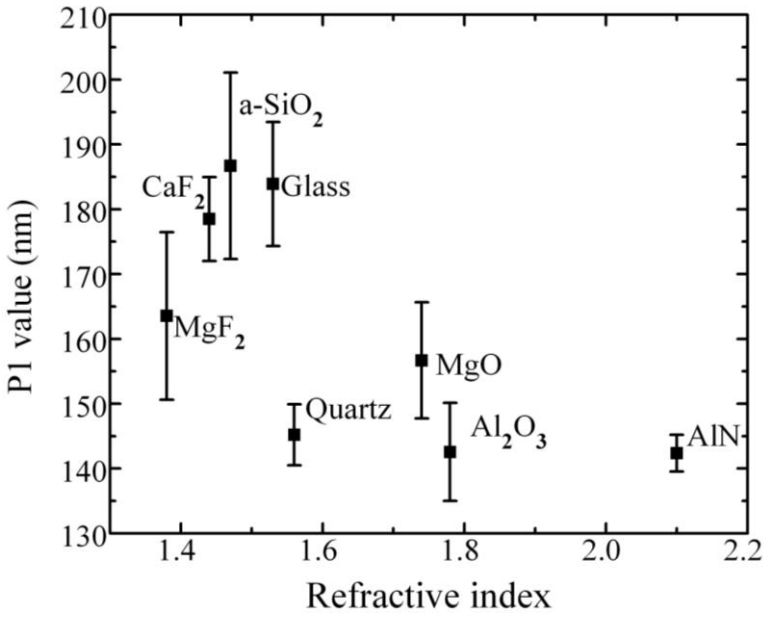

Figure 5.7 Plot of P_1 as a function of refractive index of substrate.

5.4 Effect of substrate on threshold laser power for TNG growth

As mentioned previously, the growth conditions of TNG vary with different substrates. Among which a valuable parameter is the laser power threshold for TNG growth. The threshold power is defined as the laser power at which ordered TNG starts to grow, and below which there is no observation of grating growth. SEM and AFM study reveals that there is a tungsten thin film about 10-nm grown on substrate for laser power under the threshold, and there is also a thin film underneath the formed nanograting when the power equals or exceeds the threshold. Figure 5.8 shows AFM images of a tungsten film (Figure 5.8 (a)) grows on sapphire substrate when the laser power (15-mW) is below the threshold power and a typical transverse TNG (Figure 5.8(b)) written with laser power of 24-mW and scanning speed of 1.0-μm/s. In both cases there is a thin layer of tungsten film. It is interesting to find that the deposited tungsten stripe has a concave profile in the lateral direction when the laser power is below the threshold. The reason for

the formation of concave stripe under such low laser power remains unclear.

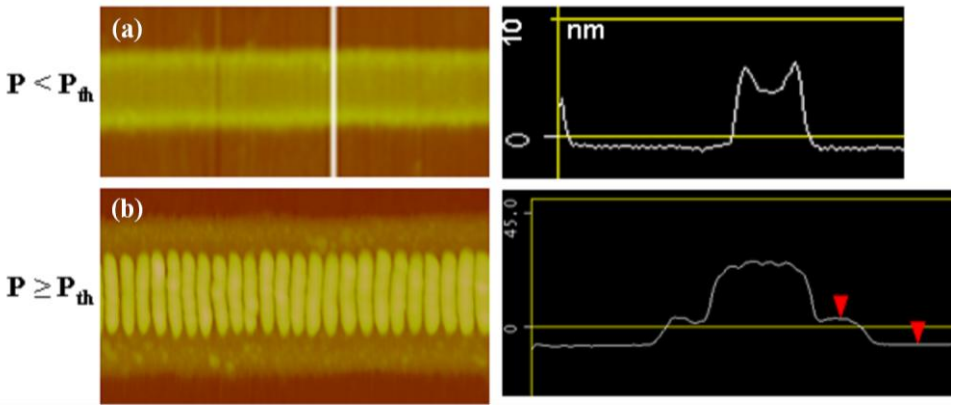

Figure 5.8 AFM images of (a) tungsten nanograting grown on sapphire substrate and its cross section profile, (b) tungsten stripe grown on sapphire substrate under laser power lower than threshold and its cross section profile.

The laser power threshold value is determined experimentally in the following manner: starting from the higher power, reduce the power each run until no grating growth is observed, then re-increase the power in smaller steps towards last power at which grating grows. By repeating above steps, a range with upper limit the minimum power at which ordered grating grows and lower limit the maximum power at which no grating grows is determined. This range is represented by the error bar in the plot and centered at the average value of these two measured powers, that average value is considered as the threshold laser power.

The growth morphology of TNG on all the substrates is similar in a way that TNG grows much higher than the surrounding background for laser power equals to or exceeds the threshold value, and a thin layer of tungsten can be detected for laser power lower than the threshold. But the threshold value varies from one substrate to the other. Among all the substrates, aluminum nitride has highest threshold power of 35-mW, while glass

has the lowest value of 14-mW. The theoretical discussion on laser threshold dependence on substrate is presented in next chapter.

In summary, detailed study on the dependence of TNG formation on substrate was reported in this chapter. The self-assembly of TNG was a universal phenomenon on a wide variety of substrates, including insulators, semiconductors, and metals. The grating period depends on the scanning speed and laser power similarly on all the substrate but detail varies. The threshold power value is also different for each substrate.

CHAPTER 6 : MECHANISM DISCUSSION

This chapter presents the mechanistic study on the formation of self-assembled tungsten nanograting induced by single femtosecond laser beam during laser chemical vapor deposition process. Conventional laser induced periodic surface structure and specifically femtosecond laser induced periodic structures and their corresponding theoretical models are reviewed. Theoretical explanation on the effect of polarization and substrate is presented. And a proposed theoretical model on the formation of TNG will be given at the end.

6.1 Periodic structure induced by a single laser beam

6.1.1 Laser induced periodic surface structure

Laser induced periodic surface structure (LIPSS) or ripples have been known since the invention of lasers [17]. LIPSS has been observed on metals, semiconductors and dielectrics. The conventional theory attributes LIPSS to the inhomogeneous energy distribution, due to the interference between the incident laser beam and a scattered (diffracted) wave near the interface[18]. Scattering of the incident light might result from the microscopic roughness of the surface, defects, or spatial variation in the dielectric constant. The period of ripples is given by: $\Lambda=\lambda/1\pm\sin(\theta)$, where λ is the laser wavelength, and θ the incident angle. The reported ripples usually orient perpendicularly to laser polarization, while parallel cases also exist under specific and rare conditions.

6.1.2 Femtosecond laser induced periodic surface structure

The study on LIPSS has been attracting more and more interests recently with the utilization of femtosecond laser beam. Sub-wavelength periodic structures were observed on various substrate surfaces induced by a single femtosecond laser beam [19-25]. A typical example reprinted from ref [19]is illustrated in Figure 6.1. Most of these features had orientation perpendicular to the laser polarization and can only be produced using amplified femtosecond pulses with pulse energy at least hundreds of nano-joules. Laser fluence, laser wavelength, laser polarization, incident angle and the number of admitted pulses or scanning speed are typical control parameters of FLIPSS.

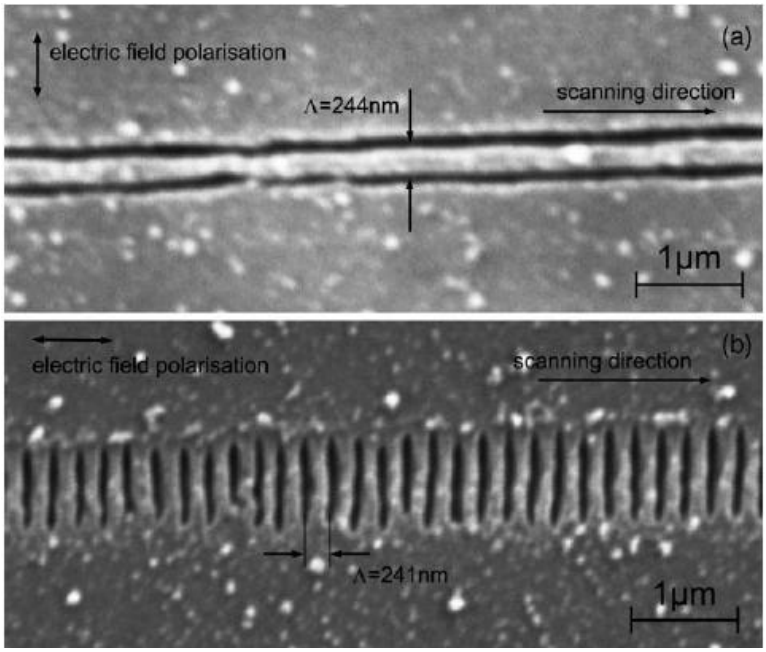

Figure 6.1 Ripples in fused silica with scanning direction (a) perpendicular and (b)parallel to the polarisation (SEM), l = 800 nm, tp = 100 fs, f = 1 kHz,d = 60 nm, Ep = 0.2 mJ. Reproduced under permission from ref. [19]. Copyright (2006) Elsevier.

Several authors have reported the dependence of nanoripples period on shot pulse number at a constant laser fluence. As the admitted pulse number increases, nnaoripples

in diamond-like carbon (DLC) film on silicon substrate grow wider, longer and better defined, the average spacing increases steadily at the same time[26]. Similar trends are observed on graphite substrate[27]. However, the evolution of the ripple period on tungsten surface as a function of the pulse number is opposite, their period deceases with increasing exposure[21, 24]. Reports on platinum and gold substrate[28] shown similar trend to tungsten. Differently, Wagner *et al.* reported that surface nanocracks produced by femtosecond laser ablation have a constant period that is independent of substrate scanning speed [19].

The dependence of nano-ripple period on laser fluence has been studied extensively on many materials, including ZnO [29], DLC [26], TiN [30], CrN [30], CaF_2[31], sapphire [32], tungsten[24], etc. The average period in CrN rises sharply and then experiences a slow increase as the laser fluence increases [30]. Other reports didn't show such sharp rise as in CrN[24].

Huang *et al* reported that the period of surface nanoripples on ZnO scaled linearly with laser wavelength over a big spectral range[29]. They also reported similar wavelength dependence of nanoripples on graphite substrate[27]. Controversially, wavelength and incident angle didn't have effect on the period of FLIPSS as reported by Costache *et al* [33].

Linear ripple structures were observed as long as the polarization was not circular, with which the formed patterns were isotropic spheres [29], it was in agreement with [22, 34] that no linear grating were observed with circular polarization. There are couple of reports claimed that even with circularly polarized laser beam, linear LIPSS orients at 45° [24, 35].

The conventional LIPSS theory failed to explain the new structures induced by femtosecond laser beam, as that femtosecond laser induced periodic surface structure (FLIPSS) always possesses deep sub-wavelength period (i.e. at least less than half the laser wavelength); While it would be predicted as equal to or larger than half the wavelength by conventional LIPSS theory. There are couple of reports adopted the conventional LIPSS theory by proposing the generation of higher harmonics of the wavelength during femtosecond laser interacting with the substrate, which resulted in ripple structure with much lower spacing than the wavelength [20, 25].

6.1.3 Self organization from instability induced by single beam

In the research area called particle bombardment, or particularly ion beam bombardment, the spontaneous pattern formation is a common phenomenon on the substrate surface. During the ion beam bombardment, it is known that nano-patterns on the surface in the form of ripples, bumps, or cones with typical scale on the order of 10-1000 nm could be produced [36-38]. Ripples formed on silicon surface produced with Ga^+ ions bombardment orient perpendicularly to the surface projection of the incident direction of ion beam, and their period increases with the exposure time and ion fluence[39]. Surface rippling is attributed to the competition between surface roughening and surface smoothing [36]. The interplay between these two effects leads to roughening instability which is responsible for the ripple formation.

Recently, Reif and his colleagues proposed that FLIPSS they observed on insulator surface is due to the roughening instability as result of the competition between surface roughening and surface smoothing [23, 40], by comparing the similarity between FLIPSS and periodic surface structure formed during ion sputtering. The similarities include laser

influence dependence, presence of bifurcation, substantial small feature size and ripple period comparing to laser wavelength. The surface roughening was caused by material erosion and surface smoothing is due to the atom diffusion[40].

6.1.4 Femtosecond laser induced periodic nano-cracks inside transparent substrate

It has been introduced that femtosecond laser can be focused inside transparent substrate and modify the material properties at focus without affecting surround area. Interestingly, sub-wavelength periodic structures could be produced in the form of nano-strips or nano-cracks within the focal volume, as was first demonstrated by shimotsuma *et. al.*[41]and later confirmed by Hnatovsky *et. al.* [42]. Typical experimental setup and results are shown in Figure 6.2. Bhardwaj et al claimed that the spacing of nanocracks inside fused silicon was independent on the energy of pulses[43], while it decreases with laser power when these cracks reside on the surface[44]. Shimotsuma et al reported nano-crack period increased with pulse energy and exposure time [41], which was supported by the observation in [32]. While in a separate study they reported the grating period decreases with laser power and increases with scanning speed[45]. The periodic nanocracks formed in fused silica were absent in BK7 substrate by any means of conditions as reported in [46]. Laser-induced plasma associated with dielectric breakdown in transparent substrates has been invoked to explain these observations. According to one model, the periodic nanocracks arise from interferences between the incident light and its scattered plasma waves [41]; according to another, they arise from the local field enhancement in inhomogeneous nano-plasma followed by a mode coupling mechanism that results in the periodic appearance [43].

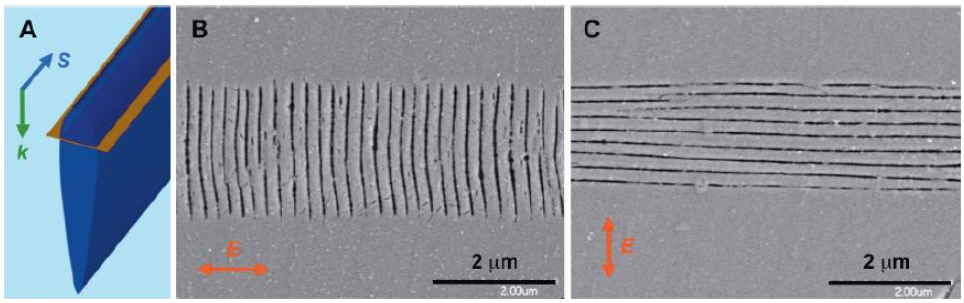

Figure 6.2 SEM images of self-organized periodic nanoplanes in the plane shown in Panel A (*x*-*y* plane in Fig. 1). Panel B: ***E*** is parallel to ***S***. Panel C: ***E*** is perpendicular to ***S***. Nominal separation of the grating planes is 250 nm. Reproduced under permission from ref. [47]. Copyright (2008) Wiley-VCH Verlag GmbH & Co. KGaA.

6.1.5 Periodic structure in metal film deposited by laser chemical vapor deposition

The discussed LIPSS above are typically surface ablation or bulk material phase transition and don't involve the growth of new material on an existing substrate. There are only a few reports of periodic structure formed during LCVD of metal films [48-50]. In LCVD-LIPSS, a deep ultra-violet light (257 nm) was used to induce deposition of metallic film on dielectric substrates. Periodic structures with varied periods (.(~ $\lambda/1.2$ to $\lambda/1.7$) started to appear as the metal film reach a thickness larger than hundreds of nanometers, and had orientation perpendicular to the laser polarization [49]. Such periodic features were attributed to the "stimulated growth" of a particular spatial component of small surface roughness that is selected by the phase-matching condition during light scattering at the metal surface. The scattering of the incident light via the surface roughness generates surface plasmon wave (SPW), which interferes with the incident light and produces standing wave pattern on the surface. Such surface standing wave induces periodic deposition of metal that serves as grating components to scatter more incident light into SPW. A positive feedback loop is thus established between the initial surface roughness and SPW, resulting in the spontaneous formation of surface

periodic structures [49].

6.2 Mechanistic study on the formation of tungsten nanograting

Although the above reviewed LIPSS and nanocracks share one common ground with TNG reported in this dissertation—they are all induced by a single laser beam. The big differences of TNG from other periodic structures make it a novel observation and require much more detailed study on the mechanism of its formation.

- TNG grows heterogeneously on substrates without an underlying thick tungsten film; while LIPSS and nano-cracks are either surface ablation or metal grating form on an existing thick metal film.
- TNG oriented always to laser polarization direction; while most of other periodic nano-structures ran perpendicular to laser polarization.

6.2.1 Formation of periodic surface structures in ablation case

To shed more light into the underlying mechanism of TNG formation, the first attempt was to verify if it was originated from the periodic surface rippling of the substrate by the laser ablation followed by deposition of tungsten thin film on the rippled surface, a control experiment have been performed. In which an amplified 400-nm femtosecond laser with up to hundreds of nano-joules in pulse energy was emitted onto bare sapphire substrates in air. The result, as shown in Figure 6.3(a), indicates clear evidence of laser ablation with sub-wavelength grooves that are somehow periodic and run perpendicular to the laser polarization. In a second experiment, we tested the hypothesis if TNGs are formed by laser-induced deposition of homogeneous thin film followed by laser-induced surface texturing. We did so by emitting 400-nm un-amplified femtosecond pulses onto sapphire substrates in air which was coated with thin tungsten film using sputtering

coating. No surface texturing is found at the laser power below 35-mW (notice that the threshold energy for TNG formation is 17-mW only); at pulse energy above 35-mW, ablation of tungsten film was observed, as shown in Figure 6.3(b), with sub-wavelength grooves that are quasi-periodic and again run perpendicular to the laser polarization. Both of them are in consistent with the FLIPSS reviewed in last section. We therefore conclude that TNGs are not originated from the rippling of substrate surface or tungsten film.

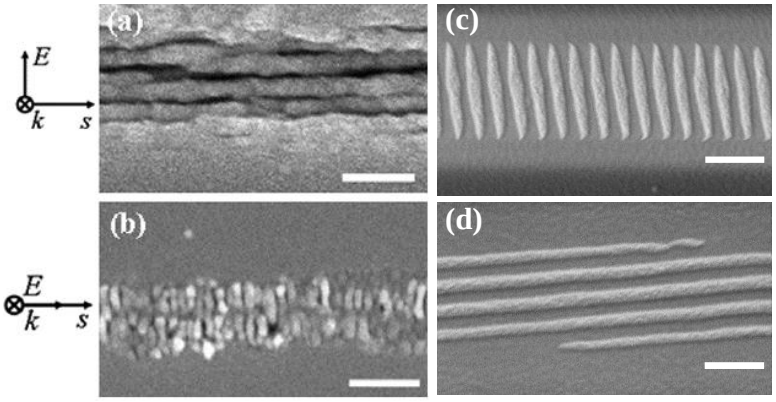

Figure 6.3 SEM images of ablated surface morphology of (a) bare sapphire substrate induced by 60-nJ femtosecond pulses from laser amplifier, and (b) thin tungsten film coated on top of sapphire substrates induced by 0.4-nJ femtosecond pulses, and (c) transverse and (d) longitudinal tungsten nanogratings grown on sapphire substrate. The scale bars in both images represent 500nm. The inset indicates the relative orientations among laser incidence (*k*), substrate scanning (*S*), laser polarization (*E*).

6.2.2 Growth of tungsten thin film and discussion on laser power threshold

It was found that the TNG formation is very sensitive to laser focusing condition respect to substrates. Transmission measurement of the 400-nm light through insulator substrate in the absence of precursor confirmed negligible absorption in sapphire substrate. Tungsten deposition induced by laser on transparent substrate should be a photolytic process at the early stage since the substrate doesn't absorb any light. The

photolytic deposition is initiated by the physisorbed reactant molecule layer absorbing multi-photons, in the evidence of sensitivity to laser focusing and the big difference between the dissociation energy of precursor molecule and the photon energy. After some time, there was a thin tungsten film formed on the substrate. AFM studied showed that the film thickness was about 10-nm, which was on the order of penetration depth of tungsten (13.2-nm at 400-nm).

6.2.3. The role of laser heating in the formation of tungsten nanogratings

This thin film started to absorb the laser light and the film temperature increases. Depending on the heat accumulation due to continue absorption of light and the heat dissipation into the substrate, the temperature of the metal film at the laser focus spot is different. The heat generated by laser is determined by the amount of absorbed laser power. The heat diffusivity among these substrates varies widely because of different thermal conductivity and heat capacity of substrates. Assuming there is a threshold temperature value required for TNG formation, for example, at that temperature fast growth due to pyrolytic LCVD takes off or the transition from uniform film to isolated islands occurs. To reach that threshold temperature, different amount of absorbed light thus different laser power is required since the heat diffusion varies for each substrate. This could explain why the threshold power for TNG formation is dependent on substrate.

To calculate the threshold temperature, by assuming the lateral heat diffusion can be ignored, we solve the one dimensional heat diffusion equation

$$\frac{\partial T(z,t)}{\partial t} = \alpha \frac{\partial^2 T(z,t)}{\partial z^2} \quad , \tag{6.1}$$

where $\alpha = \frac{\kappa}{\rho c_p}$ is the thermal diffusivity of the substrate and ρ, κ, c_p are the mass density,

thermal conductivity, and heat capacity of the material, respectively. The problem is simplified to one dimension, i.e. the lateral heat diffusion is neglected. It is also assumed that the temperature is the same in tungsten film due to its small thickness (10-nm), and the upper surface of the substrate T (z=0) has the same temperature as tungsten film. We have the following boundary and initial conditions:

$$\frac{\partial T}{\partial z}(0,t) = -\frac{I_a(t)}{\kappa}, \tag{6.2}$$

$$T(z,0) = 0, \tag{6.3}$$

where $I_a(t)$ is the absorbed intensity $I_a(t)=AI_{in}(t)$, where A is the absorptance of the system. The detailed derivation of absorptance A is also presented in Appendix B. From the derivation presented in detail in Appendix B, a simple relation between the threshold laser power and a substrate parameter S can be established as

$$P_{th} = C \cdot T_{th} \cdot S, \tag{6.4}$$

where C is a constant, T_{th} is the threshold temperature for TNG, and $S = \frac{\sqrt{\kappa \rho c_p}}{A}$ is a substrate variable whose value can be calculated for each substrate. Eqn.(6.4) states that the threshold laser power for TNG growth on each substrate is depend on the substrate variable S linearly. Figure 6.4 plots the experimental threshold power verses S for each substrate. It is interesting to find out that the data fall into two groups represented by red circles and blue squares. The red group includes glass, fused silica, quartz, Al_2O_3, which are covalent bounded materials, and the blue group consists of ionic bonded material including CaF_2, MgF_2, and MgO. Data in each group can be fitted with linear equation very well, and the slope of the fitting corresponds to the threshold temperature T_{th} for

each group. Comparison of these two slopes reveals that TNG formation requires higher temperature on covalent bonded substrate than ionic bonded ones. This could be explained by the fact that covalent bonds (50~110-kcal/mol) are generally stronger than the ionic bonds (4~7-kcal/mol). The offsets corresponding to S=0 for each group are almost equal (=13-mW) with less than 10% difference. This indicates that when there is no heat diffusion through substrate, the threshold laser power for TNG growth is a constant and independent on the type of substrate. This analysis is highly simplified, 3-dimensional study is essential for more rigorous model. All the parameters are assumed to be temperature independent, which usually are not in reality. Nevertheless, this study highlighted that laser heating playing an important role in the formation of tungsten nanograting.

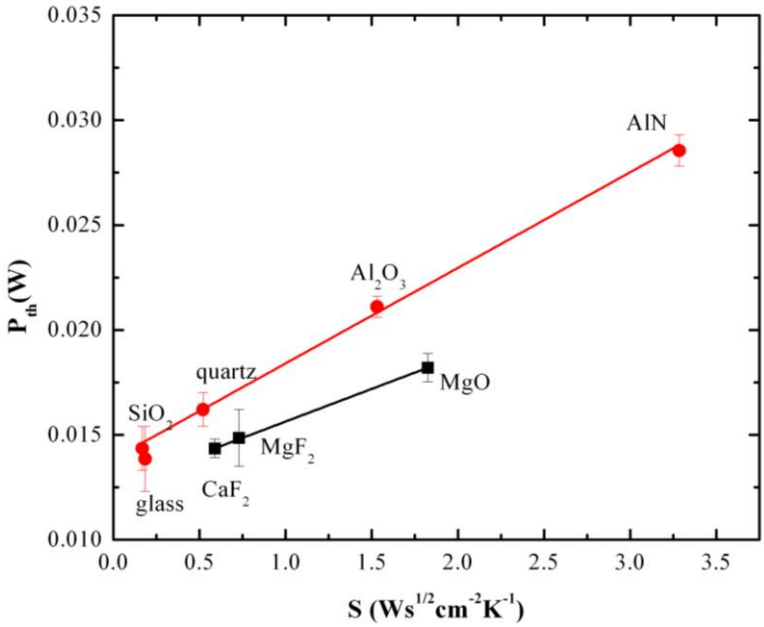

Figure 6.4 Threshold power of tungsten nanograting formation as a function of the substrate parameter S defined as in text. The lines cross data point are linear fit curves of each group.

6.2.4 Local field enhancement and asymmetric growth of tungsten nano-particle

When large nano-particle of tungsten appears either from the rapid growth at the center of laser focus, or from the deformation of the tungsten film due to laser beam induced instability, electromagnetic boundary conditions at the tungsten particle/dielectric interface lead to a field enhancement upon incoming laser beam. Chen *et al* presented the local field enhancement initiated the growth of photochemical deposited cadmium particle into elongate shape along the direction of laser polarization[51]. Figure 6.5 shows the normalized electric field energy density distribution above a tungsten nano-particle with 50-nm in diameter on the surface of semi-infinite glass substrate upon the excitation of 400-nm laser beam with different polarization states. The simulation is calculated using a three dimensional finite-difference time-domain (3D FDTD) method (Fullwave, RSoft). With linear polarization, the field is enhanced along the polarization direction or long axis of the polarization ellipse in elliptical polarization case (Figure 6.5(b-c)). The localized high intensity associated with the field enhancement could result in anisotropic growth of nano-particles into elongated shape along the strongest field direction, since photo-dissociation of $W(CO)_6$ is a nonlinear multi-photon process. When the field enhancement strength reduces, the individual teeth become wider and blunter. With circular polarization, the growth is isotropic along all the directions since there is no dominated direction of field enhancement (Figure 6.5(d)). This argument is consistent with the observation in Figure 4.14. It is also supported by the observation in Figure 4.17 (d) that existing tungsten grating teeth get extended orderly by newly deposited tungsten structures which would have been disconnected without the existence of the grating teeth.

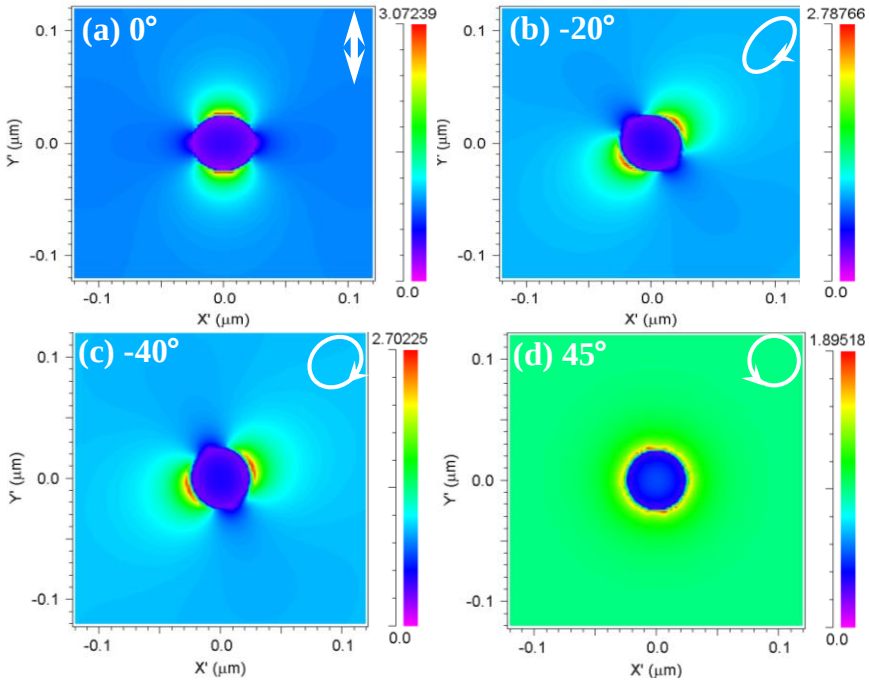

Figure 6.5 FDTD simulation results of the $|E|^2$ distribution at the surface of a 50-nm tungsten nanoparticle upon the excitation of 400-nm light with different polarization states**.**

The study of evolution of TNGs from disconnected nanostructures to highly ordered grating provides further information on its formation mechanism. Figure 6.6 shows transverse TNG on Silicon nitride (Figure 6.6(a-d)) and longitudinal TNG on sapphire (Figure 6.6(e-h)) with a fixed laser power but various scanning speeds v. When the scanning speed is too fast which corresponding to short exposure time per spot, discrete nano-particles are observed, this particles distribute with gaps in both horizontal and vertical direction with physical extension in laser polarization direction. As the scanning speed slowing down, i.e., the exposure time per spot getting longer, the extension becomes more obvious and the gap along the direction of laser polarization shrinks, due to rapid growth along polarization from the field enhancement. And eventually with slow enough scanning speed, the gap disappears and adjacent particles connect with each other in the direction of polarization and become a single grating tooth. The orthogonal gap

which is perpendicular to laser polarization remains almost unchanged throughout this process. That gap determines the ultimate grating period.

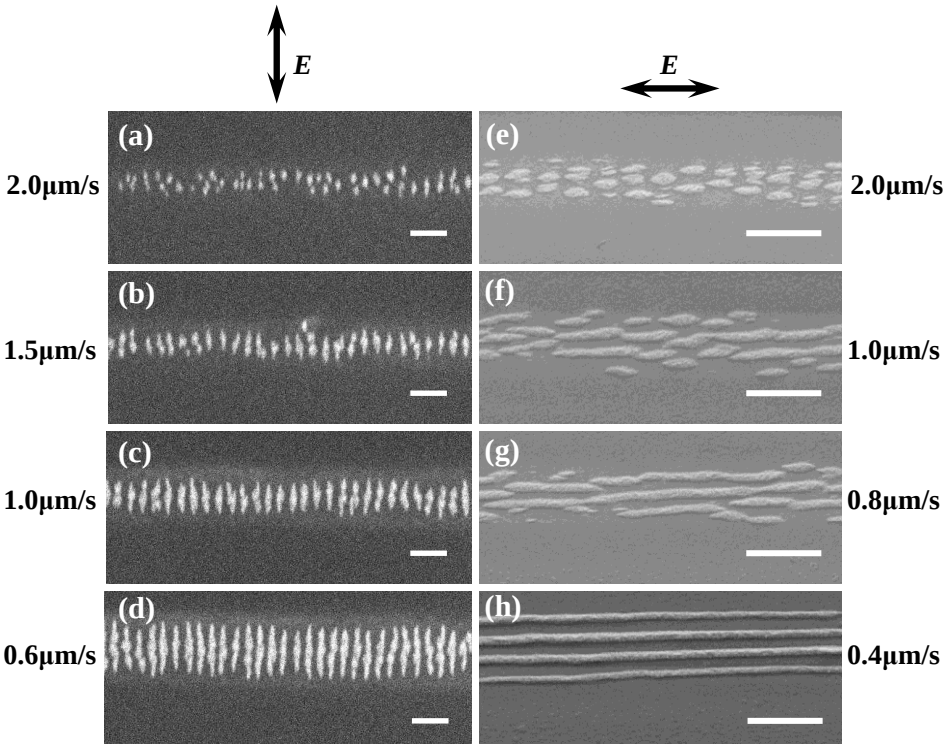

Figure 6.6 SEM images show tungsten nanostructure evolution on (a-d) Silicon nitride and (e-h) sapphire substrate with electric field and different scanning speeds as indicated. The scale bar in each figure represents 500-nm.

6.2.5. Conjectured mechanism on self-assembly of tungsten nanogratings

Putting above discussion together, here we propose a mechanism for self-assembled tungsten nanograting, as schematically shown in Figure 6.7. In the femtosecond laser induced chemical vapor deposition of tungsten from $W(CO)_6$ system, initially the laser pulses doesn't heat up the substrate since it is transparent to the substrate. But the laser intensity is high enough to induce photo-dissociation of the reactant molecules via multi-photon absorption. Tungsten film thus gradually grows on the surface. The film temperature starts to increase due to strong absorption of incoming laser by the film. At

the same time, the film is cooling down by transfer heat to the underneath substrate. The heat accumulation and dissipation through the substrate are competing. When the temperature of the film reaches a threshold value, the film then was assumed to undergo some roughening instability or stress relaxation process, during which 2D array of tungsten nanoparticles form. These nanoparticles have field enhancement along laser polarization upon the irradiation of incoming laser beam, leading to their elongated shape. The growth continues until adjacent particles are connected along the polarization direction to become a single grating tooth.

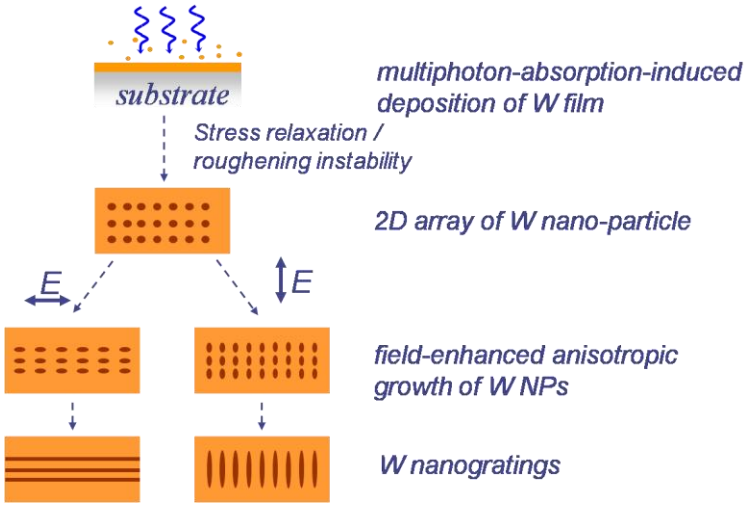

Figure 6.7 Conjectured model of TNG formation. The first one is side view of substrate while others are top views.

The gap between the particles in the direction perpendicular to laser polarization remains almost unchanged during these anisotropic growth processes and determines the ultimate period of the formed nanogratings. The experiment result that the period depends on the laser wavelength suggests the interference nature of TNG. The formed tungsten nanoparticles produce field enhancement and lead the anisotropic growth along the direction of laser polarization. On the other hand, the elongate shaped tungsten

nanoparticle acts as a dipole oscillator and radiates. The radiation field might be interference with the incoming laser beam and thus produce periodic interference fringes along the direction perpendicular to the dipole and guide the growth of adjacent nanoparticles. This process is shown schematically shown in Figure 6.8.

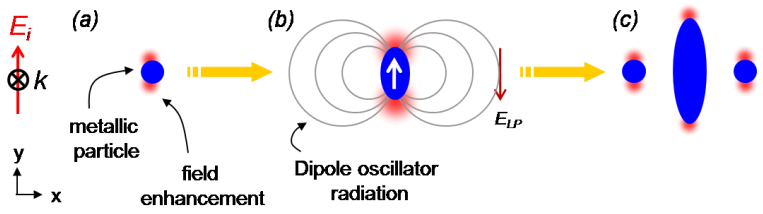

Figure 6.8 Conjectured model on grating period prediction.

The incoming laser beam can be considered as a plane wave propagating along z-axis and be expressed as

$$\vec{E}_i = E_i e^{-ikz}. \tag{6.5}$$

The field of the dipole radiation is

$$\vec{E}_d = \alpha \vec{E}_i \frac{\exp(-i(kx+\delta))}{x}, \tag{6.6}$$

where α is a scaling factor describe the strength of the radiation filed, δ is a phase delay between the dipole oscillator and incident laser beam. The radiation field is decaying along the propagation direction in order to conserve the energy. The total field at a point along x-axis thus is

$$\vec{E} = \vec{E}_i + \vec{E}_d = \vec{E}_i(1 - \alpha \frac{\exp(-i(kx+\delta))}{x}). \tag{6.7}$$

The minus sign is due to the fact that the field direction of the excited dipole is opposite to the incident field at the equator plane.

To produce constructive interference, the field intensity which equals to

$$\left|\vec{E}\right|^2 = \left|\vec{E}_i\right|^2 \left|1 - \frac{\alpha}{x}\exp(-i(kx+\delta))\right|^2 \propto 1 + (\frac{\alpha}{x})^2 - 2(\frac{\alpha}{x})\cos(kx+\delta) \quad (6.8)$$

needs to be maximum. The maximums occur when the value of the negative part in equation 6.8 is the smallest, corresponding to

$$Cos(kx+\delta) = -1. \quad (6.9)$$

By plugging k=2π/λ into Equation 6.9, we can therefore get the period of produced nanograting is

$$\Lambda = \frac{\lambda}{2}(1 - \frac{\delta}{\pi}). \quad (6.10)$$

Thus, for a given non-zero phase delay, the formed nanograting always possesses a period smaller than half the laser wavelength. This agrees with our experimental results.

This model, however, is very crude at this stage and more inputs are needed to complete it. For example, the nature of the instability remains unclear. The dependence of grating period on laser power, exposure time, and substrate could due to the fact that these parameters affect the phase delay δ. How do they related, however, requires more investigation.

In summary, the physical mechanism of tungsten nanograting formation was discussed. Initially, the photolytic deposition produced a tungsten film, which than started to absorb light and increase the temperature of the system. When a threshold temperature was reached, tungsten nanograting started to form from quasi 2D dots array. Field enhancement associated with the metal/substrate boundary favored the growth along the direction of laser polarization and resulted in the elongated grating teeth shape. The study of threshold laser power on each substrate revealed the importance of laser heating in the

process of TNG formation. A hypothesis on the mechanism of TNG growth was proposed, which were very crude and required further investigation.

CHAPTER 7 : FEASIBILITY AND POTENTIAL APPLICATIONS OF TNG

This chapter presents first the flexibility and scalability of tungsten nanogratings. Followed by nominating some potential applications of self-assembled tungsten nanogratings, its comparison with conventional nano-patterning techniques is also discussed in this chapter.

7.1 Feasibility and scalability of tungsten nanogratings

In this new tungsten nanograting deposition technique, multiple periodic tungsten lines grow on substrate with a single laser beam in single scan, thus the nominally serial nature of LCVD turns into a parallel approach with controllable orientation and spacing but without adding any instrumental complexity. Such unique properties offer capability to fabricate unique-shaped periodic structures in a single step. Figure 7.1(a) demonstrates a TNG with linear teeth embedded in a ring pattern produced with a laser power of 21-mW by translating the substrate at a speed of 1.0-μm/sec in an annular fashion while the laser polarization was held linearly and constant. The length of grating teeth is short when the scan direction is perpendicular to the laser polarization and becomes longer as the scan direction turns parallel to the laser polarization. It is interesting to point out that the grating teeth at the northwest and southeast portions of the circle fall on the same line, as indicated by the dashed lines in Figure 7.1(a). In another word, the spatial coherence between two physically separate TNGs could be preserved. Such unique property could be utilized to generate large-area gratings. The defect at the top corresponds to where the

fabrication starts and ends, and is due to the hysteresis of the translational stage which is expected to be corrected if a close-looped stage is used. Figure 7.1(b) demonstrates a writing of “UNCC” with embedded linear nanograting inside the scanning trace. These two examples demonstrate the capability of this technique to produce arbitrary-shaped linearly grating pattern by just programming the motion of the substrate. If a rotating stage or rotating polarization is adapted, complex patterns are believe to be generated in a simple manner. As an example demonstrated as radial and concentric LIPSS by manipulate the laser scanning direction always perpendicular or parallel to its polarization in a circular scanning [52].

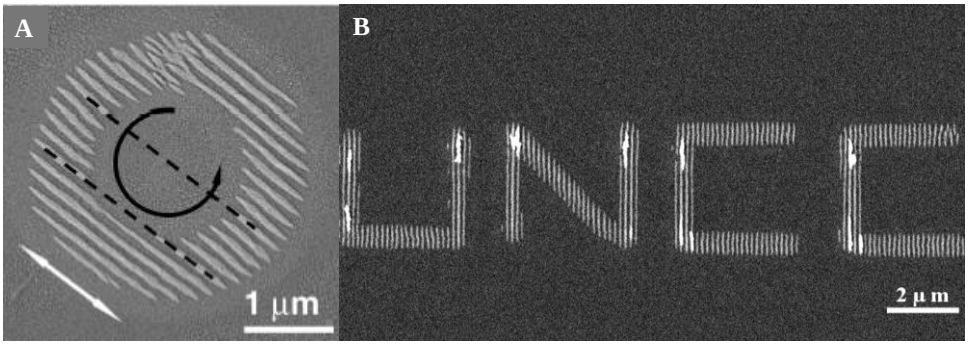

Figure 7.1 SEM images of (A) circular and (B) “UNCC” grating pattern written on sapphire substrate. The white and the black arrows indicate the laser polarization and the scanning direction, respectively.

The small deviation (<1.5%) in the grating period, obtained with a method like this without any external reference, suggests that the presence of the existing tooth determines the location of the next tooth in a precise manner. We exploit such excellent spatial registration among neighboring teeth to fabricate a larger-scale one-dimensional grating by performing multiple linear scans with proper offsets in the direction orthogonal to the substrate scanning. As demonstrated in Figure 7.2, with a vertical offset of 500 nm the

grating teeth between adjacent scans are connected to form nearly a straight line. The quality of such vertical registry is evident when comparing the connected grating tooth with the dashed line in Figure 7.2. Too large an offset, on the other hand, results in multiple lines of transverse gratings without any registry among the grating teeth. Figure 7.2 thus demonstrates the feasibility of fabricating large-area TNGs. To fabricate large-area TNG, an alternative method is to use the property of TNG that higher power yield more teeth inside the laser spot. A low numerical aperture objective lens can be adapted to enlarge the laser focus spot size. However, this method requires much higher laser power input to guarantee that a large area inside which laser power exceeds the power threshold value required for TNG growth.

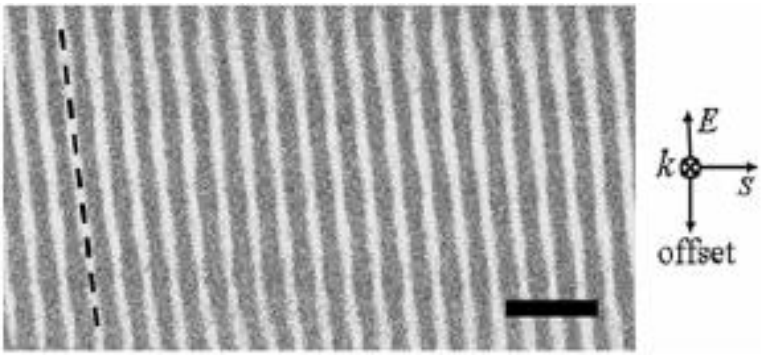

Figure 7.2 SEM image of multiple scanned TNGs with overlap obtained by raster scanning the substrate at 20 mW and 0.6μm/s with an offset of 500 nm. The scale bar represents 500 nm. The inset indicates the relative orientations among laser incidence *(k)*, substrate scanning *(S)*, laser polarization *(E)* and offset. The dashed line is only for the purpose of guiding the eyes.

Zinc Oxide micro wire was also tested as a potential device to write tungsten nanograting on. Figure 7.3(a) shows a transverse TNG scan cross a ZnO micro-wire and 7.3(b) is the close look on the wire. The grating quality is not well registered, which could be due to the surface morphology change from substrate to the wire, and the defects on the wire itself. Nevertheless, it demonstrates the potential of fabricating periodic

nanostructures onto other micro or nano material systems.

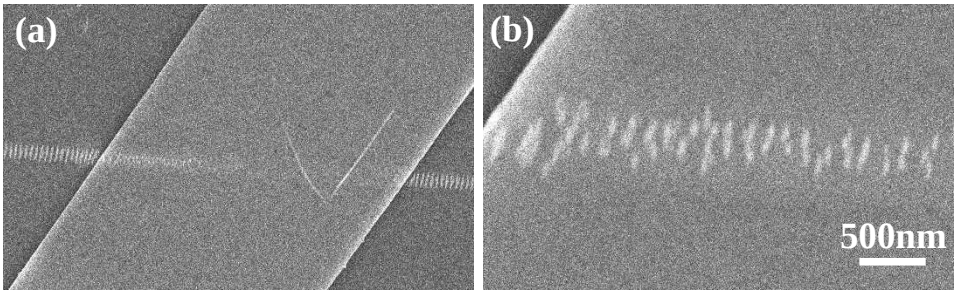

Figure 7.3 SEM images of Tungsten nanostructure on surface of ZnO Micro-wire.

Very attractively, this method can also be adapted to non-planar substrates easily, as demonstrated in Figure 7.4(a). A 30-μm long line of longitudinal TNGs was fabricated on the surface of optical fibers simply by scanning the laser beam across the fiber surface transversely. To demonstrate the feasibility of grating grown on even larger curvature surface, Hydrofluoric acid etched optical fiber was also tested in the experiment. It was found that TNG can grow on the etched fiber (Figure 7.4(b)) surface, which has a much larger curvature than the original fiber. However, due to the non-smoothly etching surface (which can be clearly seen from Figure 7.4(c)), the produced nanogratings are not very well registered, as shown in Figure 7.4(c). Neat and ordered TNG is expecting to grow on large curvature surface with a provided smooth surface condition.

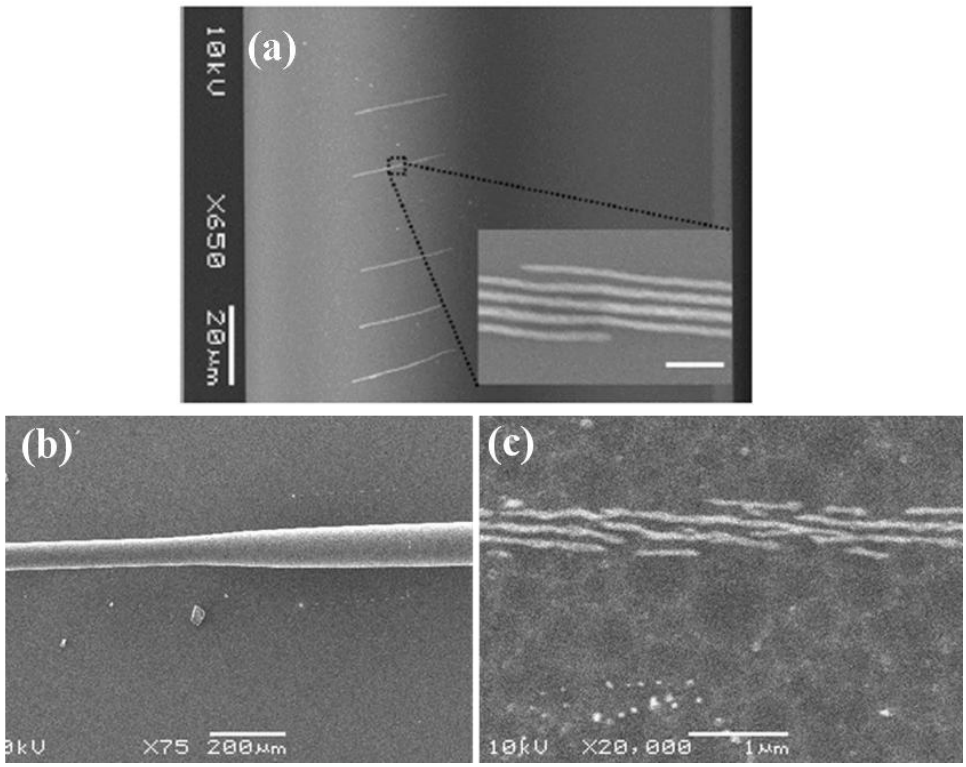

Figure 7.4 SEM image of (a) tungsten nanogratings grown on the surface of glass optical fiber. Inset: magnified view of the longitudinal nanogratings (scale bar: 500 nm), (b) profile of an etched glass optical fiber, and (c) tungsten nanogratings grown on the surface of etched optical fiber.

7.2 Comparison with other nano-patterning methods

Comparing to other nano-patterning techniques, our method has several advantages. The uniformity in the grating tooth length (< 4%) is a significant improvement in controlling the size distribution compared to other self-assembly processes such as Stranski-Krastanov growth of germanium islands on Si substrate whose size deviation is larger than 40%[53]. The uniformity of the grating period (< 1.5%), although not as good as that obtained with well-established interference lithography[54], is achieved without any external control or feedback. The throughput of our method at current stage is low and is limited by the output power of laser which restricts the focus spot to be very small (~ µm in diameter) and slow scanning speed (~ µm/s); higher laser power is expected to

scale up the throughput. Although the throughput is much slower than the e-beam lithography, our technique is a single-step add-on process that can avoid multiple steps and potential cross contamination associated with the e-beam lithography, which also requires a pre-made mask. Comparing with dip-pen nanolithography[55], which uses AFM tips to deposit target molecules onto substrate, our method has a significant advantage in that it fabricates multiple period lines spontaneously during a single scan; the number of parallel lines that are concurrent in such scan is simply proportional to the laser spot size without any external manipulation or beam shaping. Finally, our method can be adapted to non-planar substrates.

7.3 Potential applications of TNG

The ease of fabrication, the good uniformity, the flexibility on substrate choice, and the simplicity of controlling the grating period and tooth length precisely make this femtosecond laser initiated self-assembly during deposition attractive for practical applications. The potential applications of TNG include but not limit to:

- Photonic. Sub-wavelength metallic periodic nanostructures could be suitable for metallic-grid polarizer, optical diffraction grating, and grating couplers, et al.
- Optical sensor and antenna. It has been shown that elongated individual grating teeth have field enhancement along the direction of polarization direction of incoming light. This property can be utilized in optical sensor and antenna. It was demonstrated that sharp metallic tips could be used as optical antenna to concentrate light at nanometer scale[56]. And the selective wavelength could be conveniently tuned by controlling the length of the gating tooth[57].
- Reaction catalyst. It was demonstrated that TNG can be used as patterned catalyst

for the selective growth of tungsten oxide nanowire[58]. The nanowires were found only grown on top of the grating teeth. The flake structure written with slow scanning speed and/or high laser power has very large reaction surface which could be used to enhance catalytic reactions.

- The feasibility of fabricating TNGs on micro-structure and non-planar substrates could lead to many interesting applications in optical sensing and information processing.

However, for many practical applications it is desired to extend this technique to other metal materials such as Au, Ag, etc.

REFERENCES

1. E.Hargrove, L., R.L. Fork, and M.A. Pollack, *LOCKING OF HeNe LASER MODES INDUCED BY SYNCHRONOUS INTRACAVITY MODULATION.* Appl. Phys. Lett., 1964. **5**.

2. Fork, R.L., et al., *Compression of Optical Pulses to 6 Femtoseconds by Using Cubic Phase Compensation.* Optics Lett., 1987. **12**(7): p. 483-485.

3. Kamlage, G., et al., *Deep drilling of metals by femtosecond laser pulses.* Appl. Physics A: Materials Science & Processing, 2003. **77**(2): p. 307-310.

4. Haight, R., et al., *MARS: Femtosecond laser mask advanced repair system in manufacturing.* J. of Vac. Sci. & Techn. B, 1999. **17**(6): p. 3137-3143.

5. Juhasz, T., et al., *Corneal refractive surgery with femtosecond lasers.* Ieee Journal of Selected Topics in Quantum Electronics, 1999. **5**(4): p. 902-910.

6. Minoshima, K., et al., *Photonic device fabrication in glass by use of nonlinear materials processing with a femtosecond laser oscillator.* Opt. Lett., 2001. **26**(19): p. 1516-1518.

7. Serbin, J., et al., *Femtosecond laser-induced two-photon polymerization of inorganic organic hybrid materials for applications in photonics.* Opt. Lett., 2003. **28**(5): p. 301-303.

8. Cai, W.J., T.J. Reber, and R. Piestun, *Computer-generated volume holograms fabricated by femtosecond laser micromachining.* Optics Letters, 2006. **31**(12): p. 1836-1838.

9. Haight, R., P. Longo, and A. Wagner, *Metal deposition with femtosecond light pulses at atmospheric pressure.* J. of Vac. Sci. & Techn. A, 2003. **21**(3): p. 649-652.

10. Zhang, H.T., et al., *Deposition of tungsten nanogratings induced by a single femtosecond laser beam.* Optics Express, 2007. **15**(10): p. 5937-5947.

11. Tang, M.Z., H.T. Zhang, and T.H. Her, *Self-assembly of tunable and highly uniform tungsten nanogratings induced by a femtosecond laser with nanojoule energy.* Nanotechnology, 2007. **18**(48): p. 5.

12. Baüerle, D., *Laser Processing and Chemistry*. 3rd ed. 2000, Berlin; New York: Springer.

13. Bauerle, D., *Laser processing and chemistry*. 3rd rev. enlarged ed. 2000, Berlin ; New York Springer.

14. Enhrlich, D.J. and J.Y. Tsao, *Laser microfabrication : thin film processes and lithography*. 1989, BOSTON: Academic Press.

15. Venkataraman, B., et al., *A Molecular-Beam Study of the 1-Photon, 2-Photon, and 3-Photon Photodissociation Mechanism of the Group-Vib (Cr, Mo, W) Hexacarbonyls at 248nm.* Journal of Chemical Physics, 1990. **92**(9): p. 5338-5362.

16. Rytzfroidevaux, Y., et al., *Cadmium Deposition on Transparent Substrates by Laser-Induced Dissociation of Cd(Ch3)2 at Visible Wavelengths.* Applied Physics A-Materials Science & Processing, 1982. **27**(3): p. 133-138.

17. Birnbaum, M., *Semiconductor surface damage produced by ruby laser.* J. Appl. Phys., 1965. **36**: p. 3688.

18. van Driel, H.M., J.E. Sipe, and J.F. Young, Physical Review Letters, 1982. **49**: p. 1955.

19. Wagner, R., et al., *Subwavelength ripple formation induced by tightly focused femtosecond laser radiation.* Applied Surface Science, 2006. **252**(24): p. 8576-8579.

20. Wu, Q.H., et al., *Femtosecond laser-induced periodic surface structure on diamond film.* Applied Physics Letters, 2003. **82**(11): p. 1703-1705.

21. Vorobyev, A.Y. and C. Guo, *Femtosecond laser-induced periodic surface structure formation on tungsten.* Journal of Applied Physics, 2008. **104**(6): p. 063523-3.

22. Varlamova, O., et al. *Control parameters in pattern formation upon femtosecond laser ablation*. 2007.

23. Reif, J., F. Costache, and M. Bestehorn, *Self-Organized Surface Nanostructuring by Femtosecond Laser Processing*, in *Recent Advances in Laser Processing Of Materials*, J. PERRIÈRE, E. MILLON, and E. FOGARASSY, Editors. 2006, Elsevier Science. p. 472.

24. Zhao, Q.Z., S. Malzer, and L.J. Wang, *Formation of subwavelength periodic structures on tungsten induced by ultrashort laser pulses.* Optics Letters, 2007. **32**(13): p. 1932-1934.

25. Bonse, J., et al., *Femtosecond laser ablation of silicon-modification thresholds and morphology.* Applied Physics A-Materials Science & Processing, 2002. **74**(1): p. 19-25.

26. Miyaji, G. and K. Miyazaki, *Origin of periodicity in nanostructuring on thin film surfaces ablated with femtosecond laser pulses.* Optics Express, 2008. **16**(20): p. 16265-16271.

27. Huang, M., et al., *Mechanisms of ultrafast laser-induced deep-subwavelength*

gratings on graphite and diamond. Physical Review B, 2009. **79**(12).

28. Vorobyev, A.Y., V.S. Makin, and C.L. Guo, *Periodic ordering of random surface nanostructures induced by femtosecond laser pulses on metals.* Journal of Applied Physics, 2007. **101**(3).

29. Huang, M., et al., *Large area uniform nanostructures fabricated by direct femtosecond laser ablation.* Optics Express, 2008. **16**(23): p. 19354-19365.

30. Yasumaru, N., K. Miyazaki, and J. Kiuchi, *Fluence dependence of femtosecond-laser-induced nanostructure formed on TiN and CrN.* Applied Physics a-Materials Science & Processing, 2005. **81**(5): p. 933-937.

31. Costache, F., M. Henyk, and J.g. Reif, *Modification of dielectric surfaces with ultra-short laser pulses.* Applied Surface Science, 2002. **186**(1-4): p. 352-357.

32. Wang, X.C., et al., *Femtosecond pulsed laser-induced periodic surface structures on GaN/sapphire.* Applied Surface Science, 2005. **252**(5): p. 1492-1497.

33. Costache, F., M. Henyk, and J. Reif, *Modification of dielectric surfaces with ultra-short laser pulses.* Applied Surface Science, 2002. **186**(1-4): p. 352-357.

34. Reif, J., O. Varlamova, and F. Costache, *Femtosecond laser induced nanostructure formation: self-organization control parameters.* Applied Physics a-Materials Science & Processing, 2008. **92**(4): p. 1019-1024.

35. Tan, B. and K. Venkatakrishnan, *A femtosecond laser-induced periodical surface structure on crystalline silicon.* Journal Of Micromechanics and Microengineering, 2006. **16**: p. 1080-1085.

36. Bradley, R.M. and J.M.E. Harper, *Theory of ripple topography induced by ion bombardment.* Journal of Vacuum Science & Technology A: Vacuum, Surfaces, and Films, 1988. **6**(4): p. 2390-2395.

37. Chason, E., et al., *Roughening instability and evolution of the Ge(001) surface during ion sputtering.* Physical Review Letters, 1994. **72**(19): p. 3040.

38. Erlebacher, J., et al., *Spontaneous Pattern Formation on Ion Bombarded Si(001).* Physical Review Letters, 1999. **82**(11): p. 2330.

39. Habenicht, S., et al., *Ripple propagation and velocity dispersion on ion-beam-eroded silicon surfaces.* Physical Review B, 2002. **65**(11): p. 115327.

40. Costache, F., M. Henyk, and J. Reif, *Surface patterning on insulators upon femtosecond laser ablation.* Applied Surface Science, 2003. **208-209**: p. 486-491.

41. Shimotsuma, Y., et al., *Self-organized nanogratings in glass irradiated by ultrashort*

light pulses. Physical Review Letters, 2003. **91**(24).

42. Hnatovsky, C., et al., *Pulse duration dependence of femtosecond-laser-fabricated nanogratings in fused silica.* Applied Physics Letters, 2005. **87**(1).

43. Bhardwaj, V.R., et al., *Optically produced arrays of planar nanostructures inside fused silica.* Physical Review Letters, 2006. **96**(5): p. 057404-4.

44. Simova, E., et al. *Femtosecond laser-induced long-range self-organized periodic planar nanocracks for applications in biophotonics*. in *SPIE Photonic West*. 2007.

45. Yang, W.J., et al., *Self-assembled periodic sub-wavelength structures by femtosecond laser direct writing.* Optics Express, 2006. **14**(21): p. 10117-10124.

46. Hnatovsky, C., et al., *Fabrication of microchannels in glass using focused femtosecond laser radiation and selective chemical etching.* Applied Physics A: Materials Science & Processing, 2006. **84**(1): p. 47-61.

47. Taylor, R., C. Hnatovsky, and E. Simova, *Applications of femtosecond laser induced self-organized planar nanocracks inside fused silica glass.* Laser & Photonics Reviews, 2008. **2**(1-2): p. 26-46.

48. Wilson, R.J. and F.A. Houle, *COMPOSITION, STRUCTURE, AND ELECTRIC-FIELD VARIATIONS IN PHOTODEPOSITION.* Physical Review Letters, 1985. **55**(20): p. 2184-2187.

49. Osgood, J.R.M. and D.J. Ehrlich, *Optically induced microstructures in laser-photodeposited metal films.* Opt. Lett., 1982. **7**(8): p. 385-387.

50. Brueck, S.R.J. and D.J. Ehrlich, *Stimulated Surface-Plasma-Wave Scattering And Growth Of A Periodic Structure In Laser-Photodeposited Metal-Films.* Physical Review Letters, 1982. **48**(24): p. 1678-1681.

51. Chen, C.J. and R.M. Osgood, *Direct Observation of the Local-Field -enhanced Surface Photochemical Reactions.* Physical Review Letters, 1983. **50**(21): p. 1705-1709.

52. Peng, Y., et al., *CO_2-Laser-Induced Regular Periodic Structures on Glass Substrates.* Jpn. J. appl. Phys., 2003. **42**: p. 6920.

53. Liu, B., et al., *Atomic force microscopy study of the growth and annealing of Ge islands on Si(100).* Journal of Vacuum Science & Technology B, 2002. **20**(2): p. 678-684.

54. Heilmann, R.K., et al., *Dimensional metrology for nanometre-scale science and engineering: towards sub-nanometre accurate encoders.* Nanotechnology, 2004. **15**(10): p. S504-S511.

55. Hong, S.H. and C.A. Mirkin, *A nanoplotter with both parallel and serial writing capabilities.* Science, 2000. **288**(5472): p. 1808-1811.

56. Kottmann, J.P., et al., *Spectral response of plasmon resonant nanoparticles with a non-regular shape.* Optics Express, 2000. **6**(11): p. 213-219.

57. Crozier, K.B., et al., *Optical antennas: Resonators for local field enhancement.* Journal of Applied Physics, 2003. **94**(7): p. 4632-4642.

58. Zhang, H., et al., *Selective growth of tungsten oxide nanowires via a vapor-solid process.* Submitted to Nanotechnology, 2009.

APPENDIX A: DETAILED RESULTS ON SUBSTRATE STUDY

In this Appendix, the detailed results on substrate study are presented. For each substrate, transverse TNG array with different laser power and scanning speed were written to study in detail the effects of laser power and scanning speed on the periodicity of TNG. The scanning speeds range was extended from 0.2-μm/s to 5-μm/s. Plots of the grating period versus scanning speed for different laser power on each substrate are presented after the SEM images. Detailed discussion on these data is presented in Chapter 5.

1. Sapphire

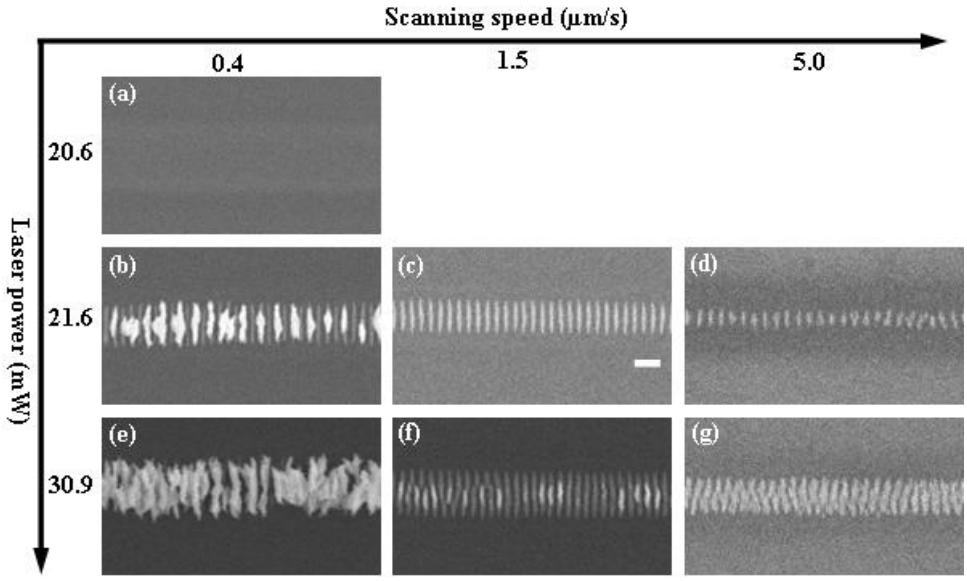

Figure Appx. 1 SEM images of transverse tungsten nanograting written on sapphire with different laser power and scanning speed. The scale bar represents 500-nm and applies to all images.

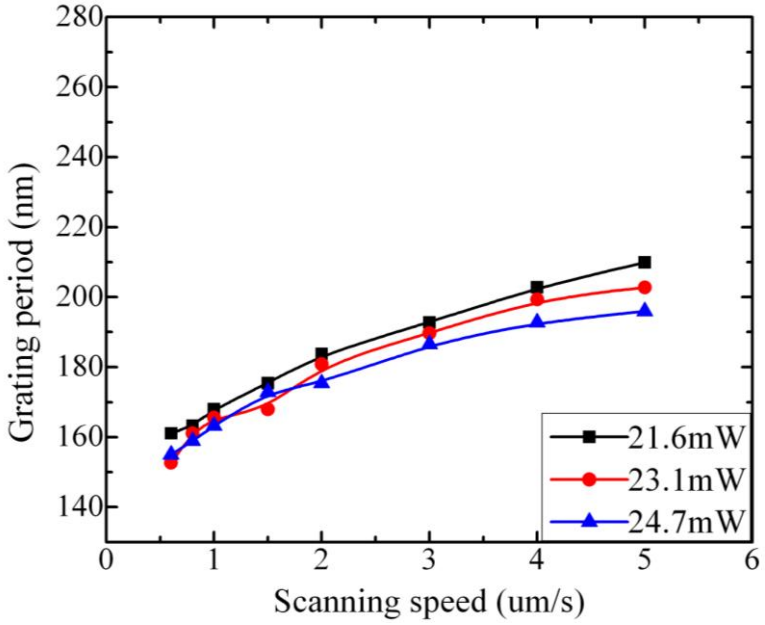

Figure Appx. 2 Plot of TNG period as a function of scanning speed for different laser power on sapphire substrate.

2. Soda-lime glass

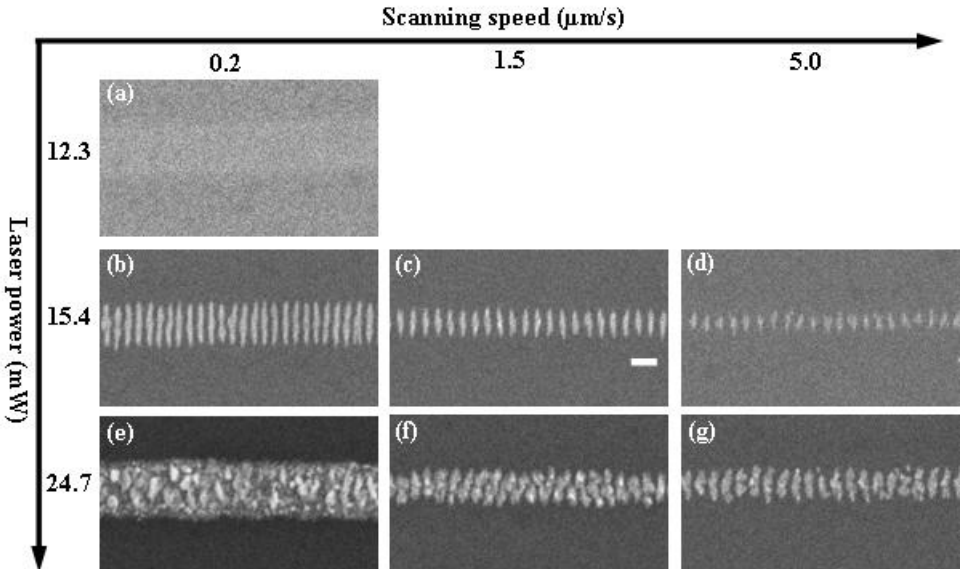

Figure Appx. 3 SEM images of transverse tungsten nanograting written on soda-lime glass with different laser power and scanning speed. The scale bar represents 500-nm and applies to all images.

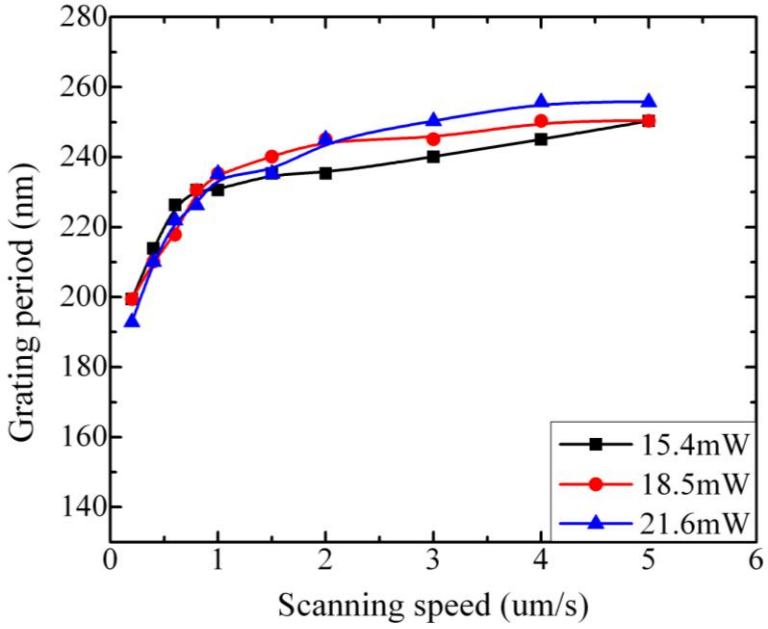

Figure Appx. 4 Plot of TNG period as a function of scanning speed for different laser power on soda-lime glass substrate.

3. Fused silica

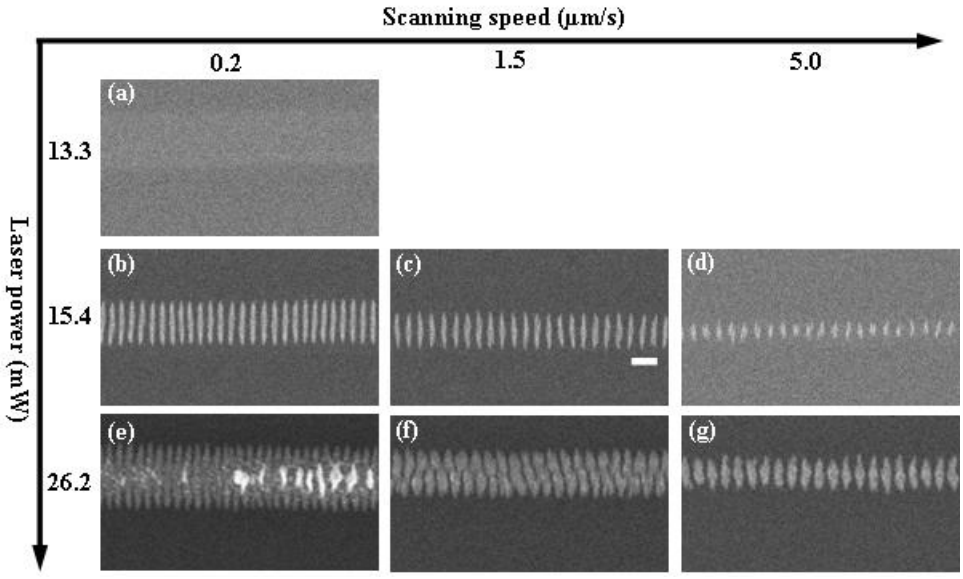

Figure Appx. 5 SEM images of transverse tungsten nanograting written on fused silica with different laser power and scanning speed. The scale bar represents 500-nm and applies to all images.

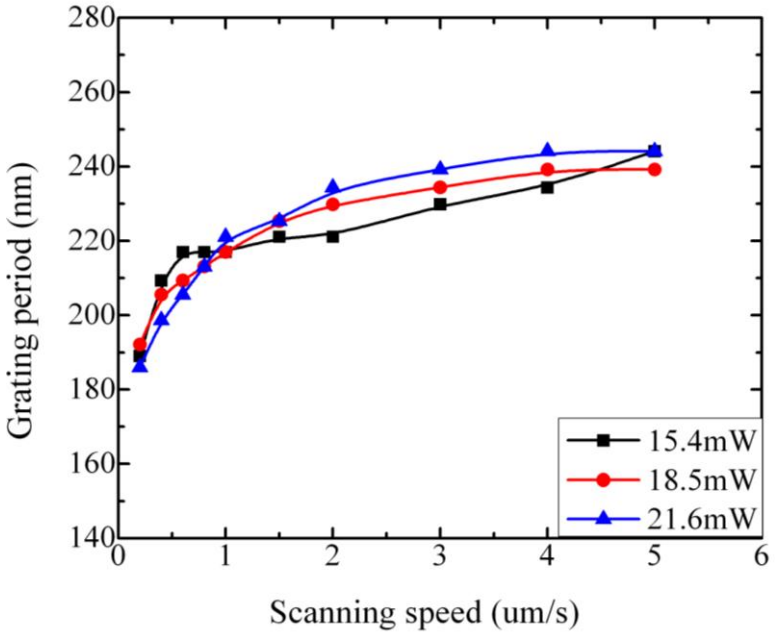

Figure Appx. 6 Plot of TNG period as a function of scanning speed for different powers on fused silica substrate.

4. Quartz

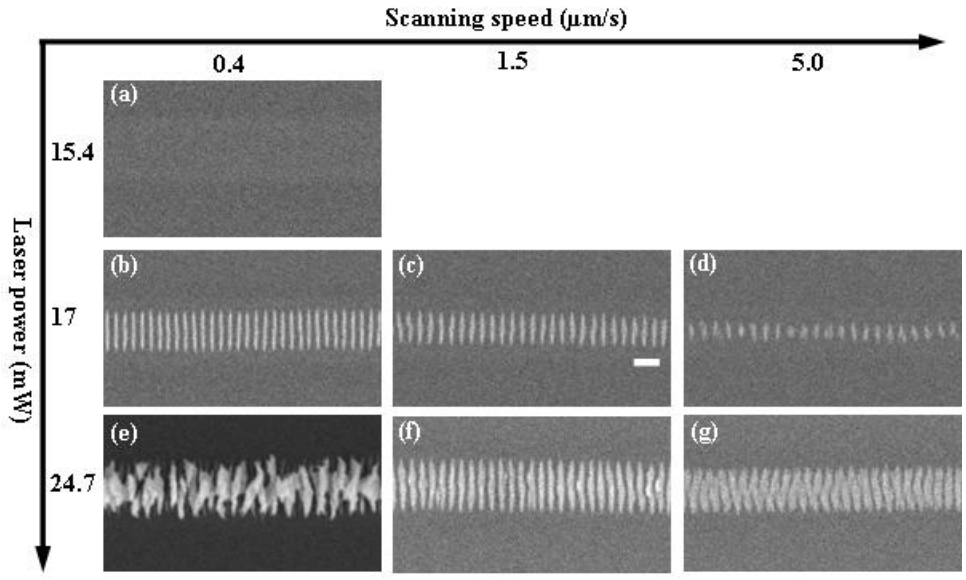

Figure Appx. 7 SEM images of transverse tungsten nanograting written on quartz with different laser power and scanning speed. The scale bar represents 500-nm and applies to all images.

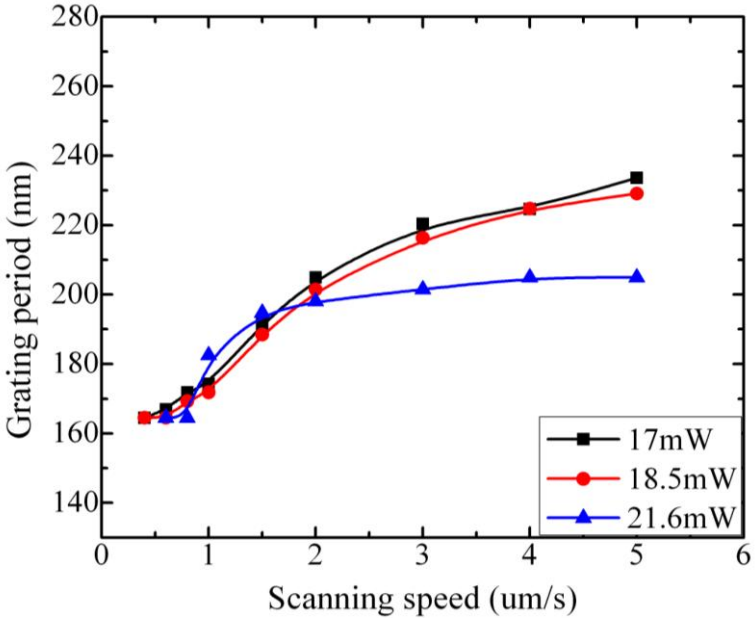

Figure Appx. 8 Plot of TNG period as a function of scanning speed for different laser powers on quartz substrate.

5. Calcium fluoride

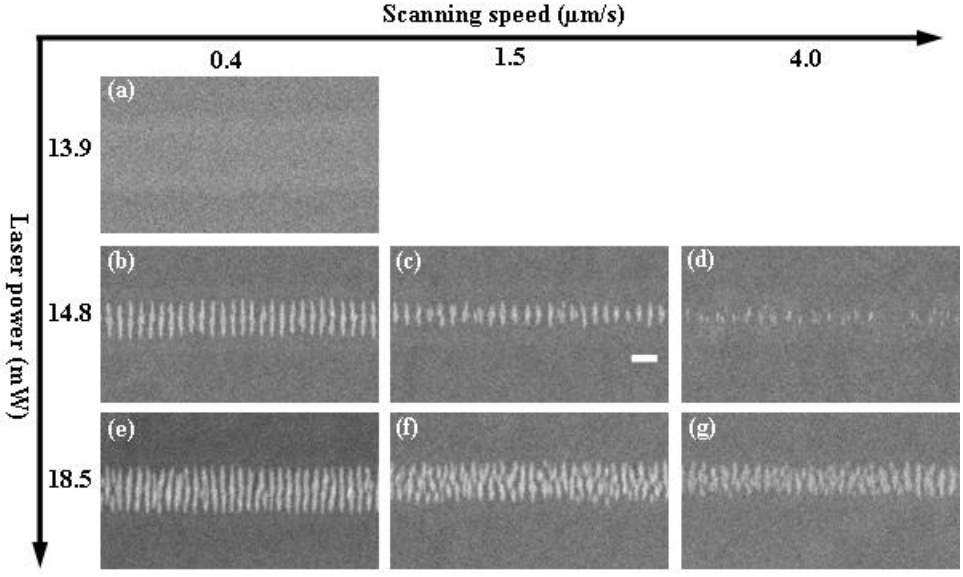

Figure Appx. 9 SEM images of transverse tungsten nanograting written on calcium fluoride with different laser power and scanning speed. The scale bar represents 500-nm and applies to all images.

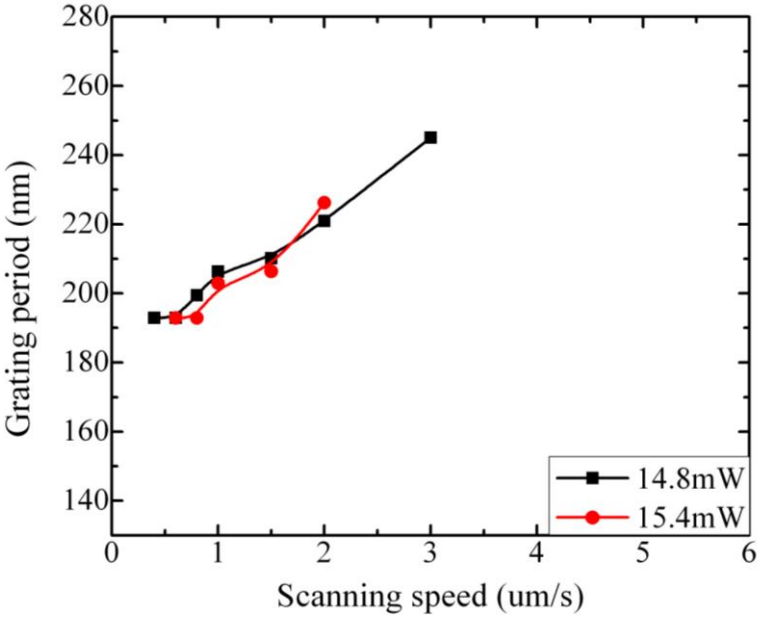

Figure Appx. 10 Plot of TNG period as a function of scanning speed for different powers on calcium fluoride substrate.

6. Magnesium fluoride

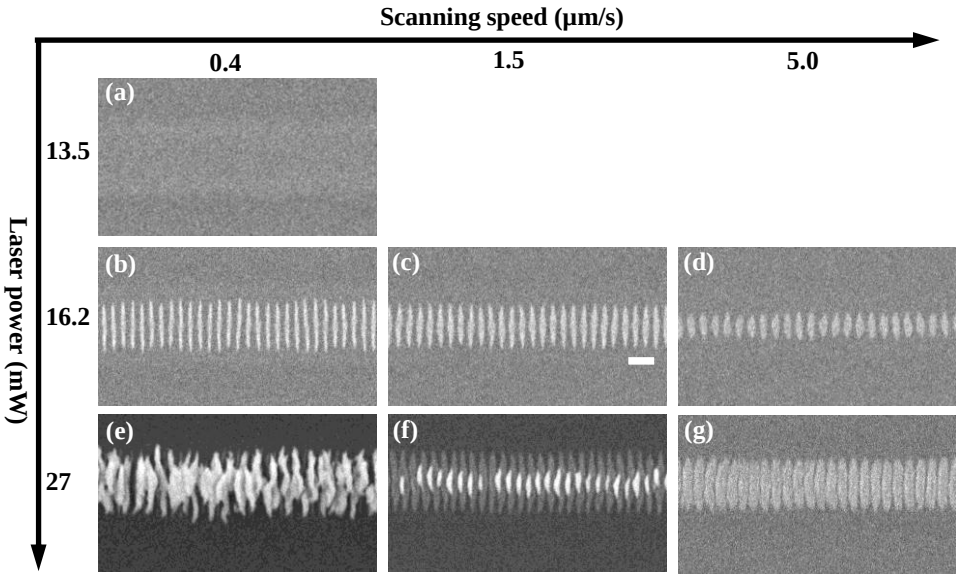

Figure Appx. 11 SEM images of transverse tungsten nanograting written on Magnesium fluoride with different laser power and scanning speed. The scale bar represents 500-nm and applies to all images.

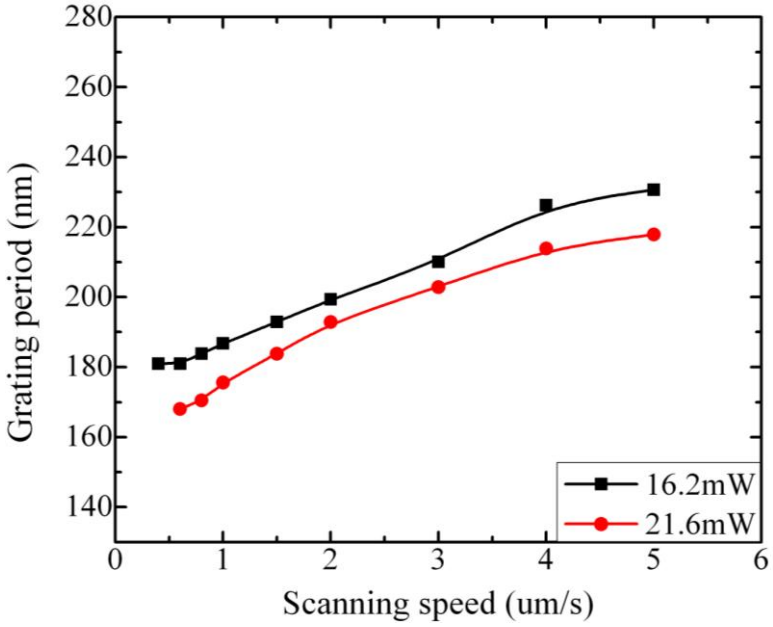

Figure Appx. 12 Plot of TNG period as a function of scanning speed for different laser powers on magnesium fluoride substrate.

7. Magnesium oxide <100>

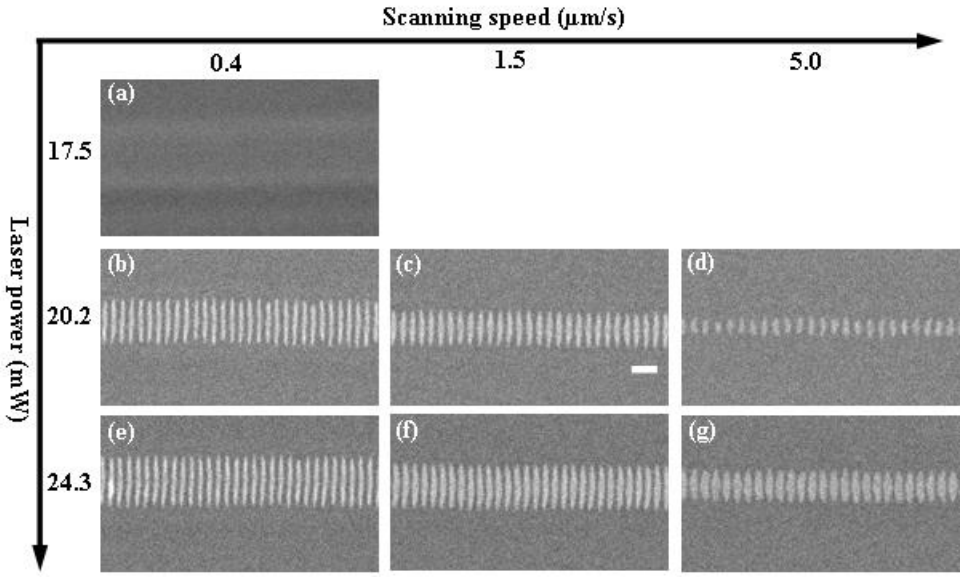

Figure Appx. 13 SEM images of transverse tungsten nanograting written on Magnesium oxide <100> with different laser power and scanning speed. The scale bar represents 500-nm and applies to all images.

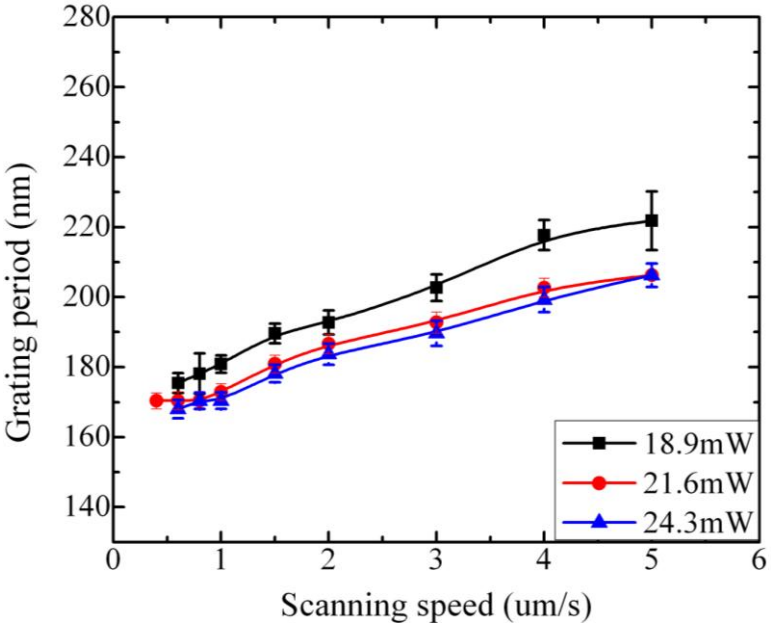

Figure Appx. 14 Plot of TNG period as a function of scanning speed for different laser powers on magnesium oxide substrate <100>.

9. Magnesium oxide <110>

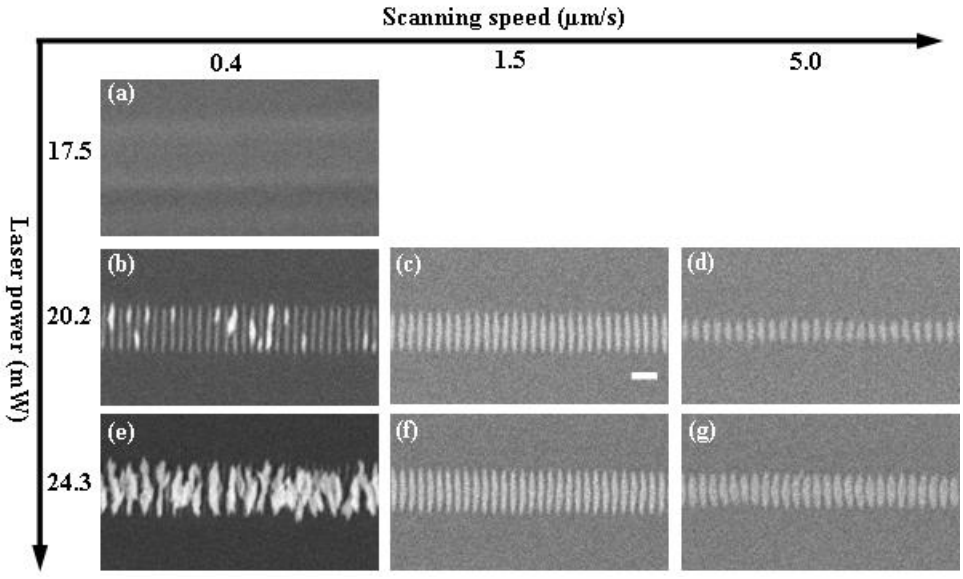

Figure Appx. 15 SEM images of transverse tungsten nanograting written on Magnesium oxide <110> with different laser power and scanning speed. The scale bar represents 500-nm and applies to all images.

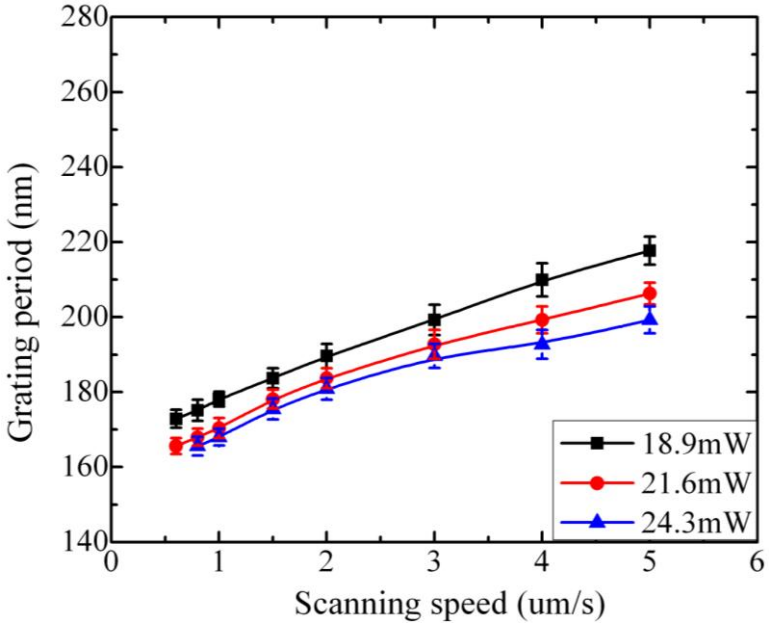

Figure Appx. 16 Plot of TNG period as a function of scanning speed for different laser powers on magnesium oxide substrate <110>.

9. Aluminum nitride

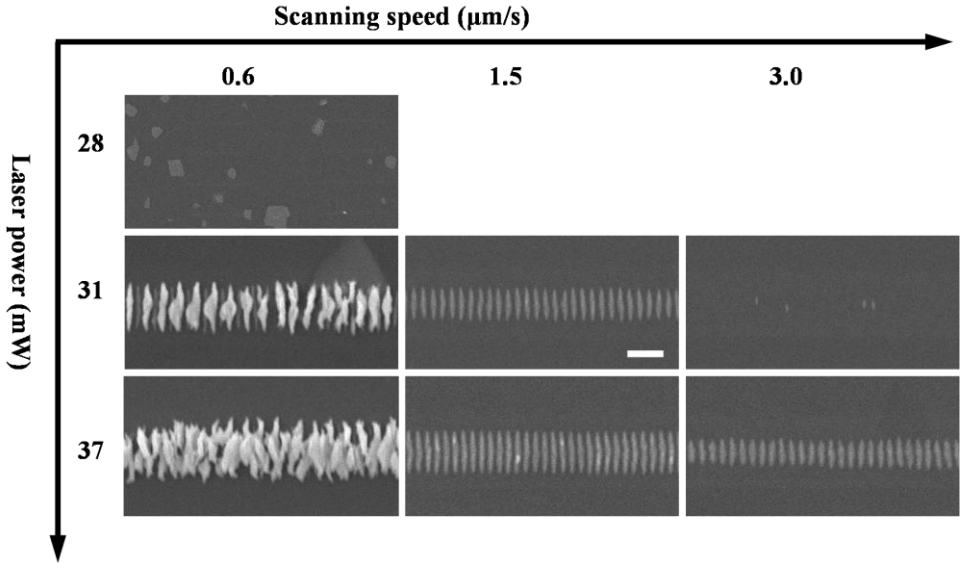

Figure Appx. 17 SEM images of transverse tungsten nanograting written on aluminum nitride with different laser power and scanning speed. The scale bar represents 500-nm and applies to all images.

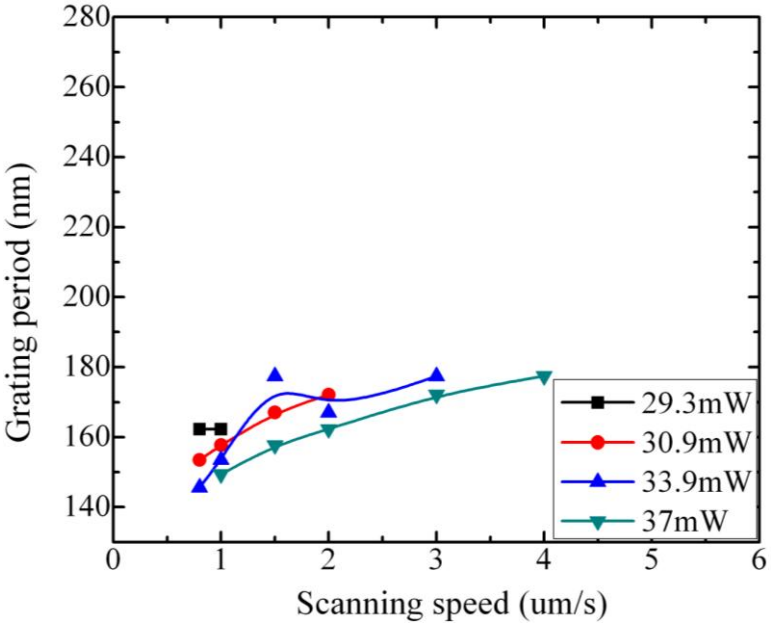

Figure Appx. 18 Plot of TNG period as a function of scanning speed for different powers on aluminum nitride substrate.

10. Zinc oxide

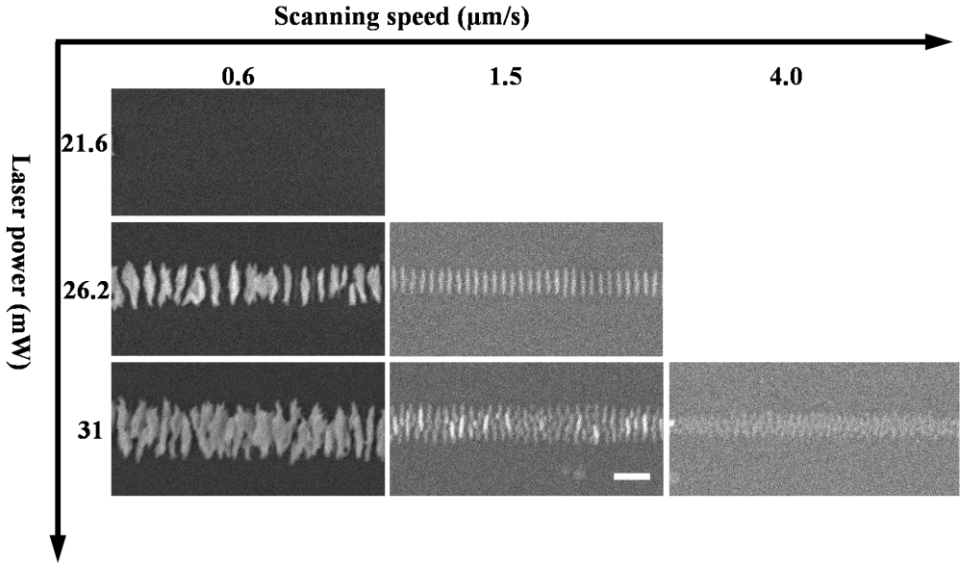

Figure Appx. 19 SEM images of transverse tungsten nanograting written on Zinc Oxide with different laser power and scanning speed. The scale bar represents 500-nm and applies to all images.

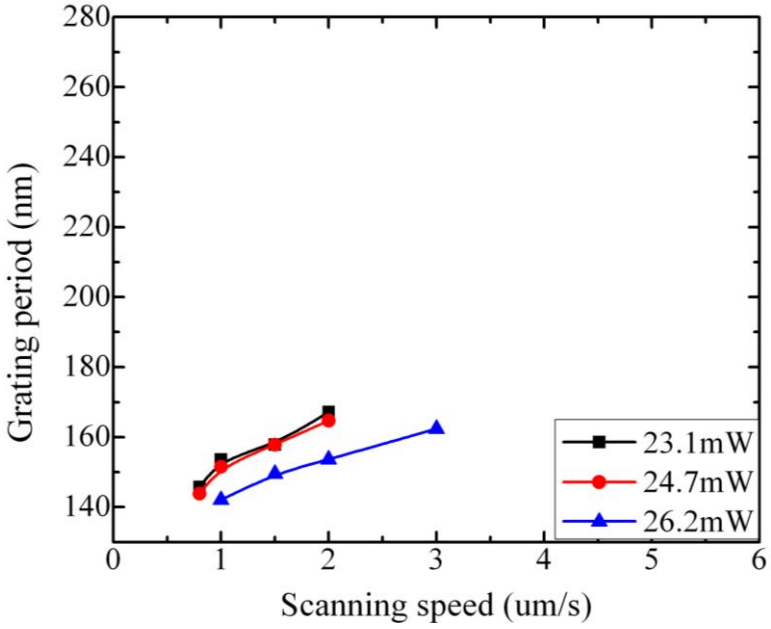

Figure Appx. 20 Plot of TNG period as a function of scanning speed for different powers on zinc oxide substrate.

10. Gallium nitride

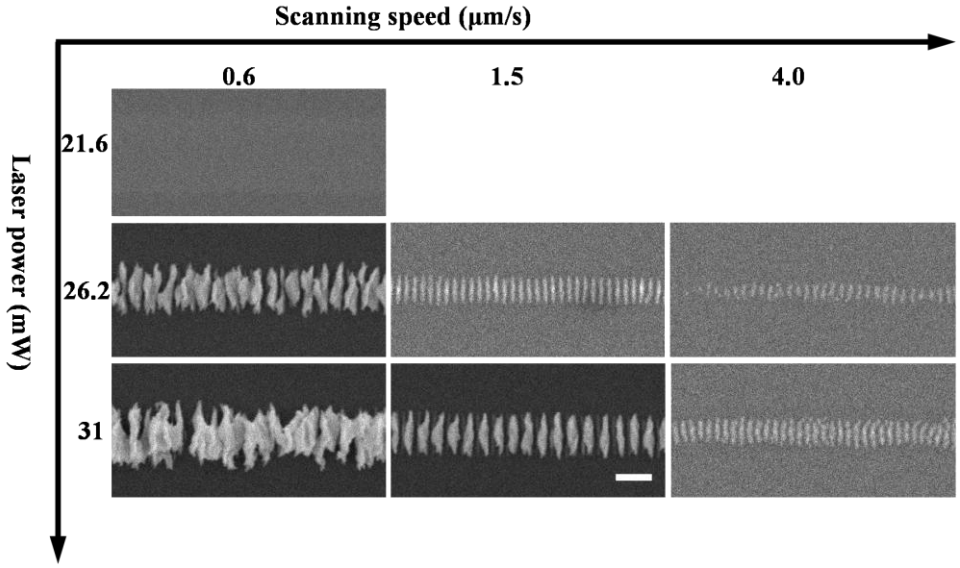

Figure Appx. 21 SEM images of transverse tungsten nanograting written on Gallium nitride with different laser power and scanning speed. The scale bar represents 500-nm and applies to all images.

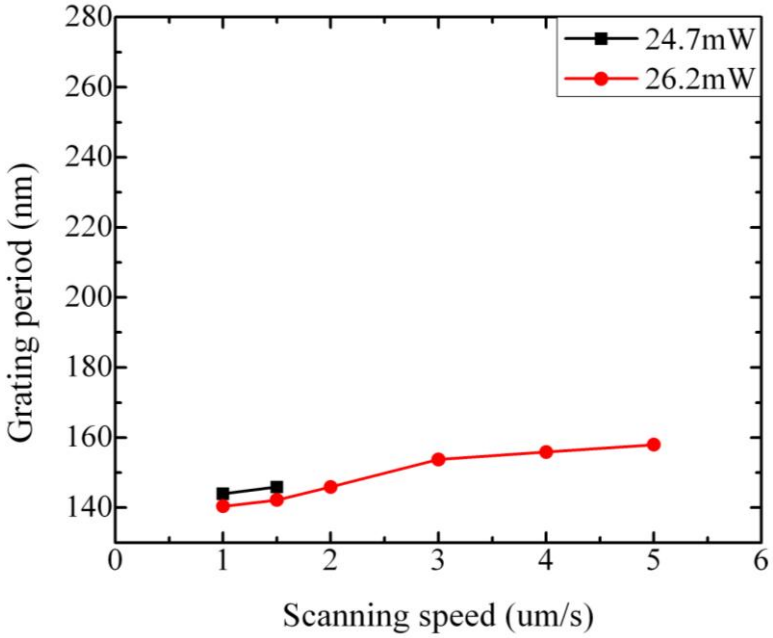

Figure Appx. 22 Plot of TNG period as a function of scanning speed for different powers on gallium nitride substrate.

12. Silicon Nitride

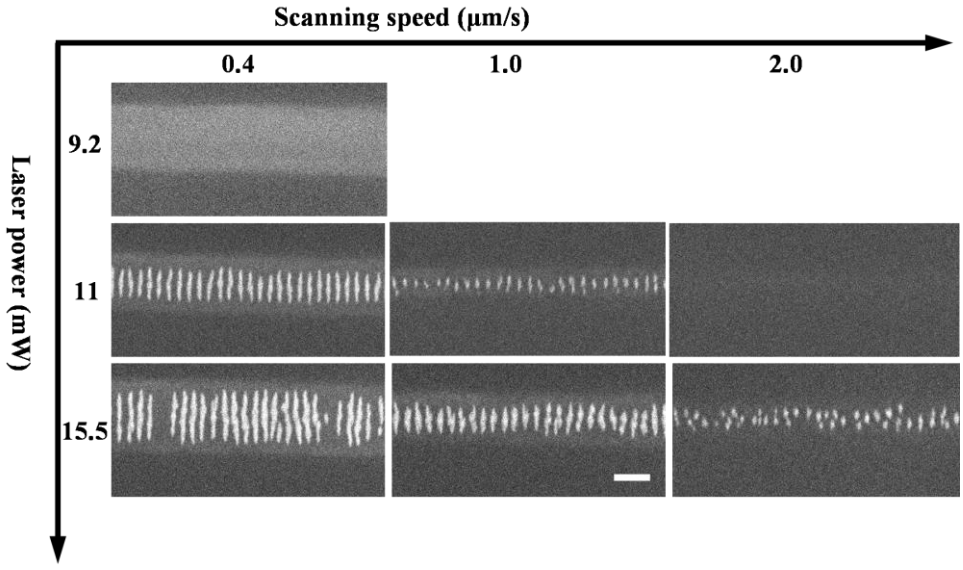

Figure Appx. 23 SEM images of transverse tungsten nanograting written on Silicon nitride with different laser power and scanning speed. The scale bar represents 500-nm and applies to all images.

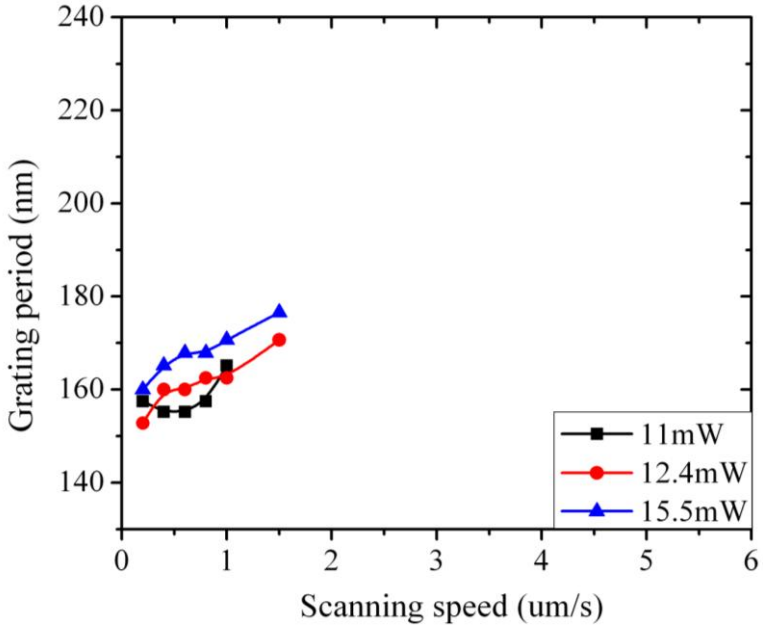

Figure Appx. 24 Plot of TNG period as a function of scanning speed for different powers on silicon nitride substrate.

APPENDIX B: DERIVATION ON THE ABSORPTANCE OF TUNGSTEN FILM

To calculate that threshold temperature, we solve the heat diffusion equation

$$\frac{\partial T(z,t)}{\partial t} = \alpha \frac{\partial^2 T(z,t)}{\partial z^2}, \tag{1}$$

where $\alpha = \frac{\kappa}{\rho c_p}$ is the thermal diffusivity of the substrate and ρ, κ, c_p are the mass density, thermal conductivity, and heat capacity of the material, respectively. It is assumed that the tungsten film has identical temperature due to the thin thickness (10-nm), and the upper surface of the substrate T(z=0) has the same temperature as tungsten film. We have the following boundary and initial conditions:

$$\frac{\partial T}{\partial z}(0,t) = -\frac{I_a(t)}{\kappa}, \tag{2}$$

$$T(z,0) = 0, \tag{3}$$

where $I_a(t)$ is the absorbed intensity $I_a(t)=AI_{in}(t)$.

By taking the Laplace transform of equation (1) with respect to time t, eq.(1) can be written as

$$s\vartheta(z,s) = \alpha \frac{d^2\vartheta(z,s)}{dz^2}, \tag{4}$$

where $\vartheta = \int_0^\infty Te^{-st}dt$ is the Laplace transform of T. note that

$$\int_0^\infty \frac{\partial T}{\partial t} e^{-st}dt = s\int_0^\infty Te^{-st}dt - T(z,0) = s\int_0^\infty Te^{-st}dt.$$

Taking the Laplace transform of eq. (2) we obtain

$$\frac{\partial \vartheta(z=0)}{\partial z} = -\frac{f(s)}{\kappa}, \quad f(s) = \int_0^\infty I_a(t)e^{-st}dt \tag{5}$$

The solution of Eq.(6.4) combine with the boundary condition of Eq.(5) is

$$\vartheta(z,s) = \frac{1}{\kappa\sqrt{s/\alpha}} f(s) e^{-z\sqrt{s/\alpha}}, \tag{6}$$

with the identity $L^{-1}[\frac{1}{\sqrt{s}} e^{-\kappa\sqrt{s}}] = \frac{1}{\sqrt{\pi t}} e^{-\kappa^2/4t}$, and $L^{-1}[F(s/a)] = af(at)$, the inverse Laplace transform of Eq. (6) gives the solution of eq.(1) in real space,

$$\begin{aligned} T(z,t) &= \frac{1}{\kappa} I_a(t) * [\frac{\alpha}{\sqrt{\pi t \alpha}} e^{-z^2/4t\alpha}] \\ &= \frac{\sqrt{\alpha}}{\kappa\sqrt{\pi}} I_a(t) * [\frac{e^{-z^2/4t\alpha}}{\sqrt{t}}] = \frac{\sqrt{\alpha}}{\kappa\sqrt{\pi}} \int_0^t \frac{I_a(\tau)}{\sqrt{t-\tau}} e^{-z^2/4\alpha(t-\tau)} d\tau \end{aligned} \tag{7}$$

at z=0, which represents the surface of the substrate, the temperature which is also the temperature of the tungsten film is

$$T(0,t) = \frac{\sqrt{\alpha}}{\kappa\sqrt{\pi}} \int_0^t \frac{I_a(\tau)}{\sqrt{t-\tau}} d\tau. \tag{8}$$

For simplicity, assume the profile of the laser pulse is a step-like shape, then $I_a(t)$ is a constant, eq. (8) can be written as

$$T(0,t) = \frac{\sqrt{\alpha}}{\kappa\sqrt{\pi}} \int_0^t \frac{I_a(\tau)}{\sqrt{t-\tau}} d\tau = \frac{2I_a}{\kappa\sqrt{\pi}} \sqrt{\alpha t} \tag{9}$$

The maximum surface temperature occurs at the end of the pulse, i.e.

$$T_m = T(0,t_p) = \frac{2I_a}{\kappa\sqrt{\pi}} \sqrt{\alpha t_p}, \tag{10}$$

where t_p is the pulse duration.

Plug $\alpha = \frac{\kappa}{\rho c_p}$ into Eq. (10), the maximum temperature of the tungsten film thus is

$$T_m = 2(\frac{1}{\sqrt{\kappa\rho c_p}})\sqrt{t_p} I_a \tag{11}$$

thus the relationship between the surface temperature and input laser power is

$$T_m = 2(\frac{1}{\sqrt{\kappa\rho c_p}})\frac{\sqrt{t_p}}{D} P_a = 2(\frac{A}{\sqrt{\kappa\rho c_p}})\frac{\sqrt{t_p}}{D} P_{in} \tag{12}$$

where D is the area of laser focus, and A is the absorptance of the system.

Therefore, to obtain the same threshold temperature T_{th} for TNG growth, the threshold laser power required is:

$$P_{th} = \frac{D}{2\sqrt{t_p}} S \cdot T_{th} \tag{13}$$

where S here is a variable of substrate and $S = \frac{\sqrt{\kappa\rho c_p}}{A}$, for all the substrate, $\frac{D}{2\sqrt{t_p}}$ is the same.

To calculate the absorptance in tungsten film, since the penetration depth defined as

$$l = \frac{1}{\alpha} = (\frac{4\pi\kappa}{\lambda})^{-1}$$

of tungsten (n=3.39-i2.41) at 400-nm is 13.2-nm. And the tungsten film is about 10-nm on average. Thus there is certain amount of light can transmit through this film and reach the substrate. It is more accurate to consider a two-layer system (as drawing in figure appx. 25) when calculating the absorptivity. The substrate is considered to be infinite in thickness.

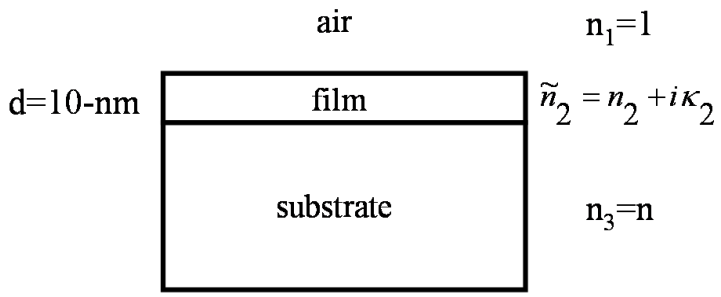

Figure Appx. 25 Schematic of two layer system when calculating the absorptance in tungsten film.

Thus for interface of air/film and film/substrate, Fresnel equations can be written as

$$r_{12} = \frac{n_1 - \tilde{n}_2}{n_1 + \tilde{n}_2}, \tag{14}$$

$$t_{12} = \frac{2}{n_1 + \tilde{n}_2}, \tag{15}$$

$$r_{23} = \frac{\tilde{n}_2 - n_3}{\tilde{n}_2 + n_3}, \tag{16}$$

$$t_{23} = \frac{2}{\tilde{n}_2 + n_3}. \tag{17}$$

The total reflection coefficient is

$$r = \frac{r_{12} + r_{23}e^{-2i\Phi}}{1 + r_{12}r_{23}e^{-2i\Phi}}, \tag{18}$$

where $\Phi = \frac{2\pi d}{\lambda}\tilde{n}_2.$ (19)

And the total transmission coefficient is

$$t = \frac{t_{12}t_{23}e^{-i\Phi}}{1 + r_{12}r_{23}e^{-2i\Phi}}. \tag{20}$$

The reflectance R and transmittance T then equal to

$$R = |r|^2 = r \cdot r^* = \left(\frac{r_{12} + r_{23}e^{-2i\Phi}}{1 + r_{12}r_{23}e^{-2i\Phi}}\right) \cdot \left(\frac{r_{12} + r_{23}e^{-2i\Phi}}{1 + r_{12}r_{23}e^{-2i\Phi}}\right)^*, \tag{21}$$

$$T = \frac{n_3}{n_1}|t|^2 = n_3 \cdot \left(\frac{t_{12}t_{23}e^{-i\Phi}}{1 + r_{12}r_{23}e^{-2i\Phi}}\right) \cdot \left(\frac{t_{12}t_{23}e^{-i\Phi}}{1 + r_{12}r_{23}e^{-2i\Phi}}\right)^*. \tag{22}$$

And the absorptance of the system equals to

$$A = 1 - R - T \tag{23}$$

So the absorptance of the air/film/substrate system is a function of the refractive index of the substrate. Their relationship is plotted in Fig. Appx. 26. The absorptance is decreasing with the refractive index of substrate.

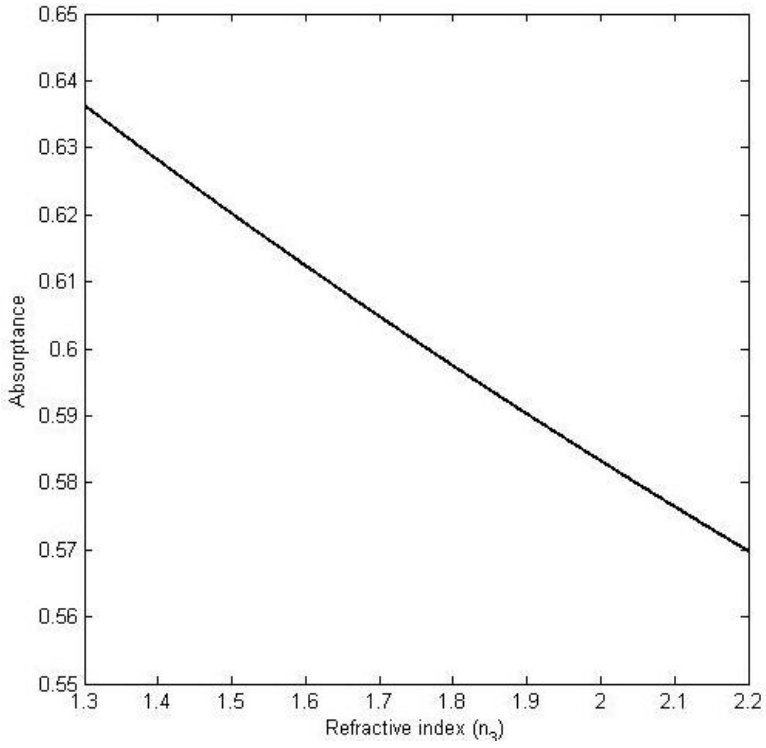

Figure Appx. 26 Absorptance in tungsten film as a function of refractive index of the substrate.